Rejuvenating aged osteoprogenitors for bone repair

Joshua Reeves[1,2], Pierre Tournier[1*], Pierre Becquart[1*], Robert Carton[2], Yin Tang[3,4], Alessandra Vigilante[2], Dong Fang[3,4] and Shukry J Habib[1]

[1]Department of Biomedical Sciences, University of Lausanne, Lausanne, Switzerland.
[2]Centre for Gene Therapy and Regenerative Medicine King's College London, London, UK.
[3]Zhejiang Provincial Key Laboratory for Cancer Molecular Cell Biology, Life Sciences Institute Zhejiang University, Hangzhou, Zhejiang 310058, China.
[4]Department of Ministry of Education, The Second Affiliated Hospital, Zhejiang University School of Medicine, Hangzhou, Zhejiang, China

* Contributed equally to this work.
Corresponding author: shukryjames.habib@unil.ch

Abstract

Aging is marked by a decline in tissue regeneration, posing significant challenges to an increasingly older population. Here, we investigate age-related impairments in calvarial bone healing and introduce a novel two-part rejuvenation strategy to restore youthful repair. We demonstrate that aging negatively impacts the calvarial bone structure and its osteogenic tissues, diminishing osteoprogenitor number and function and severely impairing bone formation. Notably, increasing osteogenic cell numbers locally fails to rescue repair in aged mice, identifying the presence of intrinsic cellular deficits. Our strategy combines Wnt-mediated osteoprogenitor expansion with intermittent fasting, which leads to a striking restoration of youthful levels of bone healing. We find that intermittent fasting improves osteoprogenitor function, benefits that can be recapitulated by modulating NAD^+ dependent pathways or the gut microbiota, underscoring the multifaceted nature of this intervention. Mechanistically, we identify mitochondrial dysfunction as a key component in age-related decline in osteoprogenitor function and show that both cyclical nutrient deprivation and Nicotinamide mononucleotide rejuvenate mitochondrial health, enhancing osteogenesis. These findings offer a promising therapeutic avenue for restoring youthful bone repair in aged individuals, with potential implications for rejuvenating other tissues.

Introduction

Flat bones like the sternum, scapula, pelvic bones, and skull bones play crucial roles in the body, including protecting organs and anchoring muscles. Their thin structure makes them prone to fractures(Huelke and Compton, 1983), leading to pain, disability, and complications like internal bleeding or organ damage(Ren et al., 2020). As individuals age, flat bones become more brittle, increasing the risk of fractures(Beedham et al., 2019). Skull fractures, common in head injuries at any age(Carson, 2009), carry a higher mortality rate even when considering trauma severity(Tsai et al., 2022). Aging affects the shape and fragility of calvarial bones(Cotofana et al., 2018)(Torimitsu et al., 2014), but the impact on osteogenic tissues supporting bone repair, such as the calvarial periosteum and suture mesenchyme remains elusive.

In the calvaria, bones form and repair through intramembranous ossification(van den Bos et al., 2008). Osteoblasts which deposit pre-mineralized bone tissue(Bianco and Robey, 2015) arise from $CD90^+$ osteoprogenitor populations(Chan et al., 2015, 2013; Kim et al., 2016), which are derived from heterogeneous populations of skeletal stem cells (SSCs)(Chan et al., 2015, 2013; Kim et al., 2016). Osteoprogenitors reside in soft tissues alongside endothelial and other cell types that interface with mineralized bone tissue. The two

main described osteoprogenitor niches are the periosteum, which overlays all flat bones(Debnath et al., 2018), and the suture mesenchyme, only present in the skull, between calvarial bones(Wilk et al., 2017). Localized Wnt ligands (Wnts) play crucial roles in regulating osteogenesis, influencing stem cells, progenitors, and mature osteoblasts(Garcin and Habib, 2017; Liu et al., 2009; Lowndes et al., 2016; Matsushita et al., 2020; Okuchi et al., 2021). We recently showed that the Wnt3a-bandage, a transplantable polymer that harbors covalently immobilized Wnt3a proteins, combined with an engineered human osteogenic tissue, can promote bone repair in adult immunodeficient mice(Okuchi et al., 2021).

In this study, using a clinically relevant immunocompetent mouse model, we examined how aspects of the periosteum and suture mesenchyme change with age, how they respond to injury, and the influence of localized Wnts throughout aging.

Young mice achieve almost complete bone repair of calvarial defects considered 'critical sized' in adults, which have limited self-healing ability. We found that age-related changes in bone tissue begin to manifest during adulthood, including increased bone porosity, altered cellular mechanical cues, and declines in mitochondrial activity, vascularity, and the proportion and function of $CD90^+$ osteoprogenitor cells within the periosteum and suture mesenchyme. While Wnt bandage increases $CD90^+$cells at the defect site regardless of age, this increase only sufficiently promotes repair comparable to young animals in adult mice, not aged mice. Our study characterized a more pronounced decline in osteogenic compartments in aged mice, encompassing reduced $CD90^+$ cell proportion, function, and mitochondrial bioenergetics, alongside other contributing factors. This multifaceted decline leads to severe age-related bone repair deficiency, only partially alleviated by the Wnt3a-bandage, underscoring the need for combinatorial approaches.

To counteract age-related decline in bone repair, we combined localized Wnt3a stimulation with systemic metabolic interventions. In aged mice with critical-size defects, alternating-day intermittent fasting restored osteogenic compartment health, improving $CD90^+$ cell function as well as bone remodelling and significantly enhanced bone repair to levels comparable to younger animals. This effect was recapitulated by even shorter-term supplementation of the gut bacteria *Akkermansia muciniphila* or nicotinamide mononucleotide (NMN – an NAD^+ precursor) in aged mice, highlighting the multifaceted mechanisms of action of intermittent fasting. We further identify mitochondrial dysfunction as a key component in age-related decline in osteoprogenitor function and show that both cyclical nutrient deprivation or NMN rejuvenate mitochondrial health and enhance osteogenesis *in vitro*.

In summary, our findings highlight that aging tissues retain the potential for health improvements through interventions. Our data reveals an intriguing avenue of research where metabolic and microbiome interventions can be repurposed to treat tissue damage in aged repair-deficient individuals.

Results:

Parietal bone structure deteriorates with aging

Initially, we analyzed the changes that occur in calvarial bone of female C57BL6/J mice during aging at the macro-structure. Female mice were selected for this study due to their distinct characteristics, such as delayed healing and higher fracture risk (Haffner-Luntzer et al., 2021; Ortona et al., 2023), which provide a more challenging model for evaluating bone repair strategies. Young mice (6 weeks) are within the period of fastest bone formation and growth, Adult mice (13 weeks) at healthy homeostasis, and Aged mice (> 88 weeks) correspond to declining skeletal health as a model of >70 year old humans(Dutta and Sengupta, 2016). We evaluated the calvaria of these animals using micro-computed tomography (microCT). The proportion of the total bone volume taken up by mineralized bone tissue (Bone Volume/Total Volume, BV/TV) significantly

decreased with age (**Fig. 1a-b**). Cortical bone mineral density (Ct.BMD), the measure of the density of the mineralized bone tissue alone, showed that Aged mice have similar mineral density to Young and Adult mice (nonsignificant differences). The overall thickness from outer surface to inner surface of the parietal bone significantly increased with age (**Figure 1 – figure supplement 1a-d**).

As parietal bone formation and maintenance is regulated by the cells within the periosteum and suture mesenchyme(Debnath et al., 2018; Li et al., 2021; Maruyama et al., 2016), we next defined the changes that occur within these compartments during aging.

Age-related changes in vascularization, nuclear morphology, F-actin levels and osteoprogenitor proportions in osteogenic compartments

Blood vessels in the calvaria bone support tissue survival by delivering oxygen and nutrients, regulating bone metabolism, and contributing to its maintenance and remodeling, while tissue stiffness influences cell behavior and osteoprogenitors differentiate into cells essential for these processes. Therefore, we aimed to characterize blood vessels, nuclear and cytoskeletal morphology, and osteoprogenitor proportions within the periosteum and suture mesenchyme. Initially, we established that 97% endothelial cells in the periosteum and the suture mesenchyme (osteogenic compartments) express Endomucin and CD31 (**Figure 1 – figure supplement 1e, f**). We found that the proportion of Endomucin-positive ($Emcn^{+}$) blood vessels in the periosteum significantly decreases with age (**Fig. 1c-d, Figure 1 – figure supplement 1g-j**). Further vascular histomorphometry shows that, in the periosteum, blood vessel lumen area is consistent throughout aging, indicating that it is the decrease in the blood vessel number per area of tissue that drives the declining blood vessel density. In addition, we find that the thickness of the periosteum itself also decreases rapidly with age (**Figure 1 – figure supplement 1k, l**). Taking increased periosteum thickness and density of blood vessels into account, the estimated blood supply (vessel density multiplied by periosteum thickness) of the whole Young periosteum is over 12-fold higher than that of Aged periosteum. In the suture mesenchyme, blood vessels are larger than in the periosteum, and overall, the vascularization remains stable throughout aging (**Figure 1 – figure supplement 2a, b**).

Vascular phenotypes can be influenced by tissue mechanics (Xie et al., 2018). Therefore, we aimed to measure mechanically-driven aspects of cellular morphology in periosteal and suture mesenchymal cells during aging. Nuclear shape is a product of intracellular(Dahl et al., 2008) and extracellular factors, such as the stiffness of the surrounding matrix(Lovett et al., 2013). Morphologically and confirmed by the mean Nuclear Aspect Ratio (NAR, long axis length divided by short axis length) we found significant elongation of nuclei in Aged mice periosteum and to a lesser extent, in the suture mesenchyme (**Fig. 1e-f**). Lamin B1, a key nuclear lamina protein involved in regulating nuclear function and organization, showed no significant changes across age groups(bin Imtiaz et al., 2021; Kim, 2023; Tran et al., 2016) (**Figure 1 – figure supplement 2i-j**)

Nuclear morphology is frequently interlinked with actin cytoskeleton organization, influencing cell migration, proliferation(Ambriz et al., 2018) and the response to mechanical force imparted on them through the extracellular matrix(Fletcher and Mullins, 2010; Stricker et al., 2010). We quantified filamentous actin (F-actin) using fluorescent-Phalloidin staining in periosteum and suture mesenchyme (**Fig. 1g-h, Figure 1 – figure supplement 2h**). Aging led to a progressive increase of F-actin, peaking at a 2.5-fold rise between young and Aged mice in suture mesenchyme.

Beyond morphological and cytoskeletal changes, we questioned whether aging periosteal cells experience changes to their cellular energy supply. Adenosine triphosphate (ATP) generation, crucial for cell function, relies largely on mitochondrial membrane potential(Zorova et al., 2018). This can be measured by determining the intensity of Tetramethylrhodamine, methyl ester (TMRM), which accumulates in active mitochondria with

intact membrane potentials in live cells(Creed and McKenzie, 2019). *Ex vivo* TMRM intensity was significantly higher in freshly-harvested samples of Young mouse periosteum, than in Adult and Aged mice (**Fig. 1i-j**). This finding is unlikely to be an artefact of differential ECM densities interfering with diffusion as performing the same experiment in explanted cells (i.e. without ECM, **Figure 1 – figure supplement 2c, d**) gave a similar trend of results. We also confirmed equal Hoechst diffusion and staining throughout the *ex vivo* tissue experiment (**Figure 1 – figure supplement 2e, f**).

Given these age-related differences in the osteogenic compartments, we aimed to elucidate changes to the $CD90^+$ osteoprogenitors (Chan et al., 2015 ; Kim et al., 2016), (**Figure 1 – figure supplement 2g**). Using in situ immunofluorescence, we found that the proportion of $CD90^+$ in the periosteum and the suture mesenchyme significantly decreases with age, with only around one third retained in Aged mice in each compartment (**Fig. 1k-l**).

These tissue and cell-level changes indicate a significant and multifaceted age-related decline in the calvarial osteogenic compartments. The periosteum and the suture mesenchyme also serve as the primary sources of cells that contribute to osteogenesis during calvarial bone repair(Jeffery et al., 2022; Wilk et al., 2017). Hence, we next characterized how calvarial bone repair is affected by age and how the nearby cells respond to the Wnt3a-bandage.

Wnt3a-bandages increase $CD90^+$ cells in repair areas of Aged and Adult mice and enhance bone repair

Critical-sized calvarial bone defects, challenging to heal without intervention, serve as models to quantitatively evaluate bone repair. Our prior work demonstrated that applying a Wnt3a-bandage and cellular osteogenic construct to the defect site significantly enhances bone repair in adult immunocompromised mice(Okuchi et al., 2021). Considering the crucial role of the immune system in bone healing(Loi et al., 2016) and the prevalence of bone fractures in immunocompetent individuals, we assessed bone repair in female wildtype (C57BL6/J) mice of varying ages. Mice underwent bilateral critical-sized (2 mm) full-thickness calvarial defect surgery in the parietal bones and were treated with one active Wnt3a-bandage and one chemically-inactivated Wnt3a control bandage. Wnt3a-bandage activity was confirmed *in vitro* (**Figure 1 – figure supplement 3a-c**) before transplantation.

We assessed bone repair by measuring the area percentage of re-mineralized tissue within the defect site using microCT after 10 weeks. Interestingly, Young mice exhibited robust bone healing even without intervention, highlighting the natural regenerative capacity of bone in young mice. (**Fig. 1o-p, Supplementary File 1**). In adult mice, Wnt3a-bandage treatment significantly enhanced bone repair compared to the control bandage, achieving levels comparable to those observed in young mice. Aged mice exhibited severely impaired repair with both bandages, though Wnt3a-bandage showed a modest but significant increase. New bone formed under Wnt3a-bandage displayed improved lamellar structure (striations) akin to mature undamaged bone (**Figure 1 – figure supplement 3d**).

To uncover cellular mechanisms behind the improved healing, we examined $CD90^+$ osteoprogenitor cells in the defect site. The proportion of $CD90^+$ cells was significantly increased by the Wnt3a-bandage across age groups, compared to control bandages (**Fig. 1m-n**). Wnt3a-bandages locally increase $CD90^+$ cells, but despite similar numbers across ages, the effect of the Wnt3a-bandage on bone repair in Aged mice was limited. We hypothesized, therefore, that the functionality of $CD90^+$ cells, rather than their number alone, may drive age-related differences in bone repair outcomes.

To investigate this, we initially examined the influence of the Wnt-bandage on $CD90^+$ cells across various age groups in terms of Wnt/β-catenin signaling. The proportion of nuclear β-catenin (**Figure 1 – figure supplement 4a-c**), indicative of Wnt/β-catenin signaling activation(Archbold et al., 2012), was significantly

increased in CD90$^+$ cells near the active Wnt3a-bandage compared to the inactive bandage. Importantly, the proportion of nuclear β-catenin remained similar regardless of age, suggesting the Aged CD90$^+$ have the capacity to activate the pathway similar to younger CD90$^+$ cells.

We then explored the effects of the Wnt3a-bandage on CD90$^+$ cell proliferation and migration near the bandage. Our results demonstrate that the proportion of CD90$^+$ stained with the proliferation marker Ki67 or MMP2, a Type IV collagenase enzyme linked to migration(Ries et al., 2007) and ECM remodeling in flat bones (Egeblad et al., 2007; Mosig et al., 2007; Zhong-Sheng et al., 2022), appeared increased in CD90$^+$ near Wnt3a-bandage. While this increase was not statistically significant compared to inactive control bandage groups in Aged mice, it was statistically significant in Adult mice (**Figure 1 – figure supplement 4b-e**).

Considering that CD90$^+$ cells inside the defect are ultimately derived from cells that are harbored in the nearby periosteum and suture mesenchyme, we next analyzed the transcriptomes of CD90$^+$ to glean insights into their functional differences during aging.

Transcriptional shifts occur in calvarial CD90$^+$ cells with aging

Single-cell RNA sequencing (scRNAseq) was performed on live cells immediately following dissection and tissue digestion from the periosteum and suture mesenchyme in Young, Adult, and Aged mice, with data processing to deplete immune (CD45$^+$) cells. CD90$^+$ subpopulations of cells (cluster 0, 1 and 3 in the periosteum; cluster 10 in the suture mesenchyme) were identified within both tissues (**Figure 2 – figure supplement 1a-h**), with high transcriptomic similarity to cells expressing Prrx1,Cathepsin K (Ctsk) and Ddr2(Bok et al., 2023; Debnath et al., 2018) (**Figure 2 – figure supplement 2**), markers of periosteal and suture SSCs(Duchamp de Lageneste et al., 2018; Wilk et al., 2017). We also found that the CD90$^+$ population includes minor subsets of cells that express other SSC/progenitor markers including CD200/CD51 (Cd200/Itgav)(Menon et al., 2021), Gli1(Zhao et al., 2015), Axin2(Maruyama et al., 2016) and α-SMA (Acta2)(Ortinau et al., 2019). Therefore, based on functional studies(Kim et al., 2016; Nusspaumer et al., 2017) and our transcriptomic analysis, the CD90$^+$ population encompasses a heterogeneous group of cells that are capable of osteogenic differentiation. Next, we will describe selected transcriptomic changes in CD90$^+$ cells during aging. For Gene ontology number, comparisons and statistics, please see **Supplementary File 2**.

Comparing Young CD90$^+$ cells with Aged CD90$^+$ cells in the periosteum (**Figure 2 – figure supplement 3a**), 542 genes were significantly upregulated. Of these, 38 corresponded to Gene Ontology (GO) term 'Cytosolic ribosome', linked to increased 'Collagen-containing extracellular matrix'. Similarly in Young vs Aged suture CD90$^+$ cells (**Figure 2 – figure supplement 3b**), 879 significantly upregulated genes are enriched for 'Structural constituent of ribosome' and 'Extracellular matrix structural constituent'. Young mice at 6 weeks of age undergo significant skeletal growth(Jilka, 2013), hence this data closely corroborates the increase in collagenous matrix deposition (both soft and bone tissue) observed in histological sections of bone defects in Young mice.

Given the effect of the Wnt3a-bandage on the Aged bone repair environment, we next probed the differentially expressed genes for components of the Wnt/β-catenin pathway. The transcript's expression of Wnt2 ligand, often implicated in the Wnt/β-catenin pathway(Goss et al., 2009; Jung et al., 2015), was significantly downregulated with age in suture CD90$^+$ cells (**Figure 2 – figure supplement 3b,d**). Further, Wnt co-receptor Lrp6 expression significantly declined with age in periosteal CD90$^+$ cells (**Figure 2 – figure supplement 3a**). Collectively, this suggests compromised Wnt signaling in the periosteum and suture mesenchyme during aging.

At the Adult and Aged timepoints, bone is at healthy and declining homeostasis, respectively. We compared Adult and Aged CD90$^+$ cells in the periosteum (**Figure 2 – figure supplement 3c**). Here, the 637 genes significantly upregulated in Adult vs Aged were vastly enriched for GO terms 'NADH dehydrogenase complex assembly', 'NADH dehydrogenase (ubiquinone) activity' and 'Oxidative phosphorylation'. Likewise, in the suture mesenchyme (**Figure 2 – figure supplement 3d**), the 610 genes significantly upregulated in Adult vs Aged CD90$^+$ cells were also enriched for 'Mitochondrial ATP synthesis coupled proton transport' and 'Oxidative phosphorylation'. Using the UCell method(Andreatta and Carmona, 2021), we found significantly reduced Complex I gene scoring with age in the suture mesenchyme and the periosteal CD90$^+$ cells (**Figure 2 – figure supplement 3e-f**). These results, coupled with live measurements of mitochondrial membrane potential (**Fig. 1i-j**), indicate an age-related decline in mitochondrial metabolism and electron transport chain (ETC) complexes within CD90$^+$ cells of the whole periosteum and suture mesenchyme. Importantly, we did not observe distinct changes in the signature of Glycolysis or lipid metabolism across age groups in CD90$^+$ cells in the osteogenic compartments (**Figure 2 – figure supplement 3j-m**).

Analysis with the CellChat package(Jin et al., 2021) shows inferred signaling heterogeneity within the periosteal CD90$^+$ population (**Figure 2 – figure supplement 4a**). Cells within the smaller CD90$^+$ cluster (cluster 3, **Figure 2 – figure supplement 1a-d**) receive incoming Wnt-signals and also Periostin-signalling, which upregulates Wnt/β-catenin pathway activity in osteogenesis(Lv et al., 2015; Zhang et al., 2017). This cluster is significantly upregulated for markers of osteogenic differentiation such as Runx2, Mme (Osteonectin/CD10)(Ding et al., 2020; Granéli et al., 2014), Bgn(Ye et al., 2012), Mgp(Zhang et al., 2019), Gas6(Shiozawa et al., 2010), and Igbp7(Zhang et al., 2018), and is hereby termed the P1 CD90$^+$ population. Cells within the larger cluster (clusters 0 & 1) both send and receive Periostin and Wnt-signals, and is significantly upregulated for markers associated with stemness, such as Klf4 and Aldh1a3(Wanandi et al., 2018), and negative regulators of osteogenic differentiation such as Bmp3(Kokabu et al., 2012), and Ccn3(Matsushita et al., 2013). Hereby these cells were termed P2 CD90$^+$.

The periosteal P2 CD90$^+$ cell population shifts with age between two categories, named 'Igf1^{high}' and 'Igf1^{low}' in relation to their differential expression of Igf1 (**Fig. 2a-c**). Igf1 is linked to bone anabolism through its dual roles in enhancing Wnt-signaling and exerting metabolic effects(Locatelli and Bianchi, 2014). Young P2 CD90$^+$ cells were restricted to the Igf1^{high} grouping (92.0%), while Aged CD90$^+$ cells were predominantly in the Igf1^{low} grouping (66.3%) (**Fig. 2a-b**). Adult CD90$^+$ cells were more evenly split (56.8% Igf1^{high}, 43.2% Igf1^{low}). Igf1^{low} cells were significantly upregulated for 85 genes (**Fig. 2c**), linked 'Cell motility', driven by genes such as Mmp14(Almalki and Agrawal, 2016) and Itgb7(Novoseletskaya et al., 2020). Igf1^{high} cells were significantly upregulated for 204 genes linked to 'Collagen-containing extracellular matrix', 'Oxidative phosphorylation' and 'Respiratory chain complex'. The enrichment is driven by significantly upregulated genes such as NADH dehydrogenase genes (mt-Nd1 & mt-Nd2), Col1a1, Sparc.

Likewise, in the suture mesenchyme, analysis of inferred cellular state and function (**Fig. 2d-e**) revealed a distinct subpopulation of CD90$^+$ cells. This group of cells was significantly upregulated for 855 genes linked to 'Mitotic cell cycle' and 'ATP-dependent activity'. In Young mice, this population, termed 'Proliferating' cells, represented 48.72% of the CD90$^+$ population, whereas it markedly declined to around 8% in both Adult and Aged mice (**Fig. 2d-e**).

When comparing CD90$^+$ cell populations between every two age stages, several genes are conserved in all three comparisons (**Figure 2 – figure supplement 4b, c**), including: Cavin1(Volonte and Galbiati, 2020), S100a4(Wagner et al., 2009), Vcan(S. Li et al., 2019), Mmp14(Haage et al., 2014), and Nsg1(Wiese et al.,

2019). Each of these genes has been identified as being involved in senescence or the cellular response to aging tissues. Likewise, in the suture CD90$^+$ cells, conserved aging-related genes included senescence-related genes Pim1(Yang et al., 2017), Pdcd4(Kang et al., 2002); and the senescence-associated secretory profile (SASP) gene Ccl6(Gillispie et al., 2021). Further comprehensive senescence signature confirms the significant increase associated with age in CD90$^+$ cells (**Figure 2 – figure supplement 4d**). Also conserved were: pro-bone resorption Mmp9(Zhu et al., 2020), and adipogenesis-related genes ApoD(Provost et al., 1991) and Slc16a3 (MCT4)(Petersen et al., 2017).

Aging calvarial CD90$^+$ cells undergo a decline in energy supply, proliferation, Wnt/β-catenin, and ECM remodeling capacity

Next, we aimed to investigate the transcriptionally-identified decline in energy supply, proliferation, Wnt/β-catenin pathway, and migration in CD90$^+$ cells at the protein level through immunofluorescent staining of marker proteins.

The catalytic beta subunit of ATP synthase (ATPB), an essential component of the mitochondrial ATP synthesis machinery, serves as a marker for assessing energy-related mitochondrial function(H.-S. Li et al., 2019). Cellular ATPB levels in suture mesenchyme CD90$^+$ cells is similar across age groups, but in the periosteal CD90$^+$ cells, ATPB level is lower in Aged mice compared to Adults (**Fig. 2f, l**). Phosphorylated AMPK (phospho-AMPK), a sensor of ATP depletion(Gowans and Hardie, 2014), exhibits a negative correlation with energy availability. In both periosteum and suture CD90$^+$ cells, mean phospho-AMPK was significantly higher in Aged mice (**Fig. 2g, l**). Taken together, these findings suggest a potential deficiency in oxidative phosphorylation machinery in CD90$^+$ cells with age.

Ki67 marks active proliferation, while cyclin-dependent kinase inhibitors p16 is involved in various cellular functions and is linked to senescence and aging in several tissues(Safwan-Zaiter et al., 2022; Stein et al., 1999, p. 199). Calvarial CD90$^+$ cells were assessed for nuclear expression of the two markers. Ki67$^+$ CD90$^+$ cells were observed in the periosteum of both Young and Adult mice but not in Aged mice. In the suture, the proportion of Ki67$^+$ CD90$^+$ was significantly higher in Young than in Adult mice with none detected in Aged mice (**Fig. 2h, l**). The proportion of p16$^+$ CD90$^+$ cells appeared to increase with Age (**Fig. 2i, l**). Together, nuclear p16 expression and a lack of Ki67 expression suggests that Aged CD90$^+$ cells are not actively proliferating, corroborating inferred findings from transcriptomics.

Next, we assessed the level of nuclear β-catenin, an indicator of Wnt/β-catenin pathway activation. Aged CD90$^+$ cells in both periosteum and suture mesenchyme showed significantly reduced nuclear localization of β-catenin compared to Young (**Fig. 2j, l**). Only Adult CD90$^+$ cells in the periosteum had significantly higher nuclear β-catenin when compared to Aged mice.

Finally, in both periosteum and suture mesenchyme, Aged CD90$^+$ cells expressed the lowest amounts of MMP2 (**Fig. 2k-l**). While MMP2 is a secreted protein, only intracellular protein was quantified, to enable the analysis to be restricted to MMP2 expressed by CD90$^+$ cells alone. It corroborates the downregulation of genes associated with migration in the transcriptomic analysis.

Overall, our protein-level analysis largely aligns with the transcript-level findings, insinuating that age-related alterations in periosteum and suture mesenchyme, and consequently bone repair, could be considerably impacted by metabolic differences within the CD90-expressing population.

Given that increasing the number of CD90$^+$ cells inside the defect alone produced only a minor improvement to Aged bone repair, we developed a systemic approach to target cellular metabolism. We aimed to combine this systemic approach with the use of the Wnt3a-bandage to ultimately facilitate the supply of competent osteogenic cells for bone repair.

Intermittent Fasting improves bone health and bone repair in Aged mice

Intermittent fasting (IF) can improve metabolic control by various measures(Longo et al., 2021) and bone mineral density in adult animals (Veronese and Reginster, 2019). We produced critical-sized calvarial defects in Aged mice, treated them with Wnt3a-bandages and inactive controls. These mice were then maintained on an alternating-day diet of self-limited feeding and complete fasting, hereby termed the intermittent fasting diet. Importantly, over the course of a week, mice intake the same amount of food during the IF diet as during the self-limited feeding controls (*ad libitum*, AL) diet (**Figure 3 – figure supplement 1a-c**), and is therefore distinct from an overall reduction in calories (i.e., caloric restriction). Fasting blood glucose levels and the area under the curve (AUC) from the intraperitoneal glucose tolerance test (IPGTT) were significantly lower in mice following an IF diet compared to those on an AL diet (**Figure 3 – figure supplement 1d-g**). These results indicate improved insulin sensitivity, enhanced glucose metabolism, and better overall metabolic control(Andrikopoulos et al., 2008; McGuinness et al., 2009; Nakrani et al., 2024).

Remarkably, Aged mice subjected to the IF diet repaired 59.24% of the defect within 10 weeks under the inactive bandage, higher even than that of Adult mice + inactive bandage (**Fig. 1o-p**). With the addition of the Wnt3a-bandage, bone repair area was increased to 67.10%. This combination approach of the local Wnt3a-bandage and post-fracture IF results in Aged calvarial bone repair rivaling that of Young mice. The IF diet also significantly increased the solid bone proportion (BV/TV) (**Fig. 3a-b**), making it similar to the much younger Adult bone.

Intermittent Fasting reverses aspects of cellular and tissue aging in the periosteum and suture mesenchyme

Compared to Aged mice, in Aged + IF, Emcn$^+$ vascularity in the periosteum was significantly increased (**Fig. 3c-d**). Additionally, in the suture mesenchyme, actin cytoskeleton staining was markedly decreased (**Fig. 3e-f**), along with a significant reduction in age-related nuclear elongation both in the suture and periosteum (**Fig. 3g-h**). The IF diet did not impact Lamin B1 protein levels (**Figure 1 – figure supplement 2i-j**). The IF diet appeared to elevate the proportion of CD90$^+$ cells in the periosteum, while in the suture it significantly increased compared to AL (**Fig. 3i-j**).

To gain a deeper understanding of how IF affects Aged CD90$^+$ cells, we conducted further scRNAseq analysis. We maintained Aged mice on the alternating-day IF diet for 10 weeks before performing scRNAseq on the periosteum and suture mesenchyme (**Source Data 2 – Supplementary Tables 9,10,12**).

Comparing CD90$^+$ cells of Aged periosteal post IF diet with Aged AL diet controls revealed 98 significantly upregulated genes (**Fig. 4a**). These were enriched mainly for ‘Response to cytokine’ and similar GO terms. Of the genes upregulated with the IF diet, 10 were individually statistically significant when adjusting for false discovery rate ($q < 0.05$). Ccl11 and Duox2 are involved in osteogenic stem cell migration(Smith et al., 2012; Tyurin-Kuzmin et al., 2016), Tnfaip6 and Ccl7 in immunomodulation(Li et al., n.d.; Rafei et al., 2008), Ptx3 is involved in both processes(Cappuzzello et al., 2016), and Actg1 in cytoskeletal structure(Dugina et al., 2009; Simiczyjew et al., 2014). Zbtb16, encoding transcription factor PLZF, regulates osteogenesis by acting upstream of master osteoblast transcription factor Runx2 (**Figure 2 – figure supplement 3i**)(Agrawal Singh et al., 2019; Liu and Lee, 2013).

In the suture mesenchyme, analysis of 297 significantly upregulated genes in Aged CD90$^+$ cells during the IF diet compared to Aged AL control (**Fig. 4b**) showed enrichment in 'Mitotic cell cycle' and 'Protein phosphorylation'. Notably, the proliferation marker Mki67 is significantly upregulated, with a threefold increase in Aged periosteum CD90$^+$ cells during intermittent fasting compared to ad libitum diet.

Intermittent fasting also showed an upregulation of Dbp, Tef, and Hlf, an effect that was conserved between osteoprogenitor compartments in Aged mice. (**Figure 2 – figure supplement 3g-h, Supplementary File 2**). These genes are part of the transcriptional effectors of the circadian transcriptional network (Gachon et al., 2004), which act by binding to D-box sites in gene promoters (Yoshitane et al., 2019). In suture Aged CD90+ cells during the IF diet, Dbp alone is significantly upregulated against Aged AL CD90+ cells. Several other genes under circadian control (e.g., Sirt1, Kat2b, Csnk1e, Ezh2, Fbxw11, Ucp2; all $p < 0.05$) are upregulated in Aged suture CD90+ cells during the IF diet. This corresponds to an enrichment of the transcriptional targets of Clock/Per2/Arntl, which together form the network of transcription factors responsible for maintaining circadian rhythms.

In **Fig. 2a**, a shift in the periosteal CD90$^+$ was noted with aging. Aged AL had relatively fewer osteogenic Igf1^{high} cells, and more of Igf1^{low} cells. Contrary, Aged + IF CD90$^+$ cells were split 70.3% Igf1^{high}, 29.7% Igf1^{low} (**Fig. 4c-d**), positioning them between Young and Adult distributions. 2 of the 14 genes identified as conserved markers of periosteal CD90$^+$ cell aging (**Figure 2 – figure supplement 4b**), Vcan, Mmp14, were significantly downregulated in Aged + IF. The proportion of 'proliferating' CD90$^+$ suture cells increased in Aged + IF (**Fig. 4e-f**). Further, 1 of the 32 conserved genes of the aging suture (**Figure 2 – figure supplement 4c**), actin-associated Tpm1(Li et al., 2022), was significantly downregulated in Aged + IF. Wnt2, found to be downregulated with aging, is significantly upregulated in the suture CD90$^+$ population of Aged + IF (**Source Data 2 – Supplementary Table 10**).

To validate diet-induced changes in CD90$^+$ cells, we conducted immunostaining for protein markers in histological sections. ATPB, marker of ATP synthase, appeared elevated in periosteum and significantly increased in suture mesenchyme CD90$^+$ cells following IF (**Fig. 4g-m**). This suggests an increase in cellular ATP levels, which is supported by decreases in ATP-deficiency sensor phospho-AMPK in periosteal and suture CD90$^+$ cells (**Fig. 4h, m**). While proliferating cells were absent in Aged mice, we observed Ki67$^+$ cells in samples of the periosteum of 3 out of 5 Aged + IF mice and in 4 out of 5 Aged + IF mice for suture mesenchyme (**Fig. 4i, m**). Conversely, p16 was similar in periosteum and suture mesenchyme (**Fig. 4j, m**). Wnt/βcatenin pathway activity, as measured by the relative nuclear localization of β-catenin, was significantly increased within the CD90$^+$ cells of both the periosteum and suture (**Fig. 4k, m**). Lastly, expression of the motility marker MMP2 in CD90$^+$ cells was markedly increased over Aged controls in the periosteum, and just under statistical significance in the suture mesenchyme (**Fig. 4l, m**).

Together, these findings suggest that IF rejuvenates aged CD90$^+$ cells, in part, by enhancing proliferation, immune response, ECM remodeling, Wnt/β-catenin pathway, and metabolism, including increased ATP levels and decreased AMPK levels.

Short term metabolic approaches rejuvenate the calvarial osteogenic compartments of Aged mice and promote bone repair

IF diet likely enhances energy supply to CD90$^+$ cells and their function through various mechanisms. We next aimed to determine if specific underlying mechanisms alone could replicate the effects of IF on aged bone

425 repair. Our analysis revealed that both aging and IF affect the NAD^+ biosynthesis pathway and gut microbiota.
426 Thus, we targeted these aspects to investigate their potential to enhance aged bone repair.
427
428 *NMN supplementation improves bone repair in Aged mice*
429 NAD^+ is a multifunctional enzyme co-factor with roles including protein deacetylation, histone modification,
430 intracellular signaling, and redox reactions (Covarrubias et al., 2021). It is also crucial in oxidative
431 phosphorylation(Stein and Imai, 2012), cycling between oxidized and reduced forms (NAD^+/NADH) in the
432 mitochondria as part of the electron transport chain. Our analysis of inferred NAD^+-dependent pathway activity
433 (**Figure 2 – figure supplement 3d, Source Data 2 – Supplementary Table 4**), live mitochondrial activity
434 (**Fig. 1i-j**), and markers of cellular energy levels (**Fig. 2f, g, l**) demonstrated distinct changes to metabolism
435 with age. Yet, little is known about the effect of NAD^+-coupled cellular metabolism on the composition of aging
436 calvarial periosteum and suture mesenchyme and its influence over Aged bone repair.
437
438 To increase cellular levels of NAD^+ systemically, we orally dosed Aged mice with nicotinamide mononucleotide
439 (NMN), an immediate precursor to NAD^+ in the 'salvage' pathway(Yang and Sauve, 2016). During a pilot study
440 involving oral NMN supplementation (600 mg/kg, 3 times within 1 week) in Adult mice, the mitochondrial
441 membrane potential, as measured by TMRM staining, within the cells of the periosteum was significantly
442 increased (**Fig. 5a, b**). NMN was then administered to Aged mice for the 2 weeks prior and 2 weeks following
443 calvarial defect surgery.
444
445 Parietal bone BV/TV was significantly increased in Aged animals that received NMN (Aged + NMN) (**Fig. 5c-**
446 **d**). Remarkably, Aged bone repair was significantly increased to 54.32% with NMN with inactive bandages
447 (**Fig. 1o-p**), marking a three-fold improvement over control Aged mice. Adding Wnt3a-bandage increased
448 Aged + NMN repair to 71.18%, resulting in over 2.71 times greater area of new bone compared to Aged
449 controls + Wnt3a-bandage, akin to repair in Adult mice + Wnt3a-bandage.
450
451 Next, we probed how NMN affects $CD90^+$ cells in the osteogenic compartments. In the suture mesenchyme,
452 NMN treatment significantly increased $CD90^+$ cells compared to Aged control (**Fig. 5e-f**). In the periosteum,
453 $CD90^+$ populations were unchanged. Additionally, compared to Aged controls, NMN supplementation
454 significantly increased the vascularity of the periosteum (**Fig. 5g-h**), and approximately halved actin
455 cytoskeletal staining intensity in the suture mesenchyme (**Fig. 5i-j**). Nuclei in the suture and periosteum were
456 rounder and less elongated than Aged controls (**Fig. 5k-m**), making them morphologically resemble Adult
457 nuclei.
458 Taken together, NMN treatment increased periosteal vascularity, impacted aspects of tissue mechanics of the
459 periosteum and suture mesenchyme, leading to a significant improvement in bone repair in Aged mice.

460 *Cyclical nutrient deprivation and NMN enhance mitochondrial function in osteogenic cells in vitro*

461 Next, we aimed to model aspects of the effects of intermittent fasting and NMN supplementation on osteogenic
462 cells, employing a cyclical nutrient deprivation regimen or NMN supplementation *in vitro* to elucidate aspects
463 of their mechanisms of action. While this approach allows us to study specific cellular responses, it is crucial
464 to recognize that it cannot fully replicate the complex systemic effects of *in vivo* intermittent fasting.
465 We investigated the impact of these interventions on mitochondrial function in the MC3T3 calvarial
466 osteoblastic cell line, a model commonly utilized to study osteogenesis *in vitro* and known for its ability to
467 contribute to bone formation *in vivo*(Horowitz et al., 1994; Paine et al., 2018; Wang et al., 1999) .
468

Alternating serum deprivation every hour (cyclical nutrient deprivation) in pyruvate and glucose-free medium induced the expression of genes related to mitochondrial biogenesis, fusion, mitophagy, and the unfolded protein response (**Fig. 6a**). This was accompanied by increased mitochondrial filament length and membrane potential, indicating enhanced mitochondrial function(McCarron et al., 2013; Westermann, 2012) (**Fig. 6b-e**). These findings are consistent with our *in vivo* observations of improved mitochondrial function in animals subjected to intermittent fasting. While cyclical nutrient deprivation enhanced mitochondrial membrane potential, it also reduced overall cellular ATP levels. However, inhibiting mitochondrial ATP production with oligomycin (a Complex V inhibitor)(Devenish et al., 2000) further diminished ATP levels, suggesting that mitochondrial respiration is a primary source of ATP in these cells (**Fig. 6f**).
Recognizing the role of mitochondrial dysfunction in aging, we investigated the impact of NMN on MC3T3 cells challenged with oligomycin and cultured in glucose and pyruvate-free medium. NMN treatment mitigated oligomycin-induced ATP loss and ROS production, enhanced cell proliferation, and prevented the loss of mitochondrial membrane potential (**Fig. 7a-c**). Holotomography microscopy revealed that NMN preserved the "rod-like/filament" morphology of mitochondria in oligomycin-treated cells (**Fig. 7d-e**). Furthermore, NMN restored the expression of genes related to mitochondrial biogenesis and dynamics, the unfolded protein response, and mitophagy, which were adversely affected by oligomycin (**Fig. 7f**). Ultimately, NMN enhanced the growth and differentiation potential of oligomycin-treated cells, as evidenced by increased ALP activity and mineralization (**Fig. 7g**).

In summary, our findings suggest that both cyclical nutrient deprivation and NMN supplementation can enhance mitochondrial function in osteogenic cells. NMN appears to protect against mitochondrial dysfunction induced by Complex V inhibition, highlighting its potential in mitigating the decline in osteogenic cell function.

Akkermansia muciniphila supplementation improves bone repair in Aged mice

The ‘gut-bone axis’ links food intake, gut microbiome and bone metabolism via circulating metabolites(Villa et al., 2017). Bacteria in the genus *Akkermansia* appeared to be elevated during Aged + IF compared to the AL control diet (**Fig. 5n**), consistent with previous studies that found similar results in young mice and human(Li et al., 2020; Özkul et al., 2019).

Akkermansia muciniphila is an anaerobic gut bacterium responsible for mucin turnover(Derrien et al., 2008), and a regulator of the intestinal mucus environment(Reunanen et al., 2015). The *Akkermansia* population exerts wider effects on the gut microbiome, and has been studied for its roles in metabolic health(Dao et al., 2016; Leite et al., 2021). We cultured *Akkermansia muciniphila* (Akk) under anaerobic conditions and calculated the viability of cryopreserved aliquots. Doses of live Akk (2×10^8 C.F.U.) were given by oral gavage three times per week in Aged mice for the 2 weeks prior and 6 weeks following calvarial defect surgery.

Our metagenomic analysis reveals that Firmicutes:Bacteroides ratio, indicator of microbiome composition(Magne et al., 2020), is significantly increased in Aged mice with *Akkermansia* supplementation (Aged + Akk) (**Figure 5 - figure supplement 1a**). Furthermore, the proportion of gut bacteria belonging to family *Lachnospiraceae,* indicative of the capacity of the gut bacteria to produce short chain fatty acids (SCFAs), is significantly elevated in Aged + Akk (**Figure 5 - figure supplement 1b**). SCAFs enter the host bloodstream and exert epigenetic effects primarily through histone modification, which might have implication on cell function and differentiation(Licciardi et al., 2011).

Similar to NMN treatment, parietal bone BV/TV was significantly increased Aged +Akk (**Fig. 5c-d**). Aged bone repair was significantly increased to 43.76% with Akk and inactive bandages (**Fig. 1o-p**). In combination with the Wnt3a bandage effect, bone repair in Aged + Akk further increased to 64.84%. This level of bone repair is

similar to that of Young mice with Wnt3a-bandage (**Supplementary File 1**). Aged + Akk also produced striated bone, similar in structure to Young mice, under both Wnt3a and control bandages (**Figure 1 - figure supplement 3d**).

Aged + Akk led to a significant increase in $CD90^+$ cells in the periosteum and suture mesenchyme (**Fig. 5e-f**) and a threefold increase in the $Emcn^+$ vascularity area of the periosteum (**Fig. 5g-h**). Compared to Aged controls, in Aged + Akk, actin cytoskeletal staining intensity appeared reduced (not significant) in the suture mesenchyme (**Fig. 5i-j**), and nuclei in both the suture and periosteum appeared rounder and less elongated (**Fig. 5k-m**). Accordingly, the nuclear morphology of Aged + Akk cells resembles that of younger mice.

In summary, we have revealed a multifaceted decline in $CD90^+$ cells with aging, which can be locally counteracted by a Wnt3a-bandage or systemically enhanced through an IF diet. Moreover, systemic interventions, acting via the gut and on shorter terms, can improve $CD90^+$ populations, osteogenic compartments, and significantly enhance bone repair in Aged mice. Combining the Wnt3a-bandage with systemic interventions targeting cellular energy supply, proliferation, migration, and Wnt signaling presents coordinated and clinically relevant approaches, promising rejuvenation of Aged bone repair comparable to younger individuals.

Discussion

Here we report on systemic interventions that can reverse aspects of the aging osteogenic tissue to promote effective calvarial bone repair (**Appendix 2 – figure 1**).

While extensive research focuses on long bones(Yates et al., 2007), there is a significant gap in understanding aging in flat bones. Our study on the calvaria demonstrates a clear decline in both bone structure and healing capacity with age. We observed a progressive decline in periosteal blood vessel density beginning in adulthood. Microvascular rarefaction is increasingly recognized as a driver, rather than merely a consequence, of hallmarks of cellular aging, such as cellular senescence(Goligorsky, 2010; Lähteenvuo and Rosenzweig, 2012). Indeed, previous studies inducing vasculature loss in young animals accelerates cellular aging(Chen et al., 2021), while mitigating this vascular decline preserves tissue health and delays aging(Grunewald et al., 2021). Vascularization and modulation of blood flow are critical for calvarial bone repair (Holstein et al., 2011; Huang et al., 2015; Ren et al., 2024). Early in the repair process, periosteal blood vessels grow independently of osteoprogenitor cells, establishing a supportive environment that promotes osteoprogenitor migration and subsequent ossification (Bixel et al., 2024). Compromised vascularization significantly impairs the healing of critical-sized calvarial defects (Caliaperoumal et al., 2018).

Aging bone tissues are inherently more hostile and pro-apoptotic(Almeida, 2012), leading to limited success with cell-based repair approaches in aged individuals(Hirata et al., 2022; Liu et al., 2018). Stiffness increases with aging in various tissues(Ferrari and Pesce, 2021; Lim and Ito, 2022; Segel et al., 2019), impacting cytoskeletal configuration(Khan et al., 2020; Pongkitwitoon et al., 2016) and significantly affecting osteogenic differentiation and senescence *in vitro*(Liu et al., 2022). Our study shows increased actin expression and elongated nuclear shape in aging osteogenic compartments, alongside elevated levels of Mmp9 and Mmp14, linked to stiffer osteogenic tissues(Tang et al., 2013; Zhu et al., 2020). These changes are associated with a decline in both the number and function of osteoprogenitors, including impaired proliferation, mitochondrial energy metabolism, Wnt/β-catenin pathway activation, migration, and ultimately, bone defect repair. While Wnt-bandage treatment increases the number of osteoprogenitors in the defect site across all age cohorts, it only modestly enhances bone repair in aged animals compared to the healing observed in adult mice.

We show that interventions improving whole-body energy metabolism can enhance aged bone health and repair. While IF is effective in delaying aging in adult flies, animals need to switch back to *ad libitum* feeding at older ages(Catterson et al., 2018), and increased protein intake is suggested for optimizing health span

and longevity in aged mice and humans(Levine et al., 2014). Our findings, however, reveal a distinct paradigm for IF in aged bone repair. Specifically, short-term IF initiated post-injury robustly enhances bone healing in aged animals, comparable to younger counterparts.

Mechanistically, IF exerts its effects through several pathways, including enhanced stress resistance, increased reliance on lipid fuel utilization, and activation of proteostatic mechanisms, all contributing to delayed aging(Longo and Anderson, 2022). Although we did not observe distinct changes in overall signature of lipid metabolism or glycolysis in osteogenic tissues during aging or IF, we did find a decline in mitochondrial function and ATP supply with age. Our *in vitro* studies showed that alternating cycles of serum deprivation and supply in osteogenic cells induced genes related to the unfolded mitochondrial protein response, mitophagy and mitochondrial fission associated with increased mitochondrial membrane potential and mitochondrial fission, indicating improved function(McCarron et al., 2013; Westermann, 2012).

Our transcriptomic analysis shows that Mmp14 is reduced during IF in the periosteum. In the suture mesenchyme, Piezo1, a gene known to mediate mechanically induced aging(Ren et al., 2022; Segel et al., 2019), was also significantly reduced in aged mice undergoing IF. Along with the reversal of nuclear cell morphology and levels of F-actin, these results indicate that IF also impacts the mechanics of the tissue, making it resemble that of younger animals. IF also upregulated Dbp, Tef, and Hlf, genes involved in the circadian transcriptional network (Gachon et al., 2004), in both osteoprogenitor compartments of aged mice. These genes, which act on D-box sites, are linked to premature aging when knocked out, affecting the liver, kidney (Gachon et al., 2006), and hematopoietic stem cell differentiation. While circadian rhythms' impact on bone is mostly studied in osteoblasts *in vitro*(Luo et al., 2021; Zhou et al., 2018), our data suggest that circadian transcription may play a role in rejuvenating $CD90^+$ cells for bone formation and repair in aged mice. ChIP-SEQ studies (Yoshitane et al., 2019) have identified D-box sites near promoters of Wnt/β-catenin components (e.g., Lrp5/6, Wnt8a, Fzd4) and osteogenic transcription factors like Zbtb16, linking circadian rhythms, stem cell function, and Wnt signaling (Lecarpentier et al., 2014; Matsu-Ura et al., 2018). While food intake regulates circadian rhythms in several organs (Damiola et al., 2000; Pickel and Sung, 2020), the diet-circadian interaction in bone repair is not well understood. Investigating circadian transcription's role in enhancing osteoprogenitor function for bone repair in aged mice is promising.

IF also led to beneficial shifts in gut microbiota composition, including elevated levels of *Akkermansia muciniphila* and increased expression of genes involved in NAD^+ biosynthesis. Subsequently, we show that short-term supplementation with *Akkermansia muciniphila* or NMN in aged mice significantly improve periosteal blood vessel density, osteoprogenitor number and function, osteoclast activity and enhance bone health and repair.

Although IF, Akk or NMN can act through many pathways and cellular processes, previous studies highlighted their beneficial effect on metabolism particularly their influence on NAD-dependent pathways. Mechanistically, our *in vitro* studies using calvarial osteogenic cells revealed that NMN protects against mitochondrial damage, often associated with aging, promotes healthy mitochondrial morphology and function, and enhances osteogenesis.

The effects of the three metabolic approaches on bone health and repair have not been studied in the context of already-aged individuals. NMN shows protective effects against bone health decline, but in long-term studies that begin dosing well before old age(Kim et al., 2021; Mills et al., 2016; Song et al., 2019). The impact of *Akkermansia muciniphila* on bone health or healing has only been investigated in young adult models with subcritical defects(Lawenius et al., 2020; Liu et al., 2020). IF diet has been investigated for skin wounding(Luo et al., 2020) in young animals but not for bone repair. We present key progress in developing three clinically relevant approaches for bone tissue regeneration in elderly patients. First, we describe the effects of NMN or *Akkermansia* dosing, or IF diet on bone tissues in aged animals that have already experienced severe skeletal decline. Second, our rejuvenation protocols are applied for shorter terms, and even post-injury with IF diet.

This study offers valuable insights into bone aging and rejuvenation strategies. However, future research should address several limitations. Further investigation is needed on the mechanisms of action of IF, NMN, and *Akkermansia*, optimal intervention timing and duration, and synergistic effects of combined approaches. While this study focused on a common osteoprogenitor, investigating the roles of specific skeletal stem cell populations and other cells within the osteogenic compartments (including immune cells) in flat bones represents a compelling frontier.

Our findings suggest broader implications beyond bone health, with these rejuvenation strategies potentially translating to other aging organs and injuries. Rigorous investigation of dosage, safety, and long-term effects will be essential for human applications.

Figure and Legends

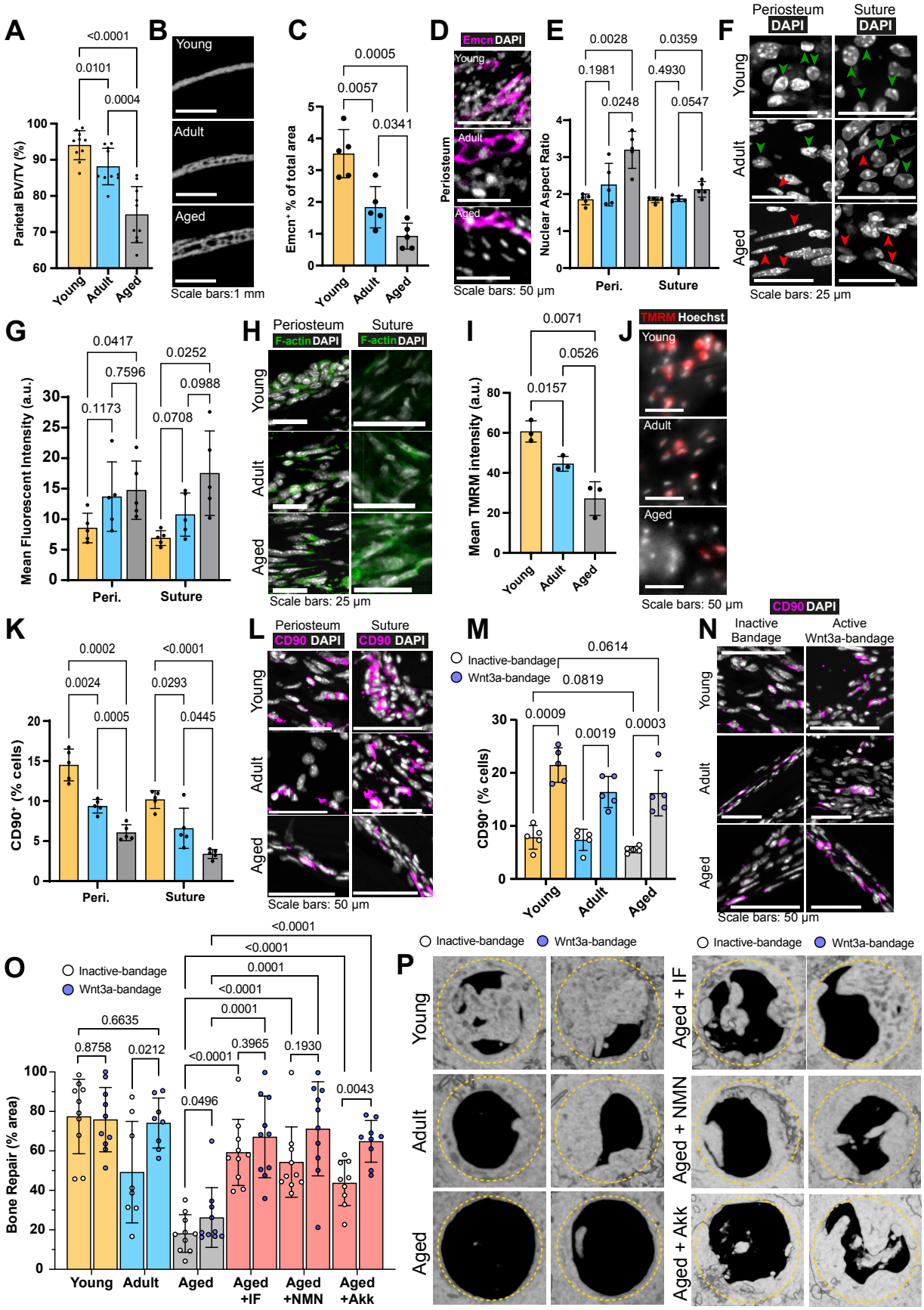

Figure 1 Changes to the calvarial bone, periosteum and suture mesenchyme, and bone repair with aging and interventions

(**A**) Parietal Bone Volume/Total Volume (BV/TV) and (**B**) representative transverse micro computed tomography (microCT) sections in Young, Adult, and Aged mice. Statistical analysis: Welch's test in n = 10 mice per condition. (**C**) Mean cross sectional area taken up by Endomucin (Emcn)-positive vascular cells and (**D**) representative immunofluorescence staining of Emcn (magenta) and DAPI (grey) in Young, Adult, and Aged mouse periosteum. Statistical analysis: Welch's tests in n = 5 mice per condition. (**E**) Nuclear aspect ratio (long axis divided by short axis) of cells within the periosteum and suture mesenchyme and (**F**) representative DAPI-stained nuclei in Young, Adult, and Aged mice. Statistical analysis: Welch's tests in n = 5 mice per condition. Green and red arrows highlight rounded and elongated nuclei, respectively. (**G**) Mean Phalloidin-488 fluorescence intensity and (**H**) representative images for filamentous actin (F-actin, green) and DAPI (grey) in Young, Adult, and Aged mouse periosteum and suture mesenchyme. Statistical analysis: Welch's tests in n = 5 mice per condition. (**I**) Mean intensity and (**J**) representative images of live TMRM staining (red) and Hoechst (grey) in Young, Adult, and Aged mouse periosteum *ex vivo*. Statistical analysis: Welch's tests in tissue from n = 3 mice per condition. (**K**) Percentage of $CD90^+$ cells within the periosteum and suture mesenchyme, expressed relative to the total cellular number ($DAPI^+$) in Young, Adult, and Aged mice. Representative images (**L**) show CD90 immunostaining (magenta) and DAPI (grey). Statistical analysis: Welch's tests in n = 5 mice per condition. (**M**) Percentage of $CD90^+$ cells within calvarial defects treated with Wnt3a-bandages (blue points) or inactive controls (white points), expressed relative to the total cellular number ($DAPI^+$) in Young, Adult, and Aged mice. (**N**) Representative images show CD90 immunostaining (magenta) and DAPI (grey). Statistical analysis: ratio-paired two-tailed t tests in n = 5 mice per condition. (**O**) Percentage of repair and (**P**) representative top-down microCT images within calvarial defects treated with Wnt3a-bandages (blue points) or inactive controls (white points). Statistical analysis within age groups: ratio-paired two-tailed t tests; between age groups and Aged mice following the IF protocol or NMN or Akk supplementation: Welch's tests; Young, Aged, Aged + IF, Aged + NMN, n = 10 mice; Aged + Akk, n = 9; Adult, n = 8. Complete statistical analysis between aged groups and treatments can be found in **Supplementary File 1**. The yellow dashed circle highlights the 2 mm diameter defect size.

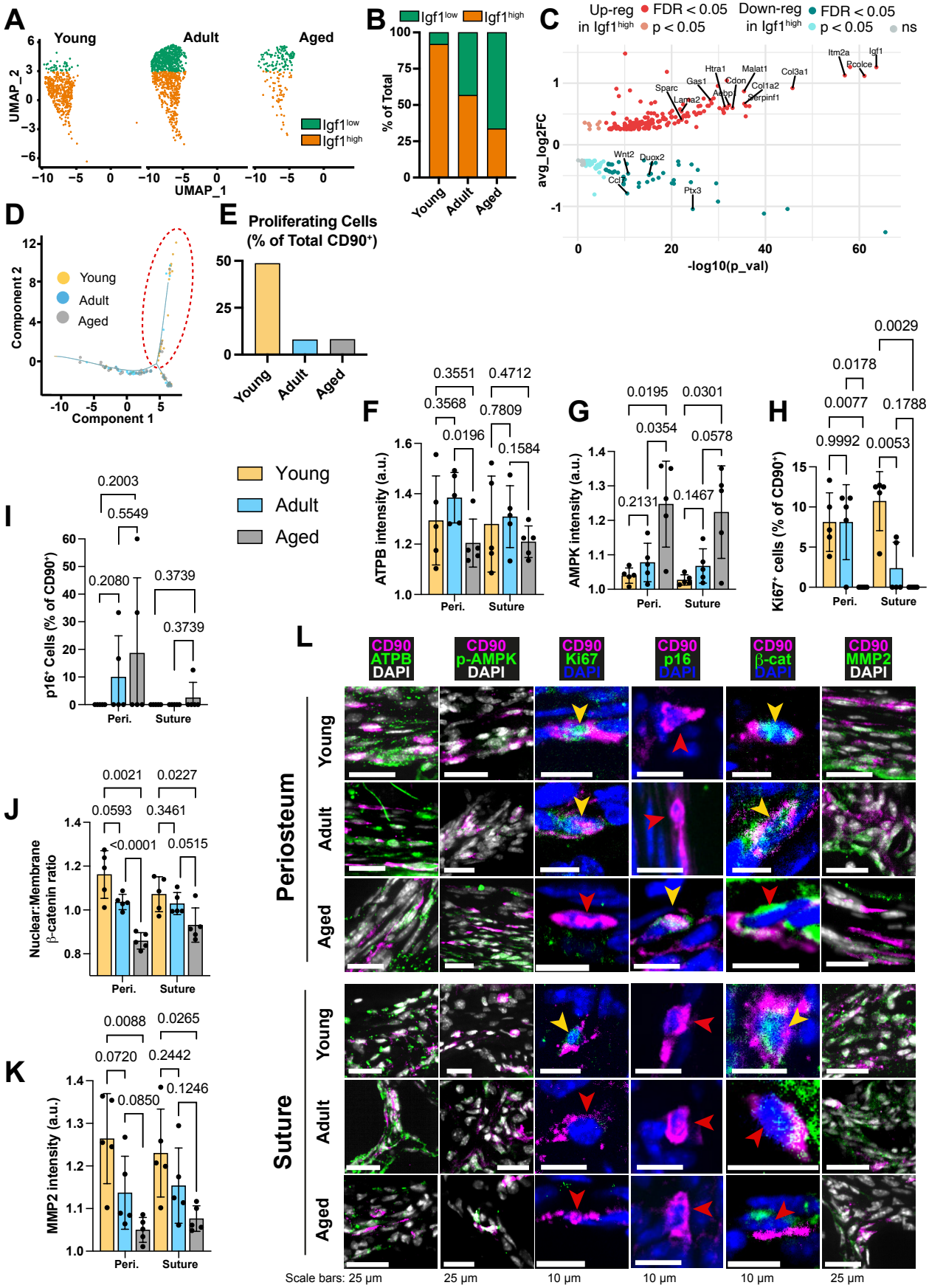
A
Young
Adult
Aged
UMAP_2
UMAP_1
Igf1low
Igf1high
B
Igf1low
Igf1high
% of Total
Young
Adult
Aged
C
Up-reg in Igf1high
FDR < 0.05
p < 0.05
Down-reg in Igf1high
FDR < 0.05
p < 0.05
ns
avg_log2FC
-log10(p_val)
Itm2a
Igf1
Bcolce
Htra1
Malat1
Col3a1
Gas1
Cdon
Sparc
Col1a2
Lama2
Serpinf1
Wnt2
Duox2
Ccl7
Ptx3
D
Young
Adult
Aged
Component 2
Component 1
E
Proliferating Cells
(% of Total CD90+)
Young
Adult
Aged
F
ATPB intensity (a.u.)
Peri.
Suture
0.3551
0.4712
0.3568
0.7809
0.0196
0.1584
G
AMPK intensity (a.u.)
Peri.
Suture
0.0195
0.0301
0.0354
0.0578
0.2131
0.1467
H
Ki67+ cells (% of CD90+)
Peri.
Suture
0.0029
0.0178
0.0077
0.1788
0.9992
0.0053
I
p16+ Cells (% of CD90+)
Peri.
Suture
0.2003
0.5549
0.2080
0.3739
0.3739
J
Nuclear:Membrane β-catenin ratio
Peri.
Suture
0.0021
0.0227
0.0593
0.3461
<0.0001
0.0515
K
MMP2 intensity (a.u.)
Peri.
Suture
0.0088
0.0265
0.0720
0.2442
0.0850
0.1246
Young
Adult
Aged
L
CD90 ATPB DAPI
CD90 p-AMPK DAPI
CD90 Ki67 DAPI
CD90 p16 DAPI
CD90 β-cat DAPI
CD90 MMP2 DAPI
Periosteum
Suture
Young
Adult
Aged
Scale bars: 25 μm
25 μm
10 μm
10 μm
10 μm
25 μm

650

Figure 2 Transcriptomic and protein expression characterization of CD90$^+$ cells during aging

(**A**) UMAP-plot showing the distribution of a subpopulation of CD90$^+$ periosteal cells with aging, categorized as Igf1^{high} (orange) and Igf1^{low} (green). (**B**) Percentage of the total CD90$^+$ subpopulation categorized as either Igf1^{high} or Igf1^{low}. Young: Igf1^{high} (n = 425 cells), Igf1^{low} (n = 37); Adult: Igf1^{high} (n = 553), Igf1^{low} (n = 421); Aged: Igf1^{high} (n = 61), Igf1^{low} (n = 120). (**C**) Volcano plot showing differentially-expressed genes in the comparison of all Igf1^{high} cells (n = 1039) against all Igf1^{low} cells (n = 578). Statistical analysis: Wilcoxon Rank Sum test via the FindMarkers function in the Seurat R package; upregulated (pink: $p < 0.05$; red: False discovery rate (FDR) -adjusted $p < 0.05$), downregulated (cyan: $p < 0.05$; teal: FDR-adjusted $p < 0.05$), and non-significant (ns) genes are displayed on axes of log fold expression (Igf1^{high} over Igf1^{low}) (y, avg_log2FC) against p transformed as its negative log value. (**D**) Dimensional reduction plot (Monocle package(Trapnell et al., 2014)) of suture mesenchyme CD90$^+$ populations in Young (yellow), Adult (blue), and Aged (grey) mice. (**E**) Percentage of CD90$^+$ categorized as 'proliferating' (inside red dashed ellipse) vs 'non-proliferating' (outside ellipse). Young: proliferating (n = 19 cells), nonproliferating (n = 20); Adult: proliferating (n = 5), non-proliferating (n = 57); Aged: proliferating (n = 5), nonproliferating (n = 56). (**F**) Normalized intensity staining for ATPB in CD90$^+$ cells. (**G**) Normalized intensity staining for phospho-AMPK in CD90$^+$ cells. (**H**) Proportion of CD90$^+$ cells that are Ki67$^+$. (**I**) Proportion of CD90$^+$ cells that are p16$^+$. (**J**) Ratio of Nuclear:Membrane β-catenin staining in CD90$^+$ cells. (**K**) Normalized intensity staining for MMP2 in CD90$^+$ cells. For all plots (**F**-**K**), Young (yellow), Adult (blue), Aged (grey), periosteum (3 left columns), suture mesenchyme (3 right columns), statistical testing: Welch's tests in n = 5 mice per condition. (**L**) Representative images depicting CD90 (magenta), DAPI (grey/blue as indicated by column), and functional markers (green) as indicated by column. Yellow arrows indicate marker-high/positive cells; red arrows indicate marker-low/negative cells.

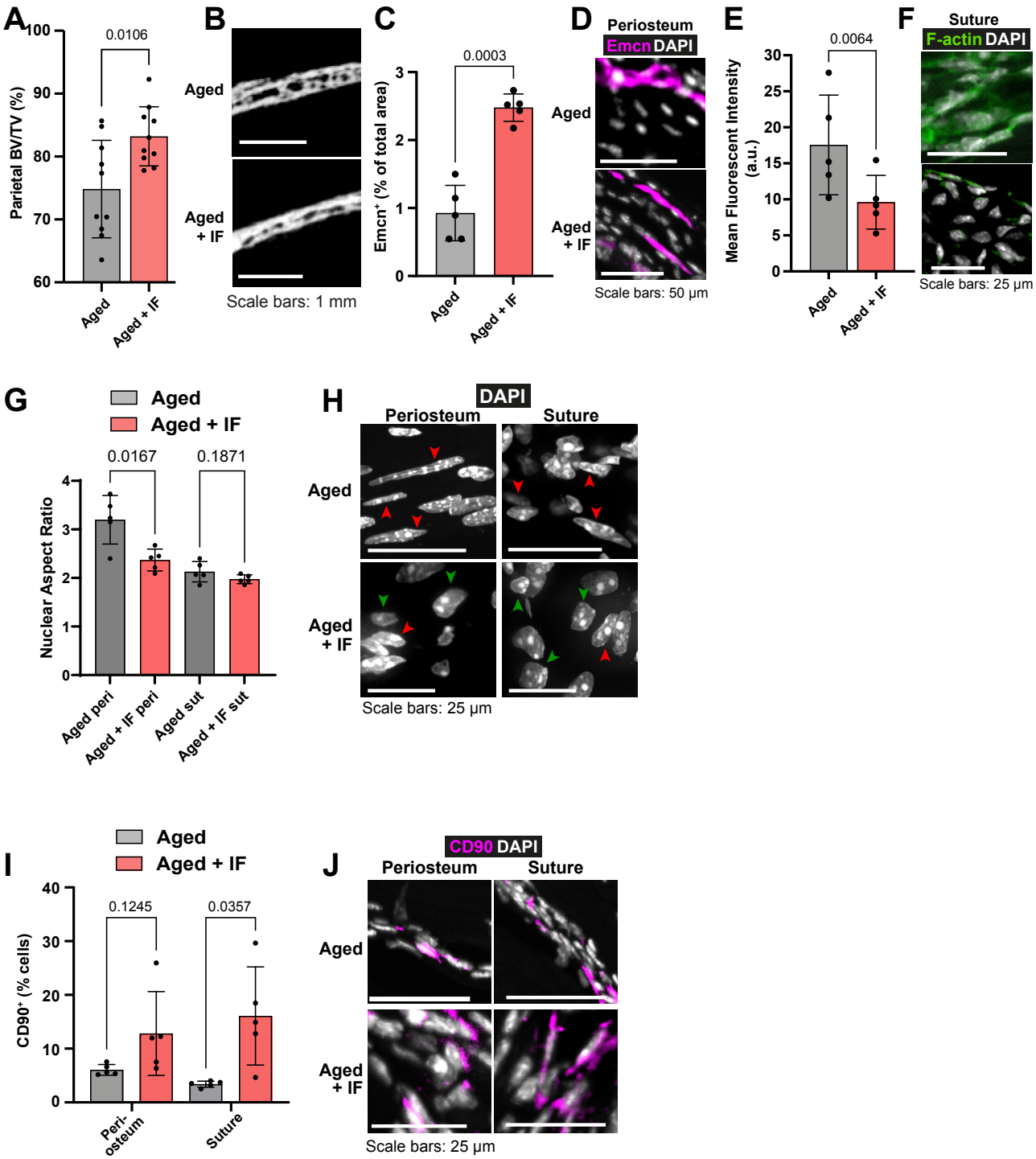
A
Parietal BV/TV (%)
0.0106
Aged
Aged + IF
B
Aged
Aged + IF
Scale bars: 1 mm
C
Emcn+ (% of total area)
0.0003
Aged
Aged + IF
D
Periosteum
Emcn DAPI
Aged
Aged + IF
Scale bars: 50 µm
E
Mean Fluorescent Intensity (a.u.)
0.0064
Aged
Aged + IF
F
Suture
F-actin DAPI
Scale bars: 25 µm
G
Aged
Aged + IF
Nuclear Aspect Ratio
0.0167
0.1871
Aged peri
Aged + IF peri
Aged sut
Aged + IF sut
H
DAPI
Periosteum
Suture
Aged
Aged + IF
Scale bars: 25 µm
I
Aged
Aged + IF
CD90+ (% cells)
0.1245
0.0357
Peri-osteum
Suture
J
CD90 DAPI
Periosteum
Suture
Aged
Aged + IF
Scale bars: 25 µm

674

675 **Figure 3 The impact of Intermittent Fasting on Aged bone structure and osteogenic tissues**
676 (**A**) Parietal Bone Volume/Total Volume (BV/TV) and (**B**) representative transverse micro computed
677 tomography (microCT) of Aged mice undergoing intermittent fasting. Statistical analysis: Welch's test in n =
678 10 mice per condition. (**C**) Mean cross sectional area taken up by Endomucin (Emcn)-positive vascular cells
679 and (**D**) representative immunofluorescence staining of Emcn (magenta) and DAPI (grey) in the periosteum
680 of Aged mice undergoing intermittent fasting. Statistical analysis: Welch's tests in n = 5 mice per condition.
681 (**E**) Mean Phalloidin-488 fluorescence intensity and (**F**) representative images for filamentous actin (F-actin,
682 green) and DAPI (grey) in the suture mesenchyme of Aged mice undergoing intermittent fasting. Statistical
683 analysis: Welch's test in n = 5 mice per condition. (**G**) Nuclear aspect ratio (long axis divided by short axis) of
684 cells within the periosteum and suture mesenchyme and representative DAPI-stained nuclei (**H**) of Aged mice
685 undergoing intermittent fasting. Statistical analysis: Welch's tests in n = 5 mice per condition. Green and red
686 arrows highlight rounded and elongated nuclei, respectively. (**I**) Percentage of $CD90^+$ cells within the
687 periosteum (left columns) and suture (right columns), expressed relative to the total cellular number ($DAPI^+$)
688 in Aged mice undergoing intermittent fasting. Representative images (**J**) show CD90 immunostaining
689 (magenta) and DAPI (grey). Statistical analysis: Welch's tests in n = 5 mice.
690 In panels **A**, **C**, **E**, **G and I,** columns in grey are data previously shown in **Fig. 1**, reproduced here for reference.
691 In panels **B**, **D**, **F**, **H**, **J**, Aged control representative images previously shown in **Fig. 1** are reproduced here
692 for reference.
693
694

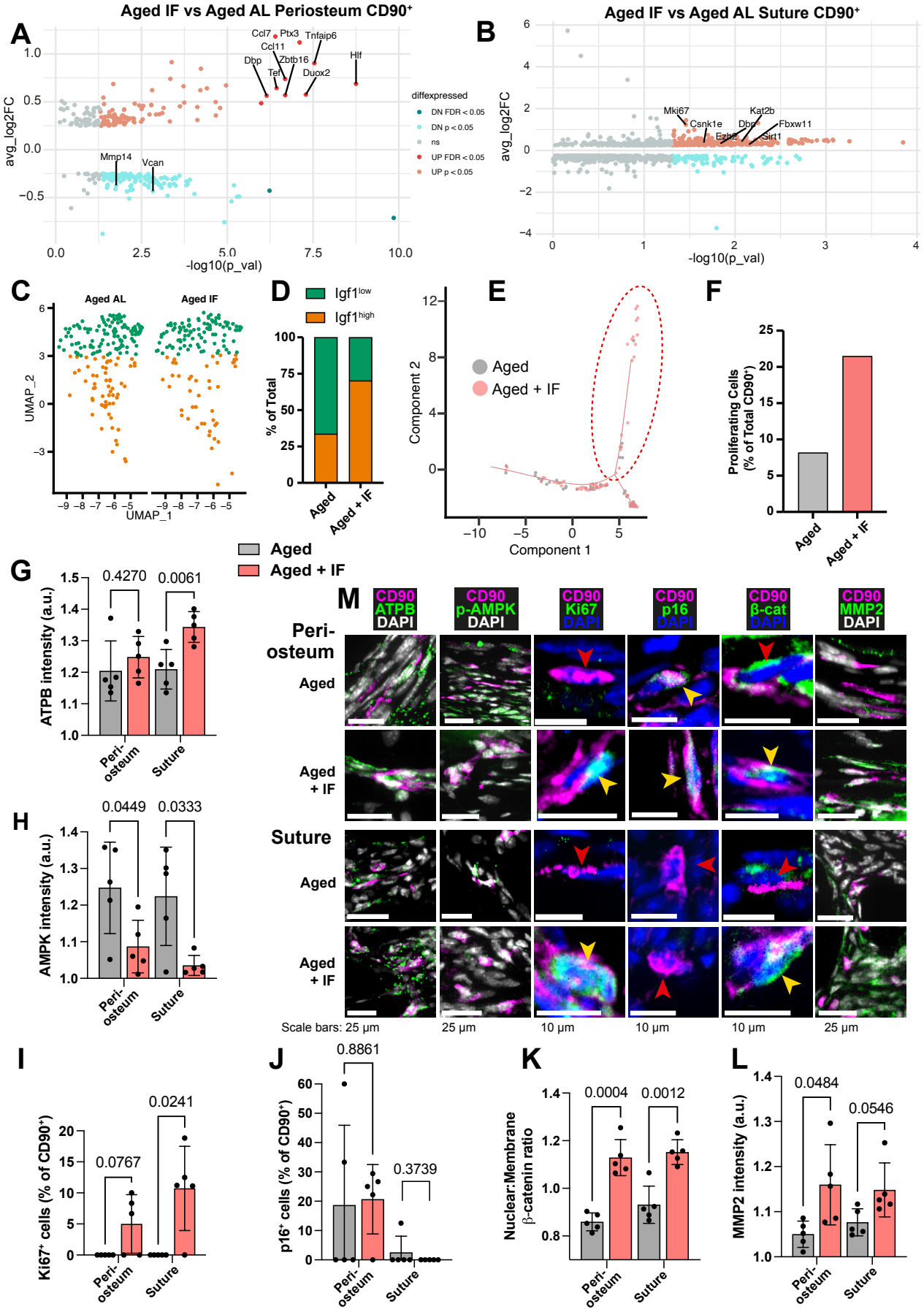
A
Aged IF vs Aged AL Periosteum CD90+
avg_log2FC
-log10(p_val)
Ccl7
Ptx3
Tnfaip6
Ccl11
Dbp
Zbtb16
Tef
Duox2
Hlf
Mmp14
Vcan
diffexpressed
DN FDR < 0.05
DN p < 0.05
ns
UP FDR < 0.05
UP p < 0.05
B
Aged IF vs Aged AL Suture CD90+
Mki67
Csnk1e
Ezh2
Dbp
Kat2b
Fbxw11
Sirt1
C
Aged AL
Aged IF
UMAP_2
UMAP_1
D
Igf1low
Igf1high
% of Total
Aged
Aged + IF
E
Aged
Aged + IF
Component 2
Component 1
F
Proliferating Cells (% of Total CD90+)
Aged
Aged + IF
G
ATPB intensity (a.u.)
0.4270
0.0061
Peri-osteum
Suture
H
AMPK intensity (a.u.)
0.0449
0.0333
Peri-osteum
Suture
M
CD90 ATPB DAPI
CD90 p-AMPK DAPI
CD90 Ki67 DAPI
CD90 p16 DAPI
CD90 β-cat DAPI
CD90 MMP2 DAPI
Peri-osteum
Aged
Aged + IF
Suture
Aged
Aged + IF
Scale bars: 25 μm
25 μm
10 μm
10 μm
10 μm
25 μm
I
Ki67+ cells (% of CD90+)
0.0767
0.0241
Peri-osteum
Suture
J
p16+ cells (% of CD90+)
0.8861
0.3739
Peri-osteum
Suture
K
Nuclear:Membrane β-catenin ratio
0.0004
0.0012
Peri-osteum
Suture
L
MMP2 intensity (a.u.)
0.0484
0.0546
Peri-osteum
Suture

695

Figure 4 Transcriptomic and protein expression characterization of Aged CD90$^+$ cells during intermittent fasting

(**A**) Volcano plot showing differentially-expressed genes in the comparison of the Aged CD90$^+$ population in the periosteum and (**B**) suture during intermittent fasting (IF) vs the *ad libitum* (AL) diet. Statistical analysis: Wilcoxon Rank Sum test via the FindMarkers function in the Seurat R package. Upregulated (pink: $p < 0.05$; red: FDR-adjusted $p < 0.05$), downregulated (cyan: $p < 0.05$; teal: FDR-adjusted $p < 0.05$), and nonsignificant (ns) genes are displayed on axes of log fold expression (IF over AL) (y, avg_log2FC) against p transformed as its negative log value. Periosteum: Aged IF (n = 194 cells); Aged AL (n = 242 cells). Suture: Aged IF (n = 79 cells); Aged AL (n = 61 cells). (**C**) UMAP-plot showing the distribution of a subpopulation of CD90$^+$ periosteal cells during intermittent fasting in Adult and Aged mice. AL cells are data previously shown, reproduced here for reference. (**D**) Percentage of the total cells categorized as either Igf1^{high} or Igf1^{low}. Aged + IF: Igf1^{high} (n = 104), Igf1^{low} (n = 44). (**E**) Plot (Monocle package) of suture CD90$^+$ populations. (**F**) Percentage of CD90$^+$ categorized as 'proliferating' (inside red dashed ellipse) vs 'non-proliferating' (outside ellipse) in Aged mice undergoing intermittent fasting. AL cells and chart are data previously shown, reproduced here for reference. Statistical analysis: two-tailed binomial test based on expected observed proportions between groups. Adult + IF: proliferating (n = 30 cells), non-proliferating (n = 86); Aged + IF: proliferating (n = 17), non-proliferating (n = 62). (**G**) Normalized intensity staining for ATPB in CD90$^+$ cells. (**H**) Normalized intensity staining for phospho-AMPK in CD90$^+$ cells. (**I**) Proportion of CD90$^+$ cells that are Ki67$^+$. (**J**) Proportion of CD90$^+$ cells that are p16$^+$. (**K**) Ratio of Nuclear:Membrane β-catenin staining in CD90$^+$ cells. (**L**) Normalized intensity staining for MMP2 in CD90$^+$ cells. For all plots (**G**-**L**), Aged + IF (red), Aged control (grey), periosteum (2 left columns), suture mesenchyme (2 right columns), statistical testing: Welch's tests in n = 5 mice per condition. (**M**) Representative images depicting CD90 (magenta), DAPI (grey/blue as indicated by column), and functional markers (green) as indicated by column). Yellow arrows indicate marker-high/positive cells; red arrows indicate marker-low/negative cells. In panels **C**-**M,** data and representative images of Aged controls from previous figures are reproduced here for reference.

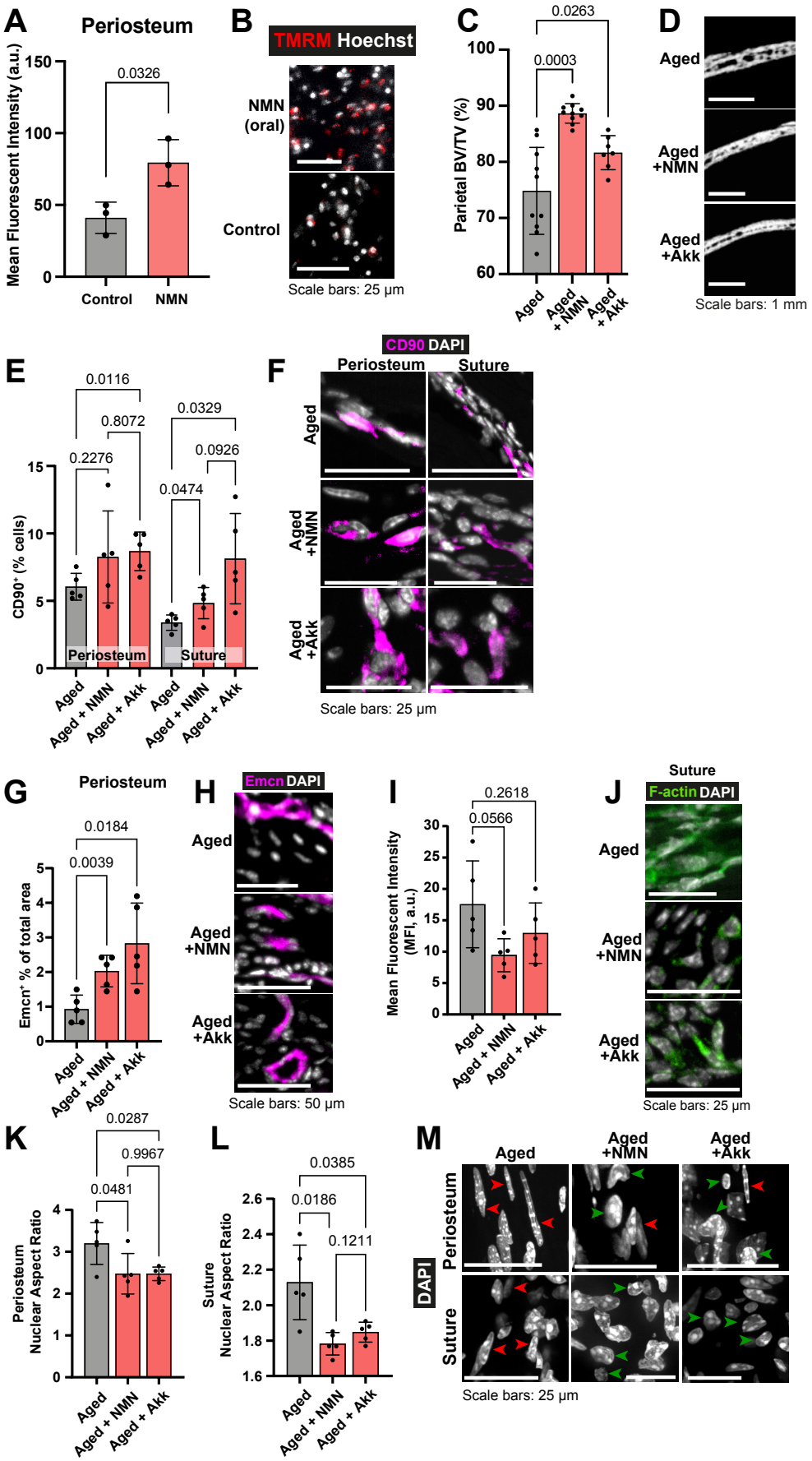
A
Periosteum
Mean Fluorescent Intensity (a.u.)
0.0326
Control
NMN
B
TMRM Hoechst
NMN (oral)
Control
Scale bars: 25 µm
C
0.0263
0.0003
Parietal BV/TV (%)
Aged
Aged + NMN
Aged + Akk
D
Aged
Aged +NMN
Aged +Akk
Scale bars: 1 mm
E
0.0116
0.8072
0.2276
0.0329
0.0926
0.0474
CD90+ (% cells)
Periosteum
Suture
Aged
Aged + NMN
Aged + Akk
F
CD90 DAPI
Periosteum
Suture
Aged
Aged +NMN
Aged +Akk
Scale bars: 25 µm
G
Periosteum
0.0184
0.0039
Emcn+ % of total area
Aged
Aged + NMN
Aged + Akk
H
Emcn DAPI
Aged
Aged +NMN
Aged +Akk
Scale bars: 50 µm
I
0.2618
0.0566
Mean Fluorescent Intensity (MFI, a.u.)
Aged
Aged + NMN
Aged + Akk
J
Suture
F-actin DAPI
Aged
Aged +NMN
Aged +Akk
Scale bars: 25 µm
K
0.0287
0.9967
0.0481
Periosteum Nuclear Aspect Ratio
Aged
Aged + NMN
Aged + Akk
L
0.0385
0.0186
0.1211
Suture Nuclear Aspect Ratio
Aged
Aged + NMN
Aged + Akk
M
Aged
Aged +NMN
Aged +Akk
Periosteum
Suture
DAPI
Scale bars: 25 µm
N
0.2392
Akkermansia Abundance (%)
Aged
Aged + IF

723

724 **Figure 5 The impact of Nicotinamide mononucleotide (NMN) and *Akkermansia muciniphila* (Akk)**
725 **supplementation on Aged bone structure and osteogenic tissues**
726 (**A**) Mean intensity and (**B**) representative images of live TMRM staining (red) and Hoechst (grey) in Adult
727 mice controls and Adult mice dosed with 600 mg/kg NMN by oral gavage, samples of periosteum *ex vivo*.
728 Statistical analysis: Welch's test in tissue from n = 3 mice per condition. (**C**) Parietal Bone Volume/Total
729 Volume (BV/TV) and (**D**) representative transverse micro-computed tomography (microCT) sections in Aged
730 mice supplemented with NMN or *Akkermansia*. Statistical analysis: Welch's tests in n = 10 (Aged, Aged +
731 NMN) and n = 7 (Aged + Akk) mice. (**E**) Percentage of $CD90^+$ cells within the periosteum (left columns) and
732 suture (right columns), expressed relative to the total cellular number ($DAPI^+$) in Aged mice supplemented
733 with NMN or *Akkermansia*. Representative images (**F**) show CD90 immunostaining (magenta) and DAPI
734 (grey). Statistical analysis: Welch's tests in n = 5 mice per condition. (**G**) Mean cross sectional area taken up
735 by Endomucin (Emcn)-positive vascular cells and (**H**) representative immunofluorescence staining of Emcn
736 (magenta) and DAPI (grey) in the periosteum of Aged mice supplemented with NMN or *Akkermansia*.
737 Statistical analysis: Welch's tests in n = 5 mice per condition. (**I**) Mean Phalloidin-488 fluorescence intensity
738 and (**J**) representative images for filamentous actin (F-actin, green) and DAPI (grey) in the suture
739 mesenchyme of Aged mice supplemented with NMN or *Akkermansia*. Statistical analysis: Welch's tests in n
740 = 5 mice per condition. (**K-M**) nuclear aspect ratio (long axis divided by short axis) of cells within the (**K**)
741 periosteum and (**L**) suture in Aged mice supplemented with NMN or *Akkermansia*, and (**M**) Representative
742 DAPI-stained nuclei. Statistical analysis: Welch's tests in n = 5 mice per condition. Green and red arrows
743 highlight rounded and elongated nuclei, respectively. (**N**) The relative abundance of bacteria identified as
744 genus *Akkermansia* in 16S metagenomic profiling of Aged mice undergoing intermittent fasting vs. Aged
745 controls. Statistical analysis: Welch's test in (Aged, n = 3; Aged + IF, n = 4) mice per condition. In panels **C-**
746 **M**, data and representative images of Aged controls from previous figures are reproduced here for reference.
747
748

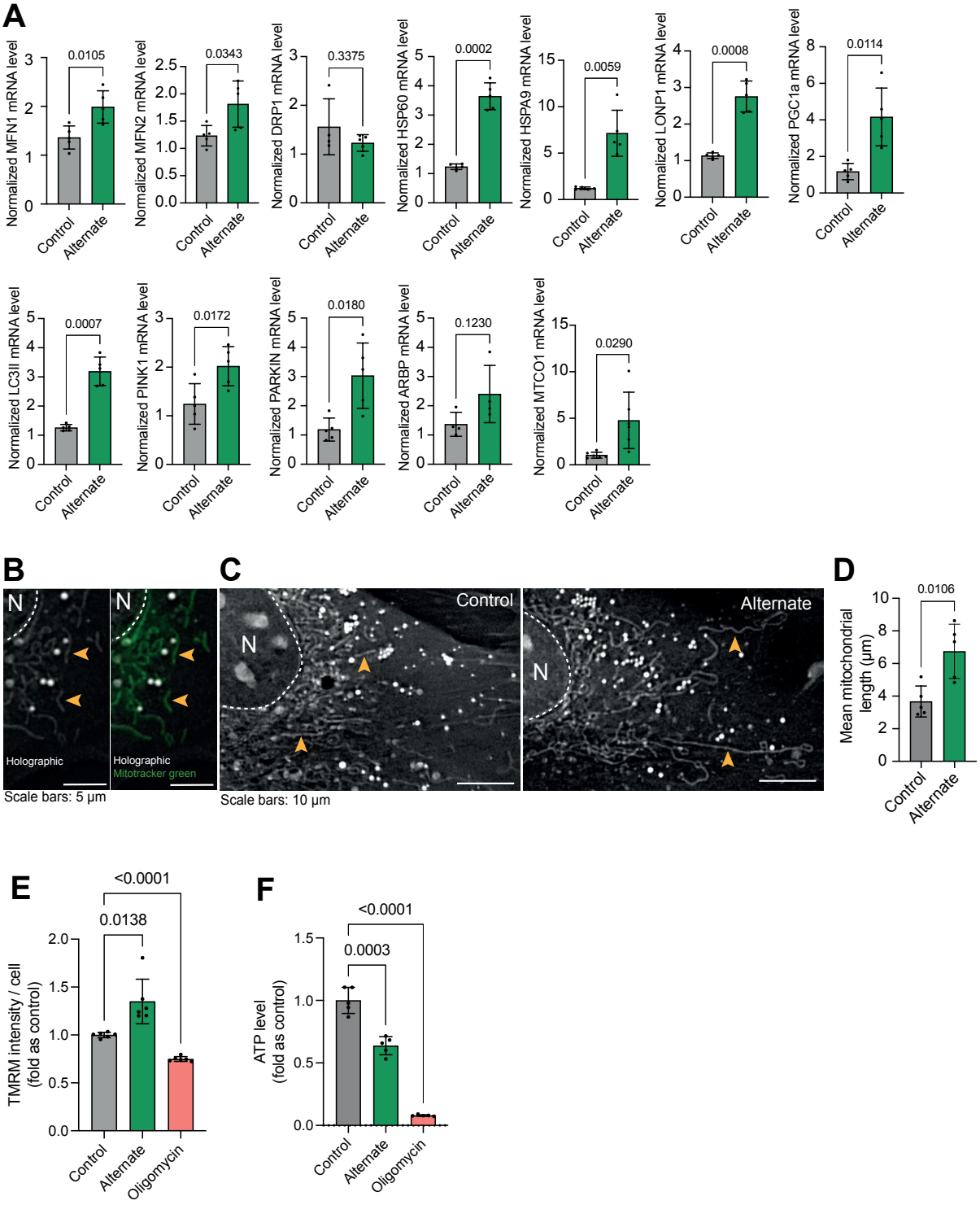
A
Normalized MFN1 mRNA level
0.0105
Normalized MFN2 mRNA level
0.0343
Normalized DRP1 mRNA level
0.3375
Normalized HSP60 mRNA level
0.0002
Normalized HSPA9 mRNA level
0.0059
Normalized LONP1 mRNA level
0.0008
Normalized PGC1a mRNA level
0.0114
Normalized LC3II mRNA level
0.0007
Normalized PINK1 mRNA level
0.0172
Normalized PARKIN mRNA level
0.0180
Normalized ARBP mRNA level
0.1230
Normalized MTCO1 mRNA level
0.0290
Control
Alternate
B
N
Holographic
Holographic
Mitotracker green
Scale bars: 5 µm
C
Control
Alternate
N
Scale bars: 10 µm
D
Mean mitochondrial length (µm)
0.0106
Control
Alternate
E
TMRM intensity / cell (fold as control)
<0.0001
0.0138
Control
Alternate
Oligomycin
F
ATP level (fold as control)
<0.0001
0.0003
Control
Alternate
Oligomycin

749

750 **Figure 6 Effect of hour-based alternate serum deprivation on mitochondria in MC3T3 cells in glucose-**
751 **free media.**
752 (**A**) Effect of alternate serum deprivation on gene expression involved in mitochondrial dynamics (MFN1,
753 MFN2, DRP1), unfolded protein response (mtUPR) (HSP60, HSPA9, LonP1), biogenesis (PGC1a), structure
754 (ARBP), mitophagy (LC3II, PINK1, PARKIN), and mitochondrial respiratory complex IV (MTCO1). Statistical
755 analysis: Welch's test, n≥4/group. (**B**) Representative holographic images of mitochondrial shape (orange
756 arrowheads), confirmed by Mitotracker green staining. (**C-D**) Effect of alternate serum deprivation on
757 mitochondrial length. Statistical analysis: Welch's t-test of n=5/group, total mitochondria=425. (**E**) Effect of
758 alternate serum deprivation and oligomycin on mitochondrial membrane potential. Statistical analysis: Welch's
759 t-test of n=6/group with at least 481 cells/group. (**F**) Effect of alternate serum deprivation and oligomycin on
760 ATP level. Statistical analysis: Welch's t-test of n≥5/group.
761

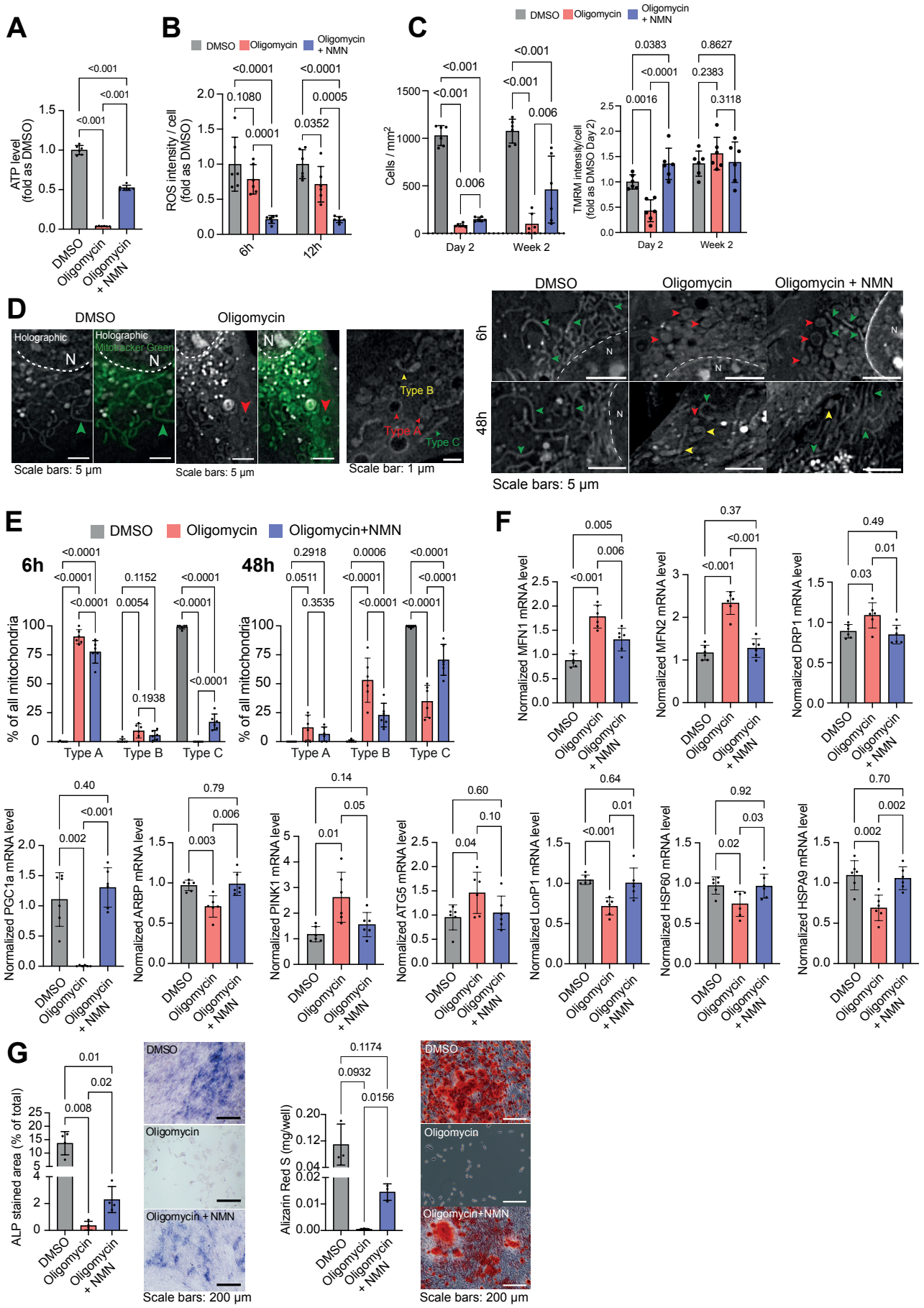
A
ATP level (fold as DMSO)
DMSO
Oligomycin
Oligomycin + NMN
B
ROS intensity / cell (fold as DMSO)
6h
12h
C
Cells / mm²
Day 2
Week 2
TMRM intensity/cell (fold as DMSO Day 2)
D
Holographic
Mitotracker Green
Type A
Type B
Type C
Scale bars: 5 µm
Scale bar: 1 µm
E
% of all mitochondria
6h
48h
F
Normalized MFN1 mRNA level
Normalized MFN2 mRNA level
Normalized DRP1 mRNA level
Normalized PGC1a mRNA level
Normalized ARBP mRNA level
Normalized PINK1 mRNA level
Normalized ATG5 mRNA level
Normalized LonP1 mRNA level
Normalized HSP60 mRNA level
Normalized HSPA9 mRNA level
G
ALP stained area (% of total)
Alizarin Red S (mg/well)
Scale bars: 200 µm

762

763 **Figure 7 Effect of NMN on oligomycin-induced mitochondrial damage in glucose-free MC3T3 cells.**
764 (**A**) Effect of oligomycin ± NMN on ATP level in MC3T3 cells. Welch's test, n=6/group. (**B**) Effect of oligomycin
765 ± NMN on ROS level MC3T3 cells. Welch's test, n=6/group. (**C**) Effect of oligomycin ± NMN on cell density
766 (left) and mitochondrial membrane potential (right) over time in MC3T3. Welch's test, n=6/group. (**D**)
767 Representative images of mitochondrial shape alteration by oligomycin exposure ± NMN supplementation.
768 Dashed white line = nuclear membrane, N = nucleus. Observation by holotomography (grey levels) and
769 confirmed with Mitotracker Green (green). Red arrowheads = Type A ("round"), yellow arrowheads = Type B
770 ("intermediate"), and green arrowheads = Type C ("rod-like/filamentous") mitochondria. (**E**) Quantification of
771 the effect of oligomycin ± NMN on mitochondrial shape. Each data point is a cell with at least 30 mitochondria.
772 Welch's test n = 6 cells / group, total mitochondria=1821. (**F**) Effect of oligomycin ± NMN on gene expression
773 involved in mitochondrial dynamics (MFN1, MFN2, DRP1), biogenesis (PGC1a), structure (ARBP), mitophagy
774 (PINK1, ATG5), and unfolded protein response (mtUPR) (LonP1, HSP60, HSPA9). Welch's test, n≥5/group.
775 (**G**) Effect of oligomycin ± NMN on osteoblastic differentiation. Staining of alkaline phosphatase (ALP) activity
776 and mineralization (Alizarin Red S; ARS) of the matrix after two weeks of differentiation. Welch's test, n=4
777 (ALP) or 3 (ARS) / group.
778

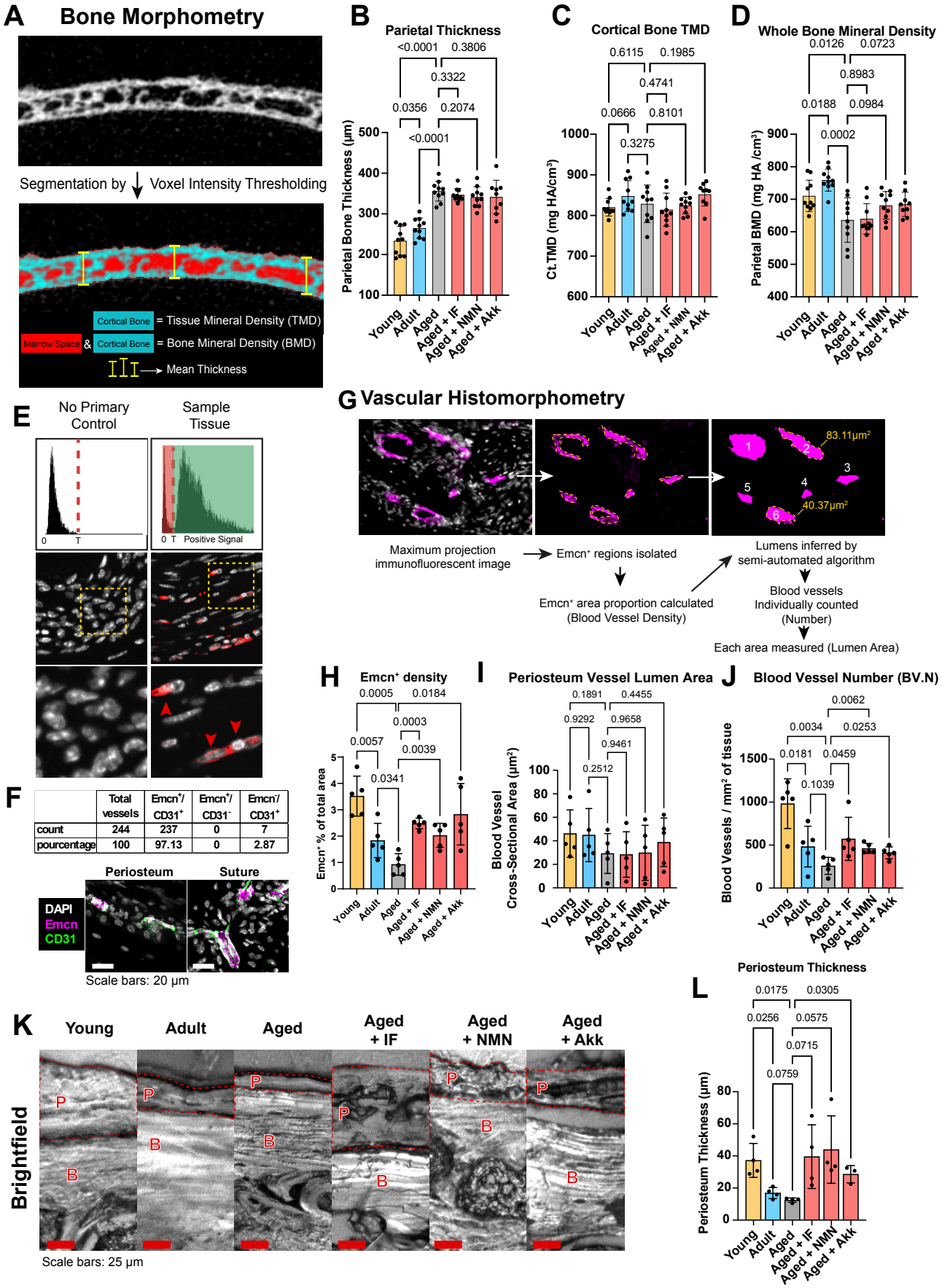

	Total vessels	Emcn⁺/ CD31⁺	Emcn⁺/ CD31⁻	Emcn⁻/ CD31⁺
count	244	237	0	7
pourcentage	100	97.13	0	2.87

780 **Figure 1 – figure supplement 1**
781 (**A**) Methodology for segmentation of micro-computed tomography (microCT) images for calculation of bone
782 morphometry metrics: (**B)** Parietal Thickness (**C**) Cortical Tissue Mineral Density (Ct.TMD), (**D**) Parietal Whole
783 Bone Mineral Density (BMD). Statistical analysis: Welch's tests, n = 10 mice per condition, except Aged + Akk
784 (n = 9). (**E**) The method for quantifying immunofluorescence-positive (red) cells. The maximum pixel intensity
785 is determined in control tissues lacking primary antibody (no primary control). This value is used to threshold
786 the stained sample tissue, with the remaining signal distinguishing positive cells (red arrows). DAPI (grey) is
787 also shown for reference of cellular locations. (**F**) Number and percentage of blood vessels positive for Emcn
788 and/or CD31 with representative images in the periosteum and suture mesenchyme. (**G**) Methodology for
789 segmentation of Endomucin (Emcn) immunofluorescent staining in fixed tissue sections, for calculation of
790 vascular histomorphometry metrics: (**H**) $Emcn^+$ staining density (proportion of total tissue area). Data are
791 shown previously in main Figures 1, 3, and 5, and are reproduced here for reference, (**I**) Mean lumen area
792 per blood vessel, (**J**) Number of blood vessels per area tissue (BV.N). Statistical analysis: Welch's tests, n =
793 5 mice per condition. (**K**) Representative brightfield images of unstained tissue sections highlighting the
794 overlying periosteum (red P, red dashed line) and parietal bone (red B). (**L**) Mean periosteal thickness.
795 Statistical analysis: Welch's tests, n = 4 mice per condition, except Aged + Akk (n = 3).
796

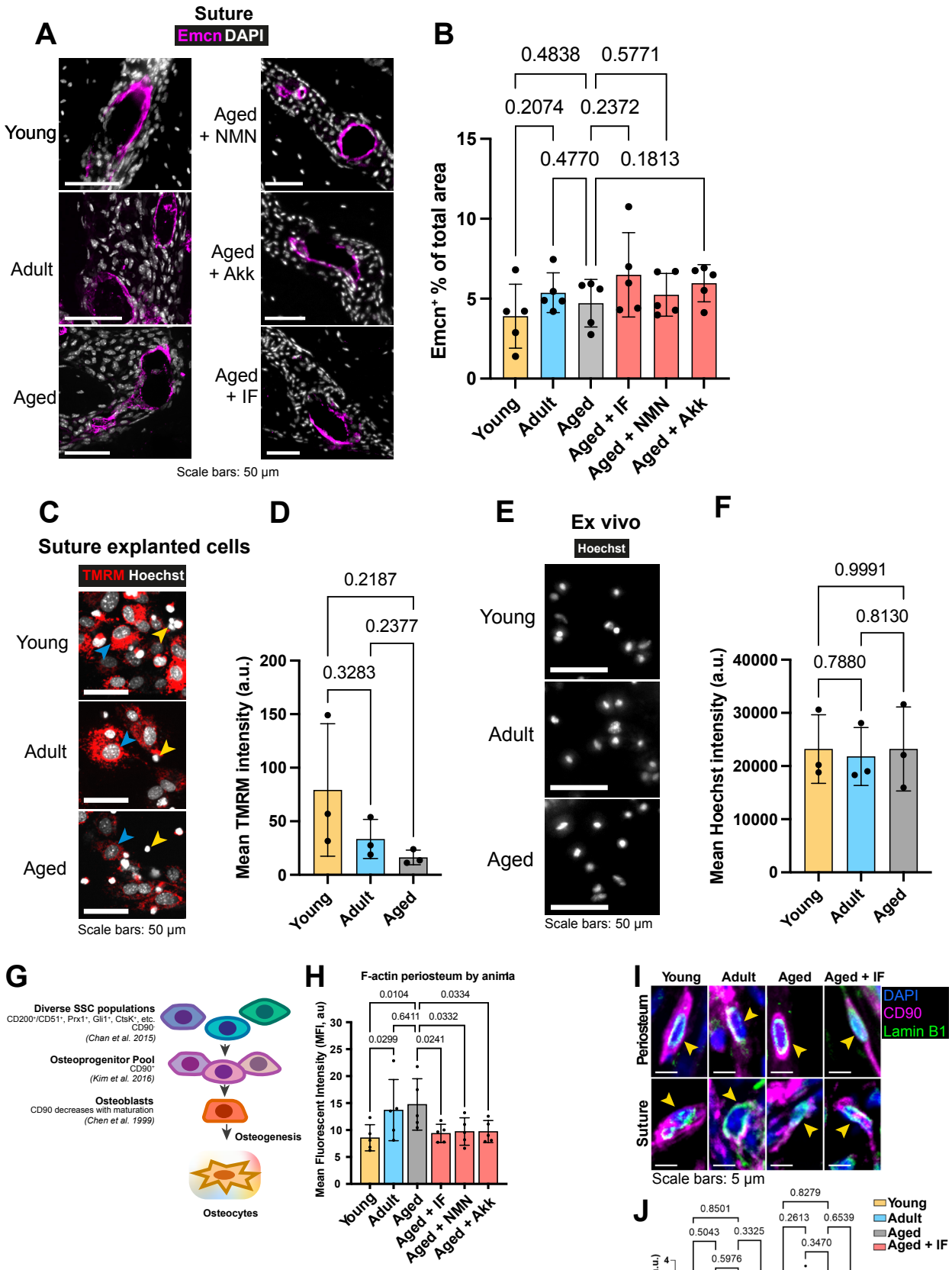
A
Suture
Emcn DAPI
Young
Adult
Aged
Aged + NMN
Aged + Akk
Aged + IF
Scale bars: 50 µm
B
Emcn+ % of total area
0.4838
0.5771
0.2074
0.2372
0.4770
0.1813
Young
Adult
Aged
Aged + IF
Aged + NMN
Aged + Akk
C
Suture explanted cells
TMRM Hoechst
Young
Adult
Aged
Scale bars: 50 µm
D
Mean TMRM intensity (a.u.)
0.2187
0.2377
0.3283
Young
Adult
Aged
E
Ex vivo
Hoechst
Young
Adult
Aged
Scale bars: 50 µm
F
Mean Hoechst intensity (a.u.)
0.9991
0.8130
0.7880
Young
Adult
Aged
G
Diverse SSC populations
CD200+/CD51+, Prx1+, Gli1+, CtsK+, etc.
CD90-
(Chan et al. 2015)
Osteoprogenitor Pool
CD90+
(Kim et al. 2016)
Osteoblasts
CD90 decreases with maturation
(Chen et al. 1999)
Osteogenesis
Osteocytes
H
F-actin periosteum by animal
Mean Fluorescent Intensity (MFI, au)
0.0104
0.0334
0.6411
0.0332
0.0299
0.0241
Young
Adult
Aged
Aged + IF
Aged + NMN
Aged + Akk
I
Young
Adult
Aged
Aged + IF
Periosteum
Suture
DAPI
CD90
Lamin B1
Scale bars: 5 µm
J
Lamin B1 intensity (a.u.)
0.8501
0.5043
0.3325
0.5976
0.8279
0.2613
0.6539
0.3470
Periosteum
Suture
Young
Adult
Aged
Aged + IF

797

798 **Figure 1 – figure supplement 2**

799 (**A**) representative immunofluorescence staining of Emcn (magenta) and DAPI (grey) and (**B**) mean cross
800 sectional area of Endomucin (Emcn)-positive vascular cells in mouse sutures. Statistical analysis: Welch's
801 tests in n = 5 mice. (**C**) Representative images and (**D**) mean intensity of live TMRM staining (red) and Hoechst
802 (grey) in adherent cells allowed to explant from suture mesenchyme tissue for 24 hours *in vitro*. Remaining
803 mesenchyme tissue was removed prior to staining. Statistical analysis: Welch's tests in tissue from n = 3 mice
804 per condition. (**E**) Representative images and (**F**) mean intensity of live Hoechst staining (grey) from the TMRM
805 experiment in **Fig. 1i-j**. Statistical analysis: Welch's tests in tissue from n = 3 mice per condition. (**G**) Schematic
806 demonstrating the hierarchy and selected markers of Skeletal Stem Cells (SSCs), leading to the $CD90^+$ cell
807 pool, which ultimately differentiates into osteoblasts and osteocytes during osteogenesis. (**H**) Mean Phalloidin-
808 488 staining intensity for F-actin in the periosteum. Statistical analysis: Welch's tests in n = 5 mice. (**I**)
809 Representative images depicting CD90 (magenta), DAPI (blue), and Lamin B1 (green). Yellow arrows indicate
810 positive cells. (**J**) Normalized intensity staining for Lamin B1 in the nucleus of $CD90^+$ cells. Statistical analysis:
811 Welch's tests in n = 5 mice per condition.
812

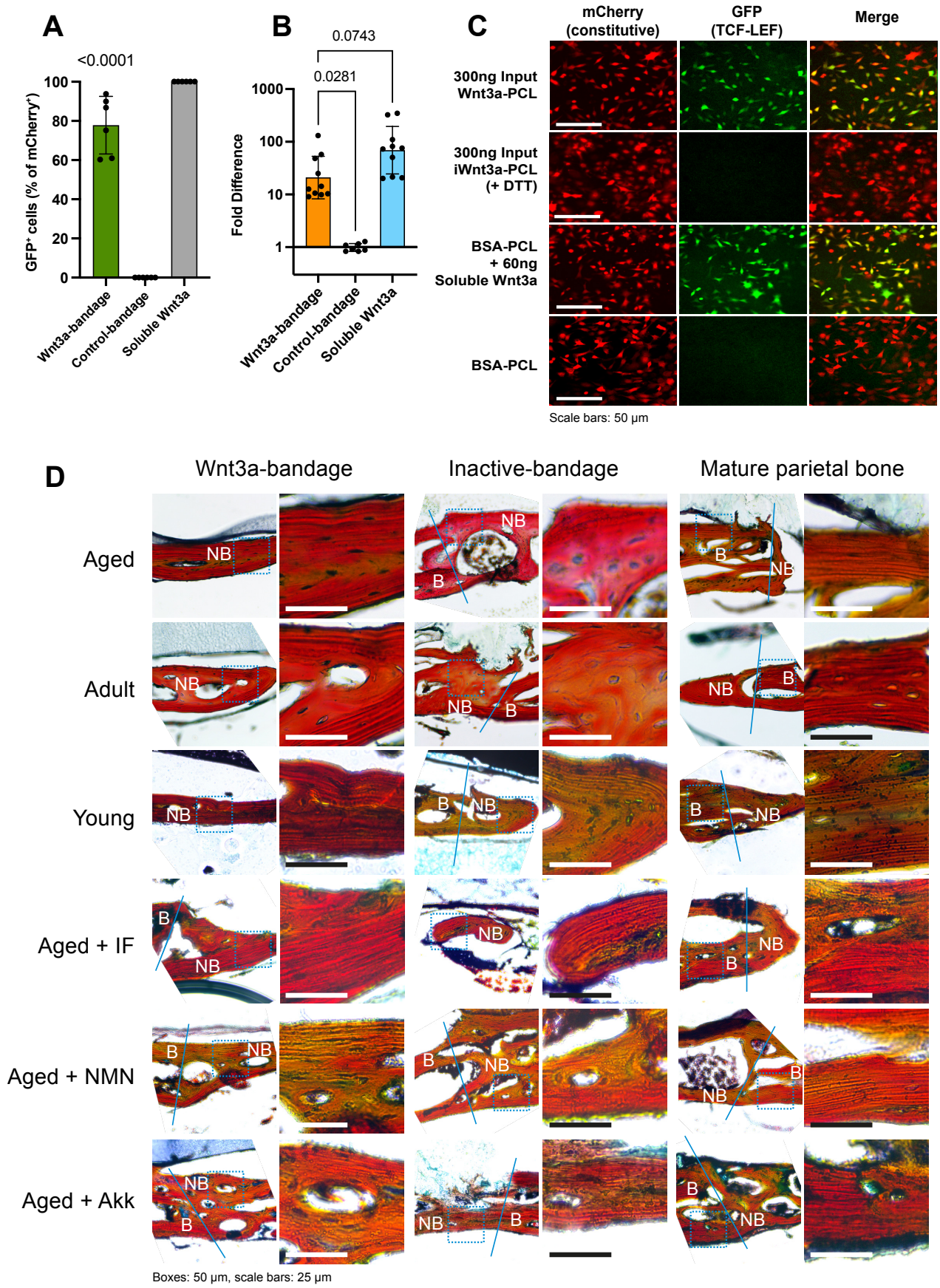
A
<0.0001
GFP+ cells (% of mCherry+)
100
80
60
40
20
0
Wnt3a-bandage
Control-bandage
Soluble Wnt3a
B
0.0743
0.0281
Fold Difference
1000
100
10
1
Wnt3a-bandage
Control-bandage
Soluble Wnt3a
C
mCherry (constitutive)
GFP (TCF-LEF)
Merge
300ng Input Wnt3a-PCL
300ng Input iWnt3a-PCL (+ DTT)
BSA-PCL + 60ng Soluble Wnt3a
BSA-PCL
Scale bars: 50 µm
D
Wnt3a-bandage
Inactive-bandage
Mature parietal bone
Aged
Adult
Young
Aged + IF
Aged + NMN
Aged + Akk
NB
B
Boxes: 50 µm, scale bars: 25 µm

813

814 **Figure 1 – figure supplement 3**
815 (**A**) Characterization of Wnt3a-bandage activation of the Wnt/β-catenin pathway with Comma-D Beta cells *in*
816 *vitro*. Presented as the proportion of GFP^+ cells, normalized to the proportion of GFP^+ responsive to soluble
817 Wnt3a. Statistical analysis: two-tailed one-sample t test against the inactive control-bandage (mean = 0); n =
818 6 for each condition. (**B**) Characterization of Wnt3a-bandage activation of the Wnt/β-catenin pathway with
819 LS/L cells *in vitro*. Presented as fold change of Luciferase signal over control-bandage. Statistical analysis:
820 Welch's test, n = 10 for each Wnt3a-bandage and Soluble Wnt3a, n = 7 for Control-bandage.
821 (**C**) Representative images for Comma-D Beta cells quantified in (**A**). mCherry (red) is constitutively
822 expressed, GFP (green) is expressed during Wnt/β-catenin pathway activation. Wnt3a is treated with DTT,
823 resulting in complete chemical inactivation (iWnt3a). Bovine Serum Albumin (BSA) is used as an additional
824 negative control. Polycaprolactone (PCL) is the polymeric material that Wnt3a is bound to during
825 Wnt3abandage manufacture. (**D**) Representative Movat's pentachrome staining of bone tissues showing the
826 lamellar/striated structures. Blue line designates the drilled defect edge, thereby separating original intact
827 bone B from new bone NB. The dashed blue box shows the enlarged region.
828

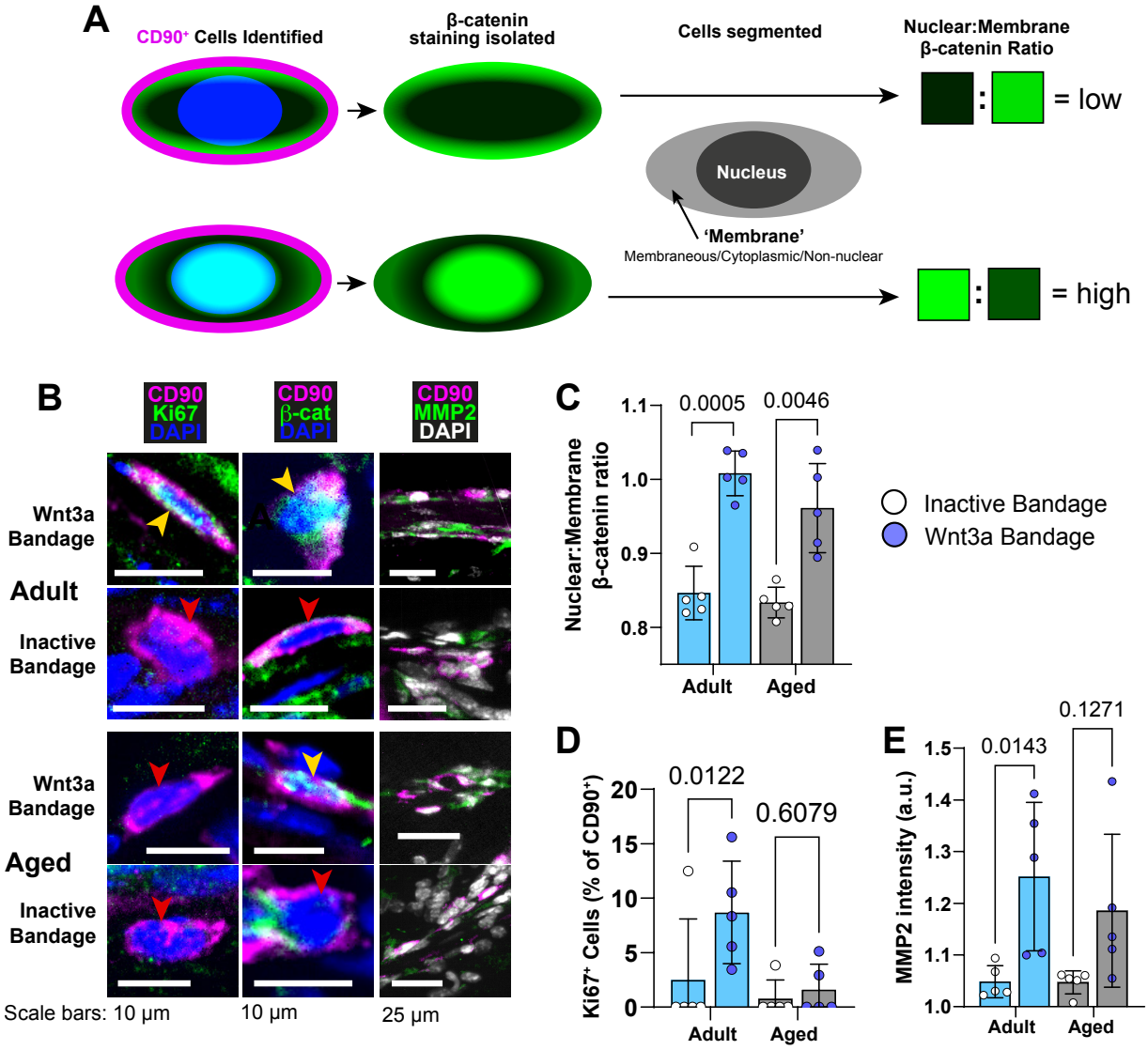
A
CD90+ Cells Identified
β-catenin staining isolated
Cells segmented
Nuclear:Membrane β-catenin Ratio
= low
Nucleus
'Membrane'
Membraneous/Cytoplasmic/Non-nuclear
= high
B
CD90 Ki67 DAPI
CD90 β-cat DAPI
CD90 MMP2 DAPI
Wnt3a Bandage
Adult
Inactive Bandage
Wnt3a Bandage
Aged
Inactive Bandage
Scale bars: 10 μm
10 μm
25 μm
C
Nuclear:Membrane β-catenin ratio
0.0005
0.0046
Adult
Aged
Inactive Bandage
Wnt3a Bandage
D
Ki67+ Cells (% of CD90+)
0.0122
0.6079
Adult
Aged
E
MMP2 intensity (a.u.)
0.0143
0.1271
Adult
Aged

829

830 **Figure 1 – figure supplement 4**

831 (**A**) Schematic depicting the methodology for measuring the ratio of Nuclear:Membrane β-catenin in single
832 $CD90^+$ cells. (**B**) Representative images depicting CD90 (magenta), DAPI (grey/blue as indicated by column),
833 and functional markers (green) as indicated by column). Yellow arrows indicate marker-high/positive cells; red
834 arrows indicate marker-low/negative cells. (**C**) Proportion of $CD90^+$ cells that are $Ki67^+$ by age. Statistical
835 testing: paired, two-tailed t tests in n = 5 mice per condition. (**D**) Ratio of Nuclear:Membrane β-catenin staining
836 in $CD90^+$ cells by age. Statistical testing: ratio paired, two-tailed t tests in n = 5 mice per condition. (**E**)
837 Normalized intensity staining for MMP2 in $CD90^+$ cells by age. Statistical testing: ratio paired, two tailed t tests
838 in n = 5 mice per condition. For all plots (**C-E**), Wnt3a-bandage (dark blue points), inactive bandage (white
839 points), Adult (blue), Aged (grey).

840

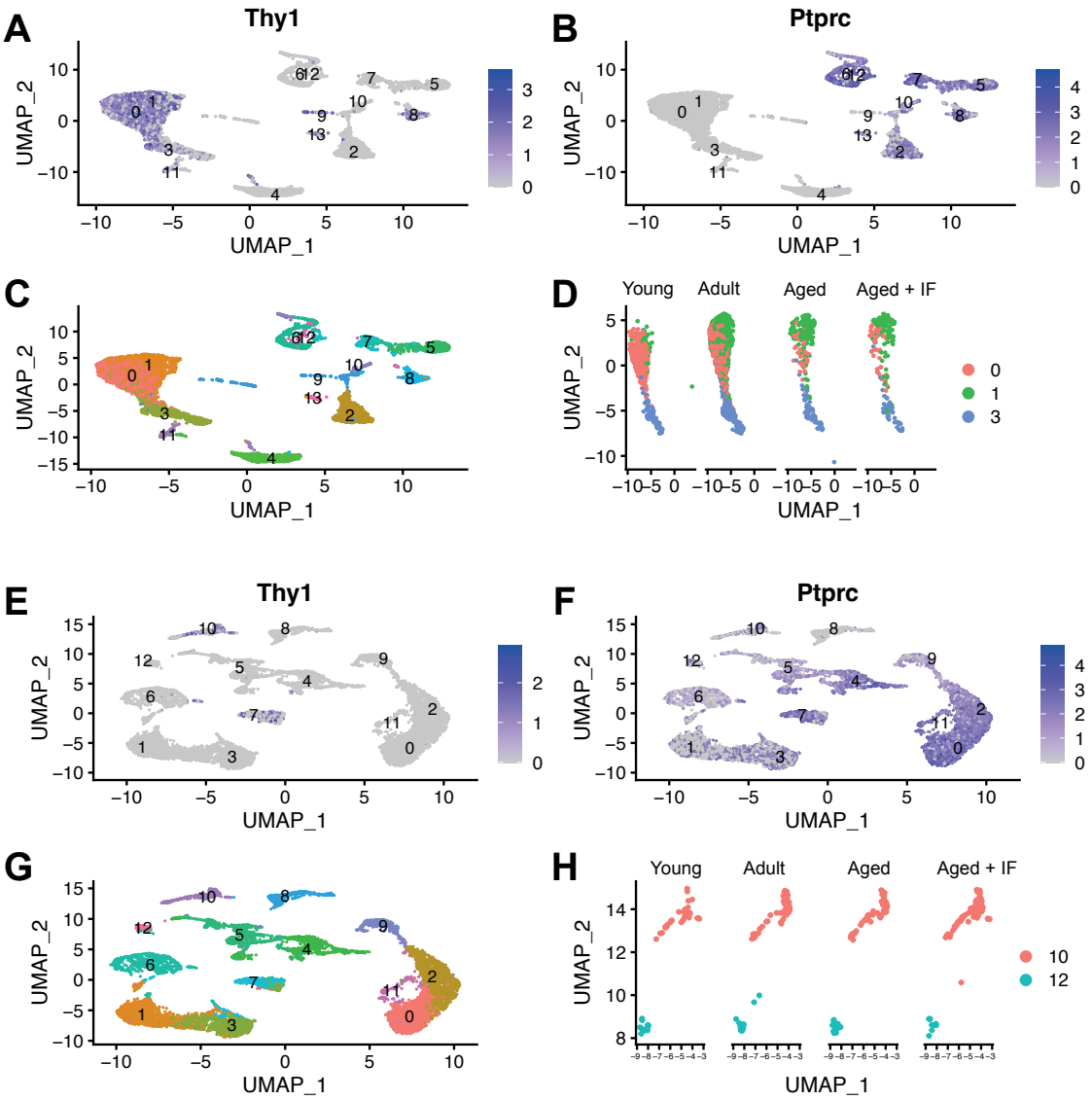
A
Thy1
B
Ptprc
C
D
Young
Adult
Aged
Aged + IF
E
Thy1
F
Ptprc
G
H
Young
Adult
Aged
Aged + IF
UMAP_1
UMAP_2

841

842 **Figure 2 – figure supplement 1**
843 UMAP-coordinate plot of Thy1 (CD90, **A**) and Ptprc (CD45, **B**) expression in clusters of cells within the
844 periosteum. (**C**) Periosteum cell populations (clusters) as identified through unbiased clustering (**D**) The
845 $CD90^{+}/CD45^{-}$ clusters of interest (0, 1, 3), separated by mouse condition. UMAP-coordinate plot of Thy1
846 (CD90, **E**) and Ptprc (CD45, **F**) expression in clusters of cells within the suture. (**G**) Suture mesenchyme cell
847 populations (clusters) as identified through unbiased clustering (**H**) The $CD90^{+}/CD45^{-}$ cluster of interest (10),
848 and also the small endothelial cluster (12), separated by mouse condition.
849

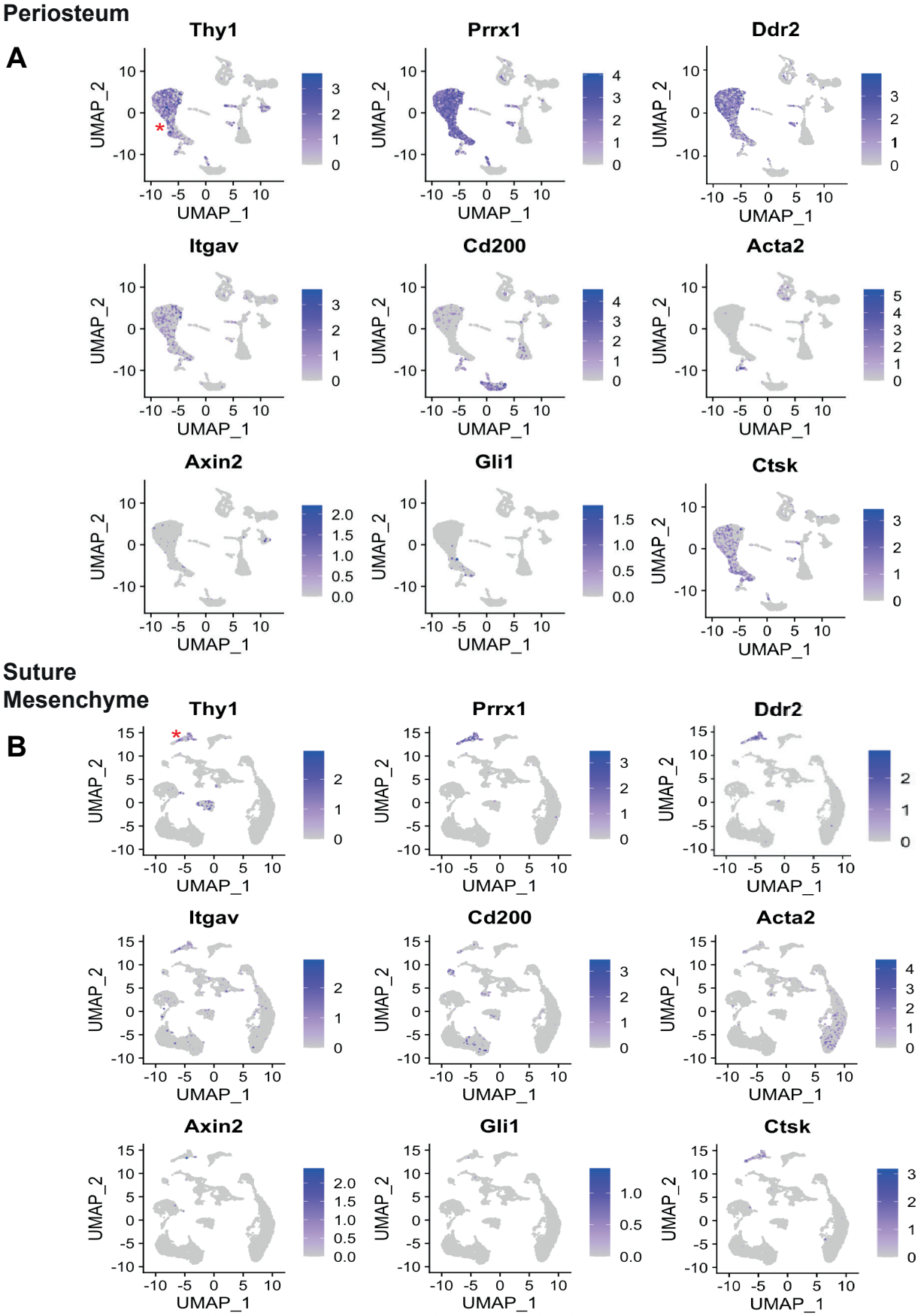
Periosteum
A
Thy1
Prrx1
Ddr2
Itgav
Cd200
Acta2
Axin2
Gli1
Ctsk
UMAP_1
UMAP_2
Suture Mesenchyme
B
Thy1
Prrx1
Ddr2
Itgav
Cd200
Acta2
Axin2
Gli1
Ctsk
UMAP_1
UMAP_2

850

851 **Figure 2 – figure supplement 2**
852 UMAP-coordinate plot of the entire cell populations from Periosteum (**A**) and Suture Mesenchyme (**B**).
853 Expression of SSC markers (purple) highlights clusters of transcriptomically-similar cells. The red asterisk is
854 adjacent to the group of cells referred to as the $CD90^+$ (Thy1) population, which is also $CD45^-$ ($Ptprc^-$) (**Figure**
855 **2 – figure supplement 1**). Prrx1 (Prx1), Ddr2, Itgav (CD51), Cd200 (CD200), Acta2(a-SMA), Axin2, Gli1 and
856 Ctsk (Cathepsin K) are shown.
857

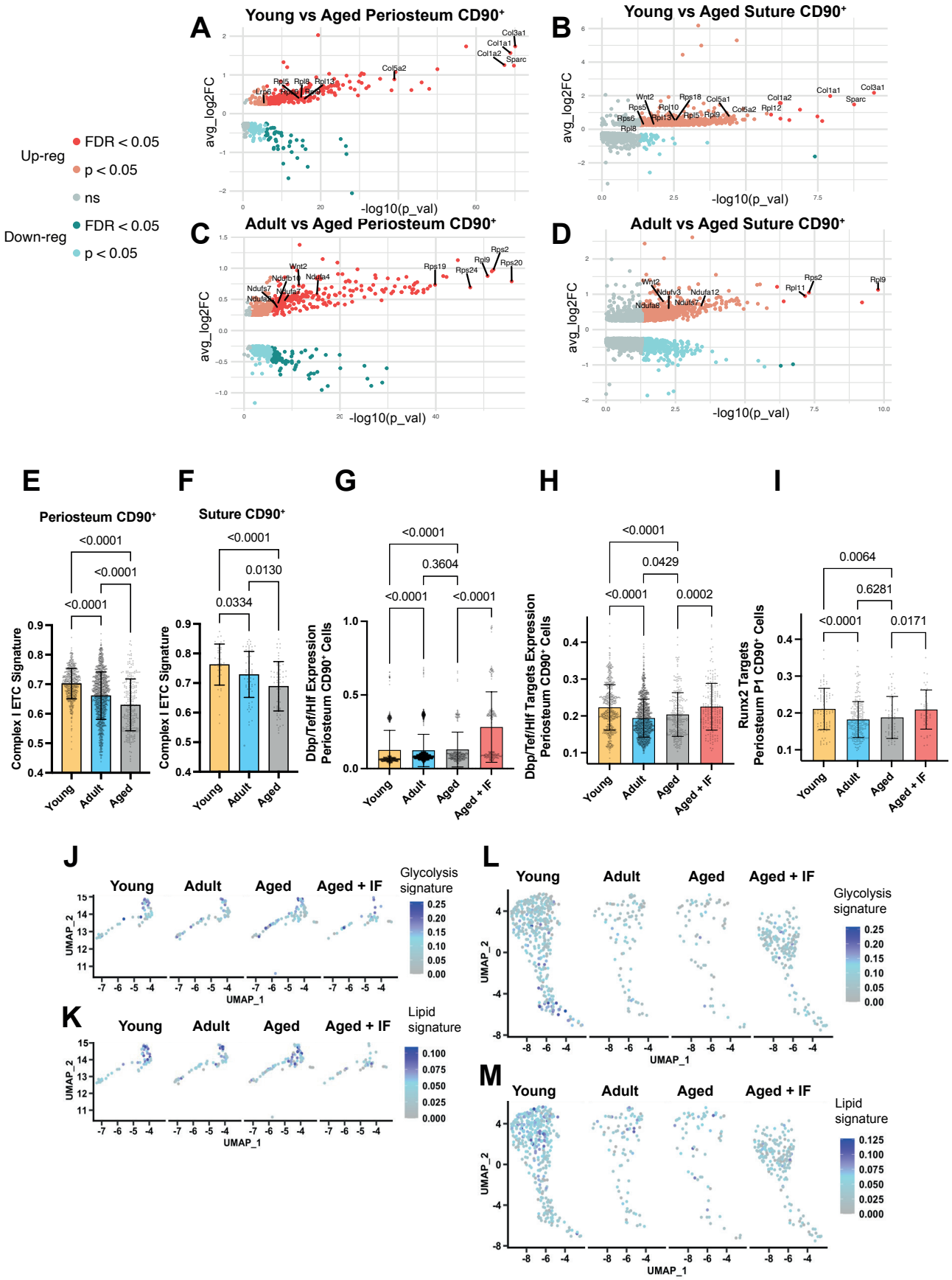
A
Young vs Aged Periosteum CD90+
B
Young vs Aged Suture CD90+
C
Adult vs Aged Periosteum CD90+
D
Adult vs Aged Suture CD90+
avg_log2FC
-log10(p_val)
Up-reg
FDR < 0.05
p < 0.05
ns
Down-reg
FDR < 0.05
p < 0.05
E
Periosteum CD90+
Complex I ETC Signature
F
Suture CD90+
Complex I ETC Signature
G
Dbp/Tef/Hlf Expression Periosteum CD90+ Cells
H
Dbp/Tef/Hlf Targets Expression Periosteum CD90+ Cells
I
Runx2 Targets Periosteum P1 CD90+ Cells
Young
Adult
Aged
Aged + IF
J
Glycolysis signature
K
Lipid signature
L
Glycolysis signature
M
Lipid signature
UMAP_1
UMAP_2

858

859 **Figure 2 – figure supplement 3**
860 (**A-D**) Volcano plots showing differentially-expressed genes in the comparison of the CD90$^+$ population in (**A**)
861 Young vs Aged periosteum; (**B**) Young vs Aged suture; (**C**) Adult vs Aged periosteum and (**D**) Adult vs Aged
862 Suture. Statistical analysis: Wilcoxon Rank Sum test via the FindMarkers function in the Seurat R package.
863 Upregulated (pink: $p < 0.05$; red: FDR-adjusted $p < 0.05$), downregulated (cyan: $p < 0.05$; teal: FDR-adjusted
864 $p < 0.05$), and non-significant (ns) genes are displayed on axes of log fold expression (y, avg_log2FC) against
865 p transformed as its negative log value. (**E**) UCell Signature Scoring of transcript expression of genes relating
866 to Complex I electron transport chain (GO-term: 0005747) in the CD90$^+$ clusters of the periosteum and (**F**)
867 suture. Statistical analysis: Uncorrected Dunn's tests; $n \geq 242$ cells in periosteum per age group, $n \geq 39$ cells
868 in suture per age group. (**G**) UCell Signature Scoring of transcript expression of transcription factors Dbp +
869 Tef + Hlf themselves and (**H**) their combined transcriptional gene targets in the CD90$^+$ clusters of the
870 periosteum. Statistical analysis: Uncorrected Dunn's tests; (**G**) $n \geq 194$; (**H**) $n \geq 194$. (**I**) UCell Signature Scoring
871 of transcript expression of transcriptional targets of Runx2 in the P1 CD90$^+$ cluster subset of the periosteum.
872 Statistical analysis: Uncorrected Dunn's tests; $n \geq 46$ cells per condition.
873 (**J-M**) UMAP-coordinate plot of the CD90$^+$ cells in the periosteum (**J, K**) and suture mesenchyme (**L, M**) for
874 the glycolysis and lipid UCell Signature scoring.
875
876

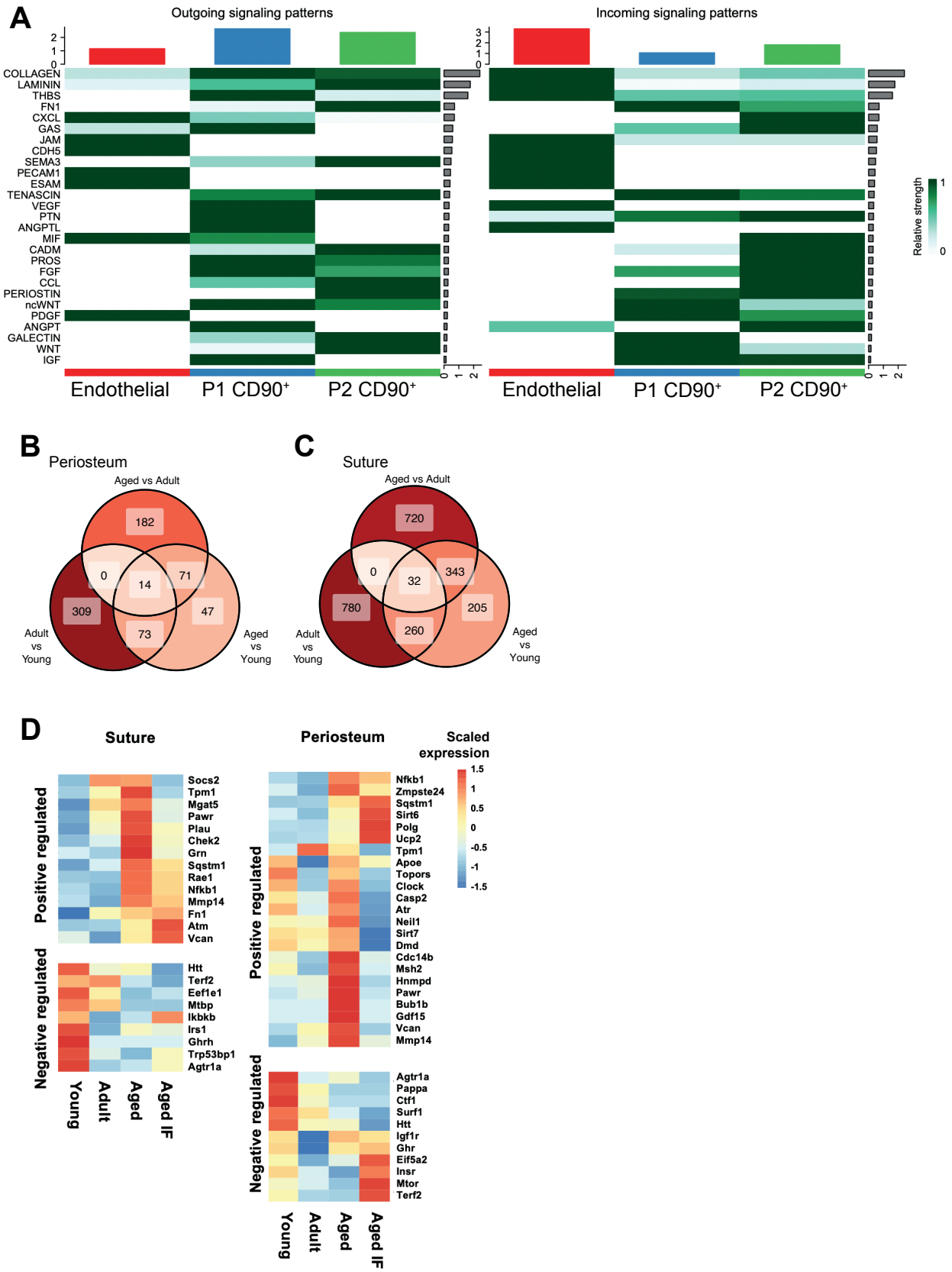
A
Outgoing signaling patterns
Incoming signaling patterns
COLLAGEN
LAMININ
THBS
FN1
CXCL
GAS
JAM
CDH5
SEMA3
PECAM1
ESAM
TENASCIN
VEGF
PTN
ANGPTL
MIF
CADM
PROS
FGF
CCL
PERIOSTIN
ncWNT
PDGF
ANGPT
GALECTIN
WNT
IGF
Endothelial
P1 CD90+
P2 CD90+
Relative strength
B
Periosteum
Aged vs Adult
182
0
14
71
309
47
73
Adult vs Young
Aged vs Young
C
Suture
Aged vs Adult
720
0
32
343
780
205
260
Adult vs Young
Aged vs Young
D
Suture
Periosteum
Scaled expression
Positive regulated
Negative regulated
Socs2
Tpm1
Mgat5
Pawr
Plau
Chek2
Grn
Sqstm1
Rae1
Nfkb1
Mmp14
Fn1
Atm
Vcan
Htt
Terf2
Eef1e1
Mtbp
Ikbkb
Irs1
Ghrh
Trp53bp1
Agtr1a
Nfkb1
Zmpste24
Sqstm1
Sirt6
Polg
Ucp2
Tpm1
Apoe
Topors
Clock
Casp2
Atr
Neil1
Sirt7
Dmd
Cdc14b
Msh2
Hnmpd
Pawr
Bub1b
Gdf15
Vcan
Mmp14
Agtr1a
Pappa
Ctf1
Surf1
Htt
Igf1r
Ghr
Eif5a2
Insr
Mtor
Terf2
Young
Adult
Aged
Aged IF

877

878 **Figure 2 – figure supplement 4**
879 (**A**) CellChat analysis of the relative inferred levels of outgoing and incoming signaling between subsets of
880 periosteal cells, grouped into pathways. P2 contains the Igf1^{high} and Igf1^{low} populations. Green color scale
881 shows relative intensity in outgoing (left) and incoming (right) inferred signaling patterns for pathways shown
882 at the left edge. Red/blue/green boxes at the top show the relative sum of all pathways. (**B**) Three-way Venn
883 diagrams showing the overlap of statistically-significant positively-upregulated differentially-expressed genes
884 ($p < 0.05$) in comparisons between the CD90^{+} clusters in the periosteum and (**C**) suture of Young, Adult, and
885 Aged mice. Color of shading and label shows number of genes shared. The central section shows the number
886 of genes conserved throughout all comparisons. (**D**) Heatmaps of gene expression in CD90^{+} cells from suture
887 and periosteum mesenchyme of young, adult, aged and aged + IF mice. Scaled expression of genes positively
888 regulated and negatively regulated in senescent cells.
889

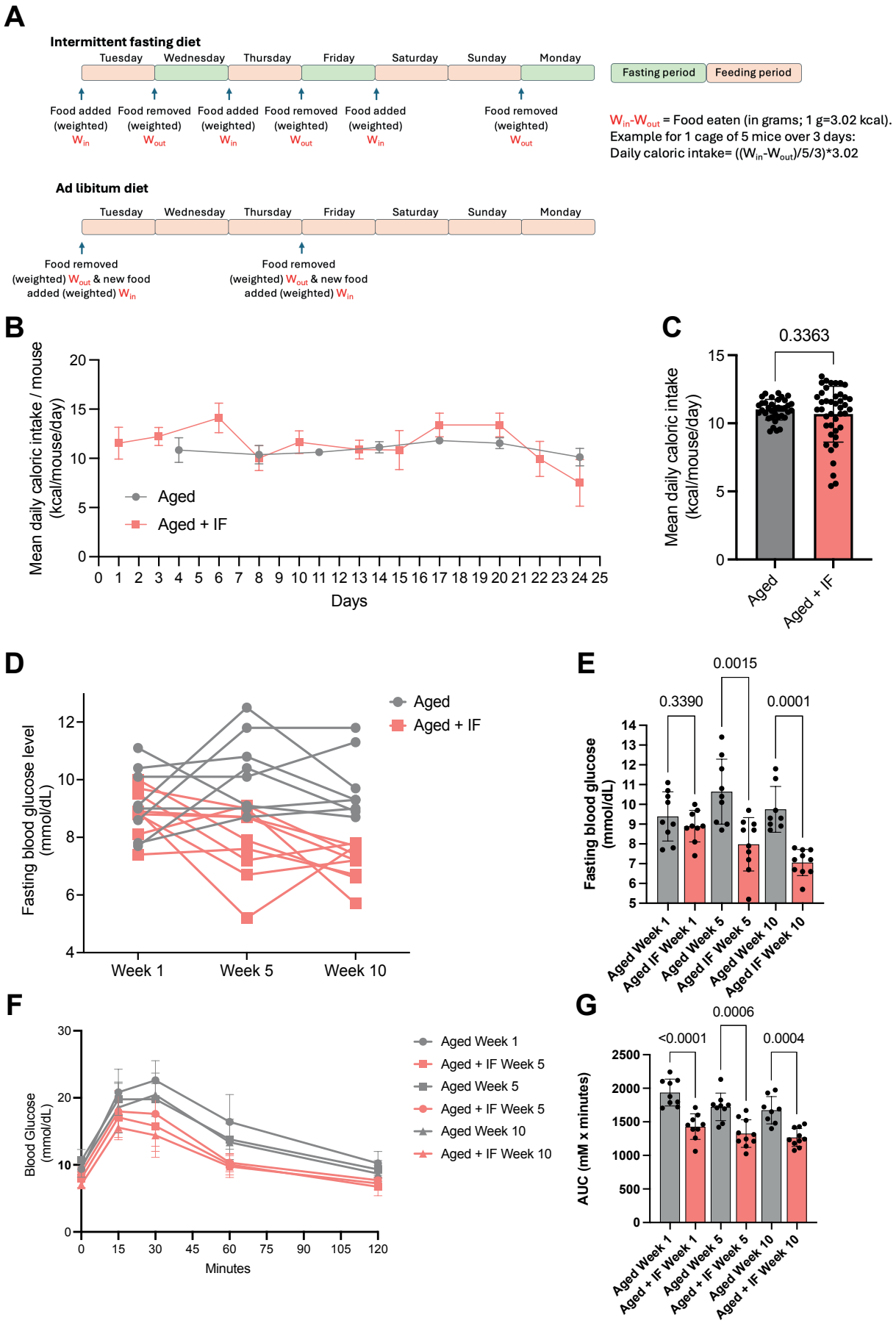
A
Intermittent fasting diet
Tuesday
Wednesday
Thursday
Friday
Saturday
Sunday
Monday
Fasting period
Feeding period
Food added (weighted) Win
Food removed (weighted) Wout
Food added (weighted) Win
Food removed (weighted) Wout
Food added (weighted) Win
Food removed (weighted) Wout
Win-Wout = Food eaten (in grams; 1 g=3.02 kcal).
Example for 1 cage of 5 mice over 3 days:
Daily caloric intake= ((Win-Wout)/5/3)*3.02
Ad libitum diet
Food removed (weighted) Wout & new food added (weighted) Win
Food removed (weighted) Wout & new food added (weighted) Win
B
Mean daily caloric intake / mouse (kcal/mouse/day)
Aged
Aged + IF
Days
C
0.3363
Mean daily caloric intake (kcal/mouse/day)
Aged
Aged + IF
D
Fasting blood glucose level (mmol/dL)
Aged
Aged + IF
Week 1
Week 5
Week 10
E
0.3390
0.0015
0.0001
Fasting blood glucose (mmol/dL)
Aged Week 1
Aged IF Week 1
Aged Week 5
Aged IF Week 5
Aged Week 10
Aged IF Week 10
F
Blood Glucose (mmol/dL)
Minutes
Aged Week 1
Aged + IF Week 5
Aged Week 5
Aged + IF Week 5
Aged Week 10
Aged + IF Week 10
G
<0.0001
0.0006
0.0004
AUC (mM x minutes)
Aged Week 1
Aged + IF Week 1
Aged Week 5
Aged + IF Week 5
Aged Week 10
Aged + IF Week 10

890

Figure 3 – figure supplement 1

(**A**) Schematic explaining the approach and measure of the food intake transcripted into caloric intake for the AL and IF diets protocols. (**B**) Calculated daily caloric intake for mouse with ad libitum diet or intermittent fasting diet for the first 24 days of treatment. For each time point, n cage ≥ 3 with 1 to 5 mice/cage. (**C**) Mean daily caloric intake over the 24 days. Data are expressed as mean ± SD with Welch's t-test n ≥ 36. (**D, E**) Fasting blood glucose levels at Weeks 1, 5, and 10 post surgeries. n ≥8 mice/group. (**D**) Connecting curve representation of the fasting blood glucose levels. Each data point is a single dosage; dosages from a same mouse are connected with a line. (**E**) Group comparison for each time point. Data are expressed as mean ± SD with Welch's ANOVA test. (**F, G**) Blood glucose levels during intraperitoneal glucose tolerance test (IPGTT). (**F**) Blood glucose levels over time during the IPGTT. Data are expressed as mean ± SD with n ≥8 mice/group. (**G**) Area under the curves (AUC) of the IPGTT. Data are expressed as mean ± SD with Welch's ANOVA test. n ≥8 mice/group.

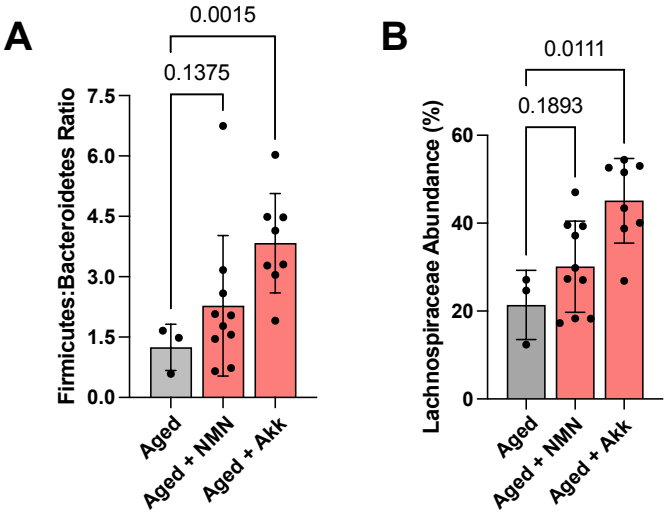
A
0.0015
0.1375
Firmicutes:Bacteroidetes Ratio
7.5
6.0
4.5
3.0
1.5
0.0
Aged
Aged + NMN
Aged + Akk
B
0.0111
0.1893
Lachnospiraceae Abundance (%)
60
40
20
0
Aged
Aged + NMN
Aged + Akk

904

905 **Figure 5 – figure supplement 1**
906 (**A**) The relative abundance of Firmicutes to Bacterioides bacteria and (**B**) Lachnospiraceae bacteria, as
907 measured by 16S metagenomic profiling. Statistical analysis: Welch's tests on n = 3 (Aged), n = 10 (Aged +
908 NMN), n = 8 (Aged + Akk).
909

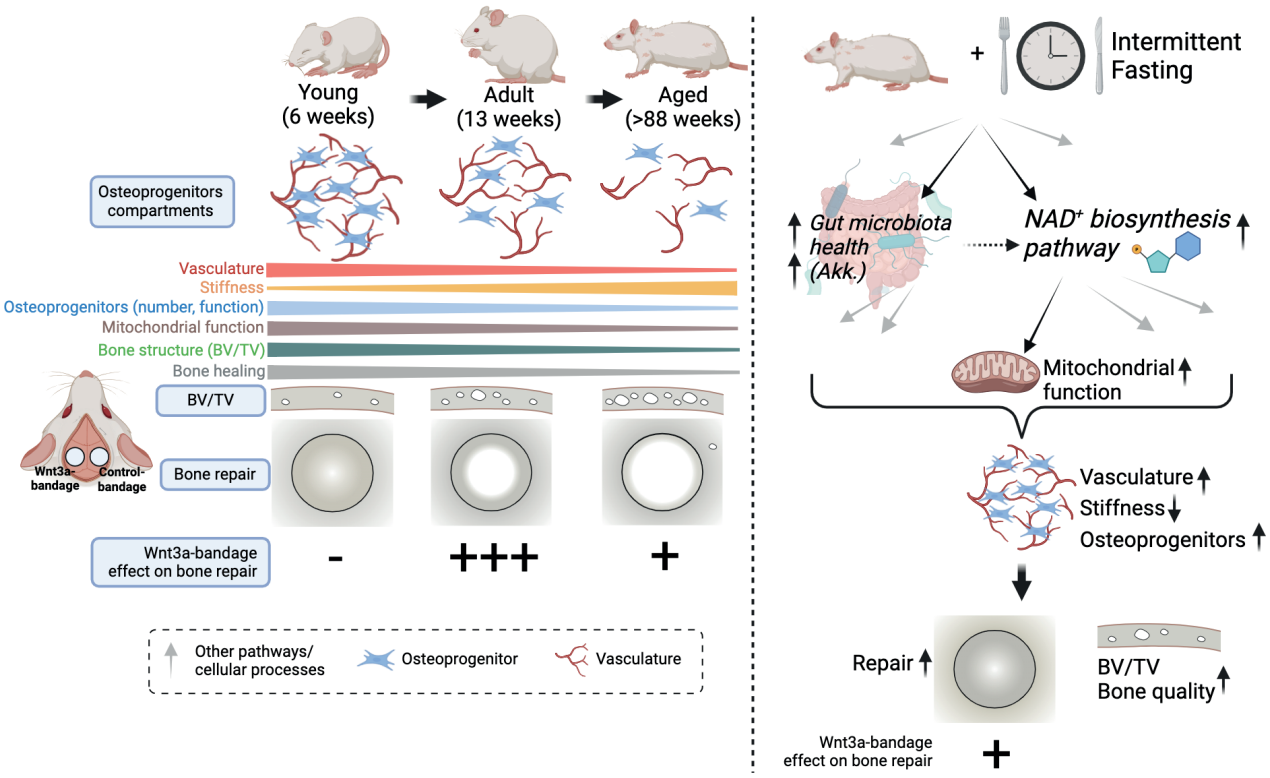
Young
(6 weeks)
Adult
(13 weeks)
Aged
(>88 weeks)
Osteoprogenitors compartments
Vasculature
Stiffness
Osteoprogenitors (number, function)
Mitochondrial function
Bone structure (BV/TV)
Bone healing
BV/TV
Wnt3a-bandage
Control-bandage
Bone repair
Wnt3a-bandage effect on bone repair
-
+++
+
Other pathways/ cellular processes
Osteoprogenitor
Vasculature
Intermittent Fasting
Gut microbiota health (Akk.)
NAD+ biosynthesis pathway
Mitochondrial function
Vasculature
Stiffness
Osteoprogenitors
Repair
BV/TV
Bone quality
Wnt3a-bandage effect on bone repair
+

Appendix 2 – figure 1

Schematic that recapitulates the mains findings of the study. Created in BioRender. Habib, S. (2024) https://BioRender.com/z14r452.

Materials and Methods

Wnt3a bandage manufacture

Polycaprolactone (PCL)-based polymer film (Poly-Med) was plasma-treated using a plasma etching electrode in oxygen gas at a flow of 20 $cm^3 min^{-1}$ with a radio frequency plasma generator (frequency 13.56 MHz, power 50 W, Diener electronic Zepto-W6) at 0.2 mbar pressure for 3 min. Treated films were immediately incubated in 5% (3-Aminopropyl)triethoxysilane (APTES, Sigma, 440140) in ethanol (dark, room temperature, 2 hours), before washing twice with 100% ethanol (room temperature, 10 minutes), and allowed to air dry. Circular bandages were cut using a 5mm biopsy punch (Stiefel) and placed in 10 mg/ml succinic anhydride (Sigma Aldrich, 239690-50G) in 0.4M borate buffer (Sigma Aldrich, B7660) pH=9 (room temperature, 30 minutes). Bandages were twice washed in 25mM Morpholineethanesulfonic acid (MES) buffer pH 5 (Sigma Aldrich, M3671), then incubated in a MES buffer solution containing 50 mg/ml N(3Dimethylaminopropyl)-N′-ethylcarbodiimide hydrochloride (EDC, Sigma Aldrich, E7750) and 50 mg/ml NHydroxysuccinimide (NHS, Sigma Aldrich, 56480) (room temperature, 30 minutes), and washed twice again in MES buffer. Bandages are individually placed on a sterile flat surface and briefly allowed to air-dry. 300ng Wnt3a (R&D, 1324-WN-010) was diluted to 23 µL in MES buffer, and this liquid added as a droplet on top of the bandage for 1 hour at room temperature.

For inert control bandages (inactive-bandages), the bandages were then placed into a 96 well plate and washed with PBS. 20 mM Dithiothreitol (DTT, Roche, 10197777001) in 50 µL ddH_2O was then added and incubated (37℃, 30 minutes). Active Wnt3a-bandages were also placed in the 96 well plate, and then all bandages were washed with PBS, and quenched with 2% Fetal Bovine Serum (FBS, Sigma Aldrich, F7524) in Dulbecco's Modified Eagle Medium (DMEM, Thermo Fisher, 41966) (room temperature, 15 minutes) in preparation for their surgical implantation.

Wnt3a-bandage testing

The Wnt/β-catenin pathway activation of Wnt3a-bandages was confirmed as previously published (Lowndes et al. 2017). Wnt3a-bandages were tested for Wnt/β-catenin pathway activation using Comma-D Beta cells harboring GFP expression under the control of a TCF-LEF promoter (Lowndes et al. 2016) (**Figure 1 – figure supplement 3a, c**). Similarly, LS/L cells harboring luciferase under control of a 7xTCF promoter were used to quantitatively test Wnt3a-bandages, as described previously (Okuchi et al. 2021) (**Figure 1 – figure supplement 3a, c**).

Animal experimentation methods according to the ARRIVE Essential 10 guidelines

All procedures involving animals were carried out by holders of Personal Licences (PIL) under a Project Licence (PPL number: P8F273FDD, S.J.H.) shaped by ARRIVE and NC3Rs guidelines. The PPL was approved by the Animal Welfare and Ethical Review Body (AWERB) at King's College London and granted by the Home Office under the Animals (Scientific) Procedures Act 1986 (ASPA) and Amendment Regulations 2012.

Study design

Within each animal, the bone repair under the Wnt-bandage was compared to the one under the inactive bandage wherever appliable. Between groups of treatments, the bone repair was compared to other groups, or to a control group (sham treatment/ad libitum feeding). Each animal was used as an experimental unit.

Sample size

10 animals were used per surgical group for a total of 60 animals. The minimum is 7 animals/ group to get statistically reliable tests of the hypothesis (80% power with 0.05 type I error). We applied the resource equation method (Charan and Kantharia, 2013). Based on our experience 8-10 animals were used per group, to account for morbidity and animal variability (Okuchi et al., Nature Materials 2021).

Inclusion and exclusion criteria

All animals were included in the study. Animals that were scarified/found dead before the end of the study were excluded (two for the group “Adult” (n=8), and one for the groups “Aged” (n=9) and “Aged + Akk.” (n=9), n=10 in all other groups).

Randomization

Randomization method was not applied to assign animals to experimental groups. Animals were identified using ear notches.

Blinding

The experimenter was aware of the group allocation of the animals when performing the experiments and during the data acquisition and analysis.

Outcome measures

Bone repair was assessed using microCT as described in the Micro-Computed Tomography section, and subsequent histological analysis and immunology staining were performed on cryosections as described in the Sample Processing and Cryosectionning, and Fluorescence Immunostaining sections.

Experimental animals

Female mice were chosen for their delayed healing and higher fracture risk (Haffner-Luntzer et al., 2021; Ortona et al., 2023), leading to a more challenging case for bone repair, making them a stringent test for evaluating the effectiveness of our rejuvenation approaches. Female C57BL6/J mice (Charles River, strain 632) were housed in conditions that comply with the Animals (Scientific) Procedures Act 1986 (ASPA). Mice were group housed (2-5 mice/cage) under 7 a.m.-7 p.m. lighting and fed with standard mouse food pellets (LabDiet, 5053). Three age groups were used for this study: Young (6 weeks), Adult (13 weeks), and Aged mice (> 88 weeks).

For *ad libitum* diet, the food was renewed every 3 to 4 days. During intermittent fasting, food was removed from cages at 10 a.m. on Monday, Wednesday, and Friday, and returned at 10 a.m. on Tuesday, Thursday, and Saturday, such that the maximum time without food was 24 hours. Intermittent fasting started the day after the surgery and was performed for 10 weeks.

Caloric intake calculation

To assess the caloric intake of mice, the food was weighted when made available to the mice (W_{in}), and when removed (W_{out}). The daily consumed food was calculated based on the weight difference (W_{in} - W_{out}), then converted to kcal (1 g = 3.02 kcal, LabDiet, 5053), and expressed as kcal/mouse/day for each cage (n cage $\geq$ 3 with 1 to 5 mice/cage).

Blood glucose level measurement

Fasting blood glucose levels were measured (Accu-Check tests strips) from 6h fasting mice by blood sampling the tail vein. For intraperitoneal glucose tolerance test (IPGTT), glucose was injected intraperitoneally (2 g/kg), and the blood glucose levels were measured after 15, 30, 60 and 120 minutes.

Experimental procedures

1010 **Calvarial Defect**
1011 All steps of surgery were carried out under aseptic conditions. Mice were intraperitoneally anaesthetized with
1012 10 μL/g bodyweight of anesthesia cocktail (7.5 mg/ml Ketamine hydrochloride (Ketavet) and 0.1 mg/ml
1013 Medetomidine hydrochloride (Domitor) in 0.9% sterile saline). Loss of consciousness was confirmed with lack
1014 of pedal and tail reflexes. The top of the head was shaved, cleaned, and prepared for surgery, before a ~8
1015 mm central incision was made in the skin with surgical scissors. The periosteum was gently pushed towards
1016 the outer edges of the calvaria, and the location of the sutures noted. A 2 mm diameter full thickness defect
1017 was drilled into the middle of the parietal bone on both sides of the skull, ensuring irrigation was applied to
1018 limit heat buildup. A small amount (~10 μL) of 1 mg/ml collagen gel (Corning, 354249) (diluted with DMEM
1019 and set with 3 mM sodium hydroxide (Sigma Aldrich, S5881)) was placed into the defect to exclude trapped
1020 air, and the required bandages were placed face down over the defect. Small dots of glue (3M, Vetbond) were
1021 applied at the edges of the bandages to affix them to the surface of the skull. The skin was then approximated
1022 and glued to ensure closure of the wound. Mice were administered 10 μL/g bodyweight of the recovery cocktail
1023 intraperitoneally (0.125 mg/ml Atipamezole hydrochloride (Antisedan) and 0.01 mg/ml Buprenorphine
1024 hydrochloride (Vetergesic) in 0.9% sterile saline) and placed in a warmed cage (35 ℃). Mice typically became
1025 conscious within 20 minutes, began moving around the cage within 40 minutes, and were feeding within 2
1026 hours. Mice showed no signs of distress or pain the following day and were externally monitored daily for the
1027 healing of the skin wound. Following surgery, mice were maintained under standard conditions for 10 weeks,
1028 and group housed (2-5 mice/cage) where possible.
1029
1030 **NMN supplementation**
1031 600 mg/kg bodyweight doses of β-nicotinamide mononucleotide (NMN, APExBIO, B7878), dissolved in water
1032 were given by flexible-tipped oral gavage 3 times per week, not on consecutive days, from 2 weeks before
1033 surgery to 2 weeks after, a total of 4 weeks.
1034
1035 **Anaerobic Culture of *Akkermansia muciniphila***
1036 Preserved *Akkermansia muciniphila* (Collection de l'Institut Pasteur, CIP107961T) was resuspended and
1037 cultured in Gifu's Anaerobic Medium (GAM) broth (Nissui Pharmaceutical, 05422) in an anaerobic
1038 environment (80% Nitrogen, 10% Carbon dioxide, 10% Hydrogen). Aliquots were cryopreserved in 50%
1039 glycerol (Sigma Aldrich, G2025) in PBS. Post-thawing viability was determined by serial dilution of
1040 cryopreserved aliquots, plating onto GAM-Agar (Sigma Aldrich, 01916) plates, and 24-hour anaerobic culture.
1041
1042 ***Akkermansia muciniphila* supplementation**
1043 Cryopreserved doses of 2.0 x 10^8 C.F.U. *Akkermansia muciniphila* were warmed to ~ 30℃ and administered
1044 to Aged mice by flexible-tipped oral gavage 3 times per week, not on consecutive days, from 2 weeks before
1045 surgery to 6 weeks after, a total of 8 weeks.
1046
1047 **Results**
1048 Results are displayed as mean ± SD. All numerical values are available in the Source Data files.
1049
1050 **Ethical Approval for animal experimentation**
1051 All procedures involving animals were carried out by holders of Personal Licences (PIL) under a Project
1052 Licence (PPL, P8F273FDD, S.J.H.) shaped by ARRIVE and NC3Rs guidelines. The PPL was approved by
1053 the Animal Welfare and Ethical Review Body (AWERB) at King's College London and granted by the Home
1054 Office under the Animals (Scientific) Procedures Act 1986 (ASPA) and Amendment Regulations 2012.
1055
1056 **Microbiome Profiling**
1057 Feces samples were freshly collected and snap-frozen in liquid nitrogen. Samples were submitted for full
1058 length (V1-V9) 16S metagenomic profiling. Amplification with KAPA HiFi HotStart ReadyMix PCR Kit (KAPA)
1059 and 16S barcode primers (PacBio) preceded library preparation SMRTbell Express Template Prep 2.0

(PacBio). Samples were sequenced via the Illumina MiSeq to generate amplicon sequence data specifying the V3-V4 regions of the 16S rRNA ribosomal subunit. The metagenomic analysis was conducted using the amplicon sequence variant (ASV) method of taxonomic classification facilitated by DADA2 (Callahan et al. 2016) incorporated by the Qiime2 package (Bolyen et al. 2019). Quality control metrics of the amplicon data was visualized by FastQC (Andrews S. 2015). The data was cleaned, via removal of adapters and low-quality sequences, using Trimmomatic (Bolger et al. (2014) and Qiime2.

Micro-Computed Tomography

Mice were culled by cervical dislocation and their tissues immediately collected. Whole calvarial samples were fixed in 4% PFA (room temperature, overnight) and washed in PBS. Fixed samples were scanned on a µCT50 micro-CT scanner (Scanco) in 19 mm scanning tubes, using voxels of side length 10 µm, X-ray settings of 70 kVp and 114 µA and using a 0.5 mm aluminum filter to attenuate harder X-rays. Scans were reconstructed and calibrated using known densities of hydroxyapatite (HA) between 0 and 790 mg HA cm^{-3}, with absorption values expressed in Hounsfield Units (HU). 3D volumes were constructed from raw data in SCANCO Visualizer 1.1, and signal of less than 250 mg HA cm^{-3} was considered non-mineralized and was set as the black level in displayed images.

Sample Processing and Cryosectionning

Fixed samples were decalcified in 10% formic acid (room temperature, overnight), then washed in PBS. Dehydration was carried out in 30% sucrose/PBS (room temperature, overnight), followed by 30% sucrose/30% OCT/PBS (room temperature, overnight). Samples were embedded in 100% OCT solidified with dry ice and stored at -80℃. Cryosections were cut at 14 µm thickness using a cryostat microtome at -23℃. Cut sections were stored at -20℃.

Fluorescence Immunostaining

Sections were rehydrated to ddH_2O. Antigen retrieval was performed with 0.05% v/v Tween-20 (Sigma Aldrich, P9416) in 10 mM Tris (Sigma Aldrich, 93362), 1 mM EDTA (Sigma Aldrich, E6758), pH=9.0 (40℃, 30 minutes). Sections were then permeabilized with 0.1% Triton X-100 (Sigma Aldrich, 93443) in 1% Bovine Serum Albumin (BSA, Sigma Aldrich, A2153) in phosphate buffered saline (PBS, Sigma Aldrich, P4417) (1% BSA/PBS) (room temperature, 5 minutes), washed with 1% BSA/PBS, and individual staining regions were designated with hydrophobic delimiting pen (Agilent, S200230-2).

Primary antibodies were diluted in 0.05% Triton-X in 1% BSA/PBS and incubated in a humid chamber (4℃, overnight). Triplicate washes of 0.1% Triton-X in 1% BSA/PBS were carried out (room temperature, 10 minutes). Secondary antibodies were diluted in 0.05% Triton-X in 1% BSA/PBS, with 5 µg/ml DAPI (Sigma Aldrich, D9542), and 1:400 dilution Phalloidin-488 (Thermo Fisher, A12379) and incubated in a humid chamber (room temperature, 1 hour). Triplicate washes of 0.1% Triton-X in 1% BSA/PBS were carried out (room temperature, 10 minutes) before mounting with aqueous mounting media (Abcam, ab128982). Immunostained sections were imaged with an inverted spinning disk confocal microscope (Nikon, NISElements Viewer 5.2 software). Optimal z-axis step size was determined according to the Nyquist criteria for sampling. Images were post-processed and analyzed through ImageJ/FIJI.

Primary antibodies

Anti-Endomucin (Emcn) 1:100 (Santa Cruz, sc-65495)
Anti-CD90/Thy1, 1:100 (Abcam, ab3105)
Anti-phosphoAMPK (Thr183, Thr172), 1:100 (Thermo Fisher, 44-1150G)
Anti-ATPB, 1:100 (Abcam, ab128743)

Anti-Ki67, 1:100 (Thermo Fisher, MA5-14520)
Anti-p16INK4a, 1:100 (Abcam, ab211542)
Anti-beta-catenin 1:100 (Abcam, ab32572)
Anti-MMP2, 1:100 (Abcam ab92536)
Anti-CD31, 1:100 (Novus Biologicals, NB100-2284)
Anti-Lamin B1, 1:100 (Abcam, ab16048)

Secondary antibodies

Chicken anti-Rat-647 1:1000 (Thermo Fisher, A21472)
Donkey anti-Rabbit-555 1:1000 (Thermo Fisher, A32816)

Fluorescence thresholding quantification

See **Figure 1 - figure supplement 1e.** Sample tissue sections were immunostained alongside controls that lacked primary antibody: the 'no primary control'. These control samples were imaged using the same microscope settings as the experimental samples, and maximum projections were calculated to reduce volumetric images to 2D. The maximum pixel intensity in the control images was used to threshold the experimental samples, thereby excluding signal arising from non-specific staining by fluorescent secondary antibodies. Cellular localization of the remaining signal allowed designation of cells positive and negative for the antibody targets of interest.

For quantitative measurements of F-actin/Phalloidin-488 signal intensity (e.g. **Figure 1h**), sum-projections were taken to reduce volumetric 3D images to 2D space. In these quantifications, mean sum pixel intensity was measured and the mean sum background pixel intensity subtracted for $N \geq 56$ cells in $n = 3$ mice.

Tetramethylrhodamine (TMRM) & Hoechst staining in live tissue *ex vivo*

Periosteum was dissected from n = 3 freshly killed mice, and immediately placed in warmed culture media (10% FBS in DMEM) containing 100 nM TMRM (Thermo Fisher, I34361) and 5 µg/mL Hoechst 33342 (Thermo Fisher, H3570) for 30 minutes at 37℃. Tissue was briefly washed with fresh warmed media and imaged on a Zeiss widefield microscope (Zeiss Zen Blue Edition 2.5 software). Explanted cell controls were allowed to migrate from minced suture mesenchyme and attach for 24 hours before identical TMRM/Hoechst staining.

MC3T3 cell culture

MC3T3 (gift from Sophie Verrier, AO foundation, Davos, Switzerland) cells were cultured in MEMα (Thermofisher, A1049001) 10% foetal bovine serum (FBS; Thermofisher A5256701), 1% penicillin-streptomycin (PS; Thermofisher, 15140-122). Cells were used at passages 13-20 and seeded at 25,000 cells / cm^2 for further experiments in glucose- and pyruvate-free DMEM (Thermofisher, 11966025), 10% FBS, 1% PS. All experiments were conducted in differentiation medium, consisting of glucose- and pyruvate-free DMEM 10% FBS, 1% PS, 50 µM ascorbic acid (Merck, 5960), and 2 mM glycerophosphate (Merck, 50020). Alternate serum deprivation was performed by replacing the osteogenic media by serum-free osteogenic media every 1h for 6h. For oligomycin and NMN treatments, cells were treated by 0.1 µM oligomycin (Merck, 75351), with or without 1 mM β-nicotinamide mononucleotide (NMN; APExBio, B7878), or with 0.1% DMSO (Merck, D2438), the vehicle of oligomycin. Cells were treated for 6h before switching to differentiation medium ("oligomycin" or "DMSO" condition) or differentiation medium + 1 mM NMN ("oligomycin + NMN" condition). The media were changed twice a day.

Inhibition of ATP production in MC3T3 and measure of Reactive Oxygen Species (ROS) production

ATP level in cells was measured in 96 well plates after 6h of the treatment induction, using the CellTiter-Glo® 2.0 Assay (Promega, G9241) according to manufacturer's instructions. ROS production was measured in live cells using the CellROX deep red staining kit (Thermofisher, C10422) using a spinning disk microscope (Nikon

Ti2, Crest Optics X-Light V3), with the sum projection intensity normalized by the number of cells using Hoechst staining.

MC3T3 count and mitochondrial activity

Cell count and mitochondrial activity were measured with Hoechst and TMRM staining respectively, using a spinning disk microscope and according to manufacturer's instructions. Z-stacks of 20 µm were acquired and the TMRM sum intensity was normalized to the cell number.

Holographic imaging

Mitochondrial morphology was observed using holotomography imaging on live cells (Tomocube, HT-X1), with a reference refractive index set at 1.337. After reconstruction of the images, mitochondria were categorized in three types according to their shape. The proportion of each morphology type was determined with Tomo Analysis and Fiji software. MitotrackerGreen (Thermofisher, M7514) was used to stain mitochondria and confirm the mitochondrial morphology obtained by holotomography.

RT-qPCR

RNA was extracted according to manufacturer's instructions (Marchery-Nagel, M36006), 12h after the treatment induction. Reverse transcription (Thermofisher, 4374966) and qPCR (Thermofisher, 4368706) were performed according to manufacturer's instruction and mRNA target levels were normalized by beta-Actin mRNA levels using the $2^{-\Delta\Delta Ct}$ method. The following primers have been used (5'→ 3'): *MFN1*: F-AACTTGATCGAATAGCATCCGAG, R-GCATTGCATTGATGACAGAGC; *MFN2*: F-CTGGGGACCGGATCTTCTTC, R-CTGCCTCTCGAAATTCTGAAACT; *DRP1*: F-GGGCACTTAAATTGGGCTCC, R-TGTATTCTGTTGGCGTGGAAC; *PGC1a*: F-AGTGGTGTAGCGACCAATCG, R-AATGAGGGCAATCCGTCTTCA; *ARBP*: F-AGATTCGGGATATGCTGTTGG , R-AAAGCCTGGAAGAAGGAGGTC; *PINK1*: F-CACACTGTTCCTCGTTATGAAGA, R- TTGAGATCCCGATGGGCAAT; *PARKIN*: F-GAGGTCCAGCAGTTAAACCCA; R-CACACTGAACTCGGAGCTTTC; *LC3II* F-TTATAGAGCGATACAAGGGGGAG, R-CGCCGTCTGATTATCTTGATGAG; *ATG5*: F-AAGTCTGTCCTTCCGCAGTC, R-TGAAGAAAGTTATCTGGGTAGCTCA; *LONP1*: F-ATGACCGTCCCGGATGTGT, R-CCTCCACGATCTTGATAAAGCG; *HSP60*: F-CACAGTCCTTCGCCAGATGAG, R-CTACACCTTGAAGCATTAAGGCT; *HPSA9*: FAATGAGAGCGCTCCTTGCTG, R-CTGTTCCCCAGTGCCAGAAC; MTCO1: F-TATGTTCTATCAATGGGAGC, R-GTAGTCTGAGTAGCGTCGTG; beta-Actin: F-GGCTGTATTCCCCTCCATCG, R- CCAGTTGGTAACAATGCCATGT.

Evaluation of the osteoblastic differentiation

Cells were cultured for 2 weeks before the staining of the alkaline phosphatase (ALP; Abcam, ab284936) or mineralized matrix using alizarin red S (ARS; 2% solution in H_2O) (Merck, A5533). ALP staining was performed as per manufacturer's recommendation, and the stained area were quantified using Fiji on pictures taken under a Evos XL core microscope. For ARS staining the cells were fixed with 4% paraformaldehyde in PBS, stained by ARS then imaged using a Evos XL core microscope. The stained mineralized matrix was then dissolved with 10% (v/v) acetic acid in H_2O and optical density was measured at 405 nm to quantify the amount of dissolved ARS.

Statistical analysis

Statistical analysis was performed in GraphPad Prism 9. All data are plotted as mean, with error bars indicating standard deviation. Typically, experimental data was analyzed from all mouse conditions together using one-way ANOVA, with individual comparisons between conditions/regions of interest displayed on figures as Welch's two-tailed unpaired tests. Welch's ANOVA was used instead of ordinary ANOVA because it is more conservative and reduces the risk of false-positive p-values. Two-factors comparisons were analyzed with two-way ANOVA with uncorrected Fisher's LSD test. Only the statistical values for the

hypotheses being tested are shown; multiple comparison corrections were not applied. Ratio-paired two-tailed t-test was used in comparisons within the same mouse (i.e., comparisons of Wnt3a-bandage vs Inactive-bandage). Correction of multiple comparison was not applied as each p-value was considered for itself. On some tested groups, correction for multiple comparison did not change our general conclusions. Uncorrected Dunn's tests were performed for the statistical analysis of UCell gene-expression signature scoring, as a non-parametric test for non-Gaussian distributions of data.

RNAseq sample processing

Periosteum and suture mesenchyme were separately dissected and pooled from ≥ 3 live mice from each condition, briefly minced with a scalpel blade, and immediately placed in 250 µL of a solution of 0.5 mg/ml Liberase TL (Roche, 05401020001) and 0.1 mg/ml DNaseI (Sigma Aldrich, DN25) in Hanks' Balanced Salt Solution (HBSS, Gibco, 14170-120) and incubated for 25 minutes at 37℃ with shaking (600 rpm). The digestion was quenched with ice-cold 1mL buffer (3% FBS in PBS), passed through a 100 µm cell strainer (Corning, 352360), and centrifuged (500 g, 5 minutes, 4℃). The supernatant was removed, and the cell pellet gently resuspended in staining solution containing 0.1 µg 'hashtag' antibody, 50 µM DRAQ5 (Invitrogen, 65-0880-92), and 1:4000 DAPI in ice-cold 3% FBS/PBS. Up to 4 samples were individually stained with TotalSeq™ antibodies 1-4 (Biolegend 155801, 155803, 155805, 155807). Samples were centrifuged, washed with 3% FBS/PBS, centrifuged again and resuspended in 3% FBS/PBS for single-cell FACS. The gating strategy took single (by forward and side scatter), nucleated ($DRAQ^+$), live ($DAPI^-$) cells, and up to 4 individually-hashtagged samples were multiplexed together by sorting equal cell numbers into the same collection tube, and stored on ice to preserve viability. Cells were loaded onto a 10X Chromium controllers and the library generated through single cell 10X 3' v3.1 gene expression. All libraries were sequenced together using NextSeq 2000 sequencing on a P3 flow cell.

RNAseq data processing

Initial alignment and processing were performed through the CellRanger pipeline. Further quality control, processing, and analysis was carried out through the Seurat (v4) package (Hao et al. 2021) and additional packages in R software (R Core Team (2022), v4.2.1). Cells were graded for proportion of mitochondrial genes, and this metric regressed. The immune cell $CD45^+$ populations in the samples ($Ptprc^{high}$) were removed from downstream analyses. $CD90^+/CD45^-$ ($Thy1^{high}/Ptprc^{low}$) clusters were considered the populations of interest. Differential expression of lincRNA Gm42418 was identified as an artefact and removed from the data, as has been done in other studies (Kimmel et al. 2019). For calculation of Gene Ontology (GO) and KEGG enrichment of sets of differentially expressed genes, ShinyGO 0.76.3 (Ge, Jung, and Yao 2020) was used to calculate false discovery rate (FDR) and fold enrichment (FE) values. Full details of differentially expressed genes in comparisons between ages, diets, and $CD90^+$ subpopulations are available in Source Data 2.

To construct the senescence signature, we obtained mouse aging-related genes from the GenAge database (https://genomics.senescence.info/genes/search.php?organism=Mus+musculus&show=4). The genes were categorized into two groups: positively regulated and negatively regulated. Positively regulated genes are defined as those with high expression levels associated with senescence, while negatively regulated genes are defined as those with low expression levels associated with senescence. The genes were clustered based on their expression, then we selected the highly expressed cluster in the positively-regulated genes and the poorly expressed cluster in negatively-regulated genes in the Aged group.

For the glycolysis and lipid catabolic processes signatures, we obtained mouse metabolism-related genes from AmiGO2 database (https://amigo.geneontology.org/amigo) with Ontology ID: GO:0061621 (glycolysis) and GO:0050996 (positive regulation of lipid catabolic process), and we clustered the genes based on their expression levels. Heatmaps were drawn by R package pheatmap (version 1.0.12).

Data availability

All numerical data included in the production of figures, plots and statistical analysis will be found in the Source Data. Additional statistical analysis values (F values, t values, degrees of freedom and p values) will be presented in the Source Data documents. Source Data will be provided with this paper. Raw and processed single cell RNAseq data will be available under a GEO accession number during the revision/review process.

Authors and Affiliations

Department of Biomedical Sciences, University of Lausanne, Lausanne, Switzerland
Joshua Reeves, Pierre Tournier, Pierre Becquart & Shukry J. Habib

Centre for Gene Therapy and Regenerative Medicine, King's College London, London, UK
Joshua Reeves, Robert Carton & Alessandra Vigilante

Zhejiang Provincial Key Laboratory for Cancer Molecular Cell Biology, Life Sciences Institute, Zhejiang University, Hangzhou, Zhejiang 310058, China
Department of Medical Oncology, Key Laboratory of Cancer Prevention and Intervention, Ministry of Education, The Second Affiliated Hospital, Zhejiang University School of Medicine, Hangzhou, Zhejiang, China
Yin Tang & Dong Fang

Author Contributions

S.J.H. conceived the project and with J.R. designed the experiments. J.R. performed surgeries, *ex vivo* experiments, *in vitro* experiments, and collected all data. J.R. analyzed microCT data, and live *ex vivo* staining J.R and P.B analyzed histological staining. P.T and P.B performed experiments in Figure 6 and 7. R.C. processed the metagenomic data. J.R., Y.T, A.V. and D.F. performed RNAseq analysis. J.R., P.T. and P.B. prepared the figures. J.R. and S.J.H. interpreted the data and wrote the initial manuscript draft. S.J.H revised the manuscript. All authors approved the manuscript. S.J.H. led the project and provided financial support for the project.

Acknowledgement

We thank Dr Nadège Zanou for discussions about the oligomycin experiments. We also thank Prof Mehdi Tafti and Dr Frédéric Schütz for discussions on statistics.
R.C. salary is supported by MRC MR/S023747/1. This research was supported by funds from the University of Lausanne, Switzerland (S.J.H). Additional financial support from the UK Regenerative Medicine Platform (MR/R015635/1, S.J.H.).

Competing interests:

S.J. H is listed as an inventor on a patent application (P6125GB00) on Tissue Regeneration Patch that includes the Wnt-bandage.

Materials and Methods References

Andrews S. 2015. Babraham Bioinformatics - FastQC A Quality Control tool for High Throughput Sequence Data. https://www.bioinformatics.babraham.ac.uk/projects/fastqc/

Bolger *et al.* 2014. Trimmomatic: a flexible trimmer for Illumina sequence data. *Bioinformatics*, 30(15); 21142120.

Bolyen *et al.* 2019. Reproducible, interactive, scalable and extensible microbiome data science using QIIME

2. *Nature Biotechnology*, 37; 852-857.
Callahan *et al.* 2016. DADA2: High-resolution sample inference from Illumina amplicon data. *Nature Methods*, 13; 581–583.
Ge, Steven Xijin *et al*. 2020. “ShinyGO: A Graphical Gene-Set Enrichment Tool for Animals and Plants.” *Bioinformatics* 36 (8): 2628–29.
Hao *et al.* 2021. “Integrated Analysis of Multimodal Single-Cell Data.” *Cell* 184 (13): 3573– 87.e29.
Kimmel *et al.* 2019. “Murine Single-Cell RNA-Seq Reveals Cell-Identity- and Tissue-Specific Trajectories of Aging.” *Genome Research* 29 (12): 2088–2103.
Lowndes *et al*. 2016. “Immobilized WNT Proteins Act as a Stem Cell Niche for Tissue Engineering”. *Stem Cell Reports*. 7(1):126-37
Lowndes *et al.* 2017. “Constructing Cellular Niche Properties by Localized Presentation of Wnt Proteins on Synthetic Surfaces.” *Nature Protocols* 12 (7): 1498–1512.
Okuchi *et al.* 2021. “Wnt-Modified Materials Mediate Asymmetric Stem Cell Division to Direct Human Osteogenic Tissue Formation for Bone Repair.” *Nature Materials* 20 (1): 108–18.

Main text Bibliography:

Agrawal Singh S, Lerdrup M, Gomes A-LR, van de Werken HJ, Vilstrup Johansen J, Andersson R, Sandelin A, Helin K, Hansen K. 2019. PLZF targets developmental enhancers for activation during osteogenic differentiation of human mesenchymal stem cells. *Elife* **8**. doi:10.7554/eLife.40364
Almalki SG, Agrawal DK. 2016. Effects of matrix metalloproteinases on the fate of mesenchymal stem cells. *Stem Cell Res Ther* **7**:129. doi:10.1186/s13287-016-0393-1
Almeida M. 2012. Aging mechanisms in bone. *Bonekey Rep* **1**. doi:10.1038/bonekey.2012.102
Ambriz X, de Lanerolle P, Ambrosio JR. 2018. The Mechanobiology of the Actin Cytoskeleton in Stem Cells during Differentiation and Interaction with Biomaterials. *Stem Cells Int* **2018**:2891957. doi:10.1155/2018/2891957
Andreatta M, Carmona SJ. 2021. UCell: Robust and scalable single-cell gene signature scoring. *Comput Struct Biotechnol J* **19**:3796–3798. doi:10.1016/j.csbj.2021.06.043
Andrikopoulos S, Blair AR, Deluca N, Fam BC, Proietto J. 2008. Evaluating the glucose tolerance test in mice. *Am J Physiol Endocrinol Metab* **295**:E1323-1332. doi:10.1152/ajpendo.90617.2008
Archbold HC, Yang YX, Chen L, Cadigan KM. 2012. How do they do Wnt they do?: regulation of transcription by the Wnt/β-catenin pathway. *Acta Physiol* **204**:74–109. doi:10.1111/j.1748-1716.2011.02293.x
Beedham W, Peck G, Richardson SE, Tsang K, Fertleman M, Shipway DJ. 2019. Head injury in the elderly - an overview for the physician. *Clin Med* **19**:177–184. doi:10.7861/clinmedicine.19-2-177
Bianco P, Robey PG. 2015. Skeletal stem cells. *Development* **142**:1023–1027. doi:10.1242/dev.102210
bin Imtiaz MK, Jaeger BN, Bottes S, Machado RAC, Vidmar M, Moore DL, Jessberger S. 2021. Declining lamin B1 expression mediates age-dependent decreases of hippocampal stem cell activity. *Cell Stem Cell* **28**:967-977.e8. doi:10.1016/j.stem.2021.01.015
Bixel MG, Sivaraj KK, Timmen M, Mohanakrishnan V, Aravamudhan A, Adams S, Koh B-I, Jeong H-W, Kruse K, Stange R, Adams RH. 2024. Angiogenesis is uncoupled from osteogenesis during calvarial bone regeneration. *Nat Commun* **15**:4575. doi:10.1038/s41467-024-48579-5
Bok S, Yallowitz AR, Sun J, McCormick J, Cung M, Hu L, Lalani S, Li Z, Sosa BR, Baumgartner T, Byrne P, Zhang T, Morse KW, Mohamed FF, Ge C, Franceschi RT, Cowling RT, Greenberg BH, Pisapia DJ, Imahiyerobo TA, Lakhani S, Ross ME, Hoffman CE, Debnath S, Greenblatt MB. 2023. A multi-stem cell basis for craniosynostosis and calvarial mineralization. *Nature* **621**:804–812. doi:10.1038/s41586-023-06526-2
Caliaperoumal G, Souyet M, Bensidhoum M, Petite H, Anagnostou F. 2018. Type 2 diabetes impairs angiogenesis and osteogenesis in calvarial defects: MicroCT study in ZDF rats. *Bone* **112**:161–172. doi:10.1016/j.bone.2018.04.009
Cappuzzello C, Doni A, Dander E, Pasqualini F, Nebuloni M, Bottazzi B, Mantovani A, Biondi A, Garlanda C, D’Amico G. 2016. Mesenchymal Stromal Cell-Derived PTX3 Promotes Wound Healing via Fibrin Remodeling. *J Invest Dermatol* **136**:293–300. doi:10.1038/JID.2015.346

1352 Carson HJ. 2009. Brain trauma in head injuries presenting with and without concurrent skull fractures. *J*
1353 *Forensic Leg Med* **16**:115–120. doi:10.1016/j.jflm.2008.08.013
1354 Catterson JH, Khericha M, Dyson MC, Vincent AJ, Callard R, Haveron SM, Rajasingam A, Ahmad M, Partridge
1355 L. 2018. Short-Term, Intermittent Fasting Induces Long-Lasting Gut Health and TOR-Independent
1356 Lifespan Extension. *Current Biology* **28**:1714-1724.e4. doi:10.1016/j.cub.2018.04.015
1357 Chan CKF, Lindau P, Jiang W, Chen JY, Zhang LF, Chen C-C, Seita J, Sahoo D, Kim J-B, Lee A, Park S, Nag
1358 D, Gong Y, Kulkarni S, Luppen CA, Theologis AA, Wan DC, DeBoer A, Seo EY, Vincent-Tompkins JD,
1359 Loh K, Walmsley GG, Kraft DL, Wu JC, Longaker MT, Weissman IL. 2013. Clonal precursor of bone,
1360 cartilage, and hematopoietic niche stromal cells. *Proc Natl Acad Sci U S A* **110**:12643–12648.
1361 doi:10.1073/pnas.1310212110
1362 Chan CKF, Seo EY, Chen JY, Lo D, McArdle A, Sinha R, Tevlin R, Seita J, Vincent-Tompkins J, Wearda T, Lu
1363 W-J, Senarath-Yapa K, Chung MT, Marecic O, Tran M, Yan KS, Upton R, Walmsley GG, Lee AS,
1364 Sahoo D, Kuo CJ, Weissman IL, Longaker MT. 2015. Identification and specification of the mouse
1365 skeletal stem cell. *Cell* **160**:285–298. doi:10.1016/j.cell.2014.12.002
1366 Chen J, Sivan U, Tan SL, Lippo L, De Angelis J, Labella R, Singh A, Chatzis A, Cheuk S, Medhghalchi M, Gil
1367 J, Hollander G, Marsden BD, Williams R, Ramasamy SK, Kusumbe AP. 2021. High-resolution 3D
1368 imaging uncovers organ-specific vascular control of tissue aging. *Sci Adv* **7**:eabd7819.
1369 doi:10.1126/sciadv.abd7819
1370 Cotofana S, Gotkin RH, Ascher B, Morozov SP, Gombolevsky VA, Laipan AS, Pyatintsky IA, Movsisyan TV,
1371 Koban KC, Hladik C, Frank K. 2018. Calvarial Volume Loss and Facial Aging: A Computed
1372 Tomographic (CT)-Based Study. *Aesthet Surg J* **38**:1043–1051. doi:10.1093/asj/sjy096
1373 Covarrubias AJ, Perrone R, Grozio A, Verdin E. 2021. NAD+ metabolism and its roles in cellular processes
1374 during ageing. *Nat Rev Mol Cell Biol* **22**:119–141. doi:10.1038/s41580-020-00313-x
1375 Creed S, McKenzie M. 2019. Measurement of Mitochondrial Membrane Potential with the Fluorescent Dye
1376 Tetramethylrhodamine Methyl Ester (TMRM). *Methods Mol Biol* **1928**:69–76. doi:10.1007/978-1-4939-
1377 9027-6_5
1378 Dahl KN, Ribeiro AJS, Lammerding J. 2008. Nuclear shape, mechanics, and mechanotransduction. *Circ Res*
1379 **102**:1307–1318. doi:10.1161/CIRCRESAHA.108.173989
1380 Damiola F, Le Minh N, Preitner N, Kornmann B, Fleury-Olela F, Schibler U. 2000. Restricted feeding uncouples
1381 circadian oscillators in peripheral tissues from the central pacemaker in the suprachiasmatic nucleus.
1382 *Genes Dev* **14**:2950–2961. doi:10.1101/gad.183500
1383 Dao MC, Everard A, Aron-Wisnewsky J, Sokolovska N, Prifti E, Verger EO, Kayser BD, Levenez F, Chilloux
1384 J, Hoyles L, MICRO-Obes Consortium, Dumas M-E, Rizkalla SW, Doré J, Cani PD, Clément K. 2016.
1385 Akkermansia muciniphila and improved metabolic health during a dietary intervention in obesity:
1386 relationship with gut microbiome richness and ecology. *Gut* **65**:426–436. doi:10.1136/gutjnl-2014-
1387 308778
1388 Debnath S, Yallowitz AR, McCormick J, Lalani S, Zhang T, Xu R, Li N, Liu Y, Yang YS, Eiseman M, Shim J-H,
1389 Hameed M, Healey JH, Bostrom MP, Landau DA, Greenblatt MB. 2018. Discovery of a periosteal stem
1390 cell mediating intramembranous bone formation. *Nature* **562**:133–139. doi:10.1038/s41586-018-0554-
1391 8
1392 Derrien M, Collado MC, Ben-Amor K, Salminen S, de Vos WM. 2008. The Mucin degrader Akkermansia
1393 muciniphila is an abundant resident of the human intestinal tract. *Appl Environ Microbiol* **74**:1646–
1394 1648. doi:10.1128/AEM.01226-07
1395 Devenish RJ, Prescott M, Boyle GM, Nagley P. 2000. [No title found]. *Journal of Bioenergetics and*
1396 *Biomembranes* **32**:507–515. doi:10.1023/A:1005621125812
1397 Ding L, Vezzani B, Khan N, Su J, Xu L, Yan G, Liu Y, Li R, Gaur A, Diao Z, Hu Y, Yang Z, Hardy WR, James
1398 AW, Sun H, Péault B. 2020. CD10 expression identifies a subset of human perivascular progenitor
1399 cells with high proliferation and calcification potentials. *Stem Cells* **38**:261–275. doi:10.1002/stem.3112
1400 Duchamp de Lageneste O, Julien A, Abou-Khalil R, Frangi G, Carvalho C, Cagnard N, Cordier C, Conway SJ,
1401 Colnot C. 2018. Periosteum contains skeletal stem cells with high bone regenerative potential
1402 controlled by Periostin. *Nat Commun* **9**:773. doi:10.1038/s41467-018-03124-z
1403 Dugina V, Zwaenepoel I, Gabbiani G, Clément S, Chaponnier C. 2009. Beta and gamma-cytoplasmic actins
1404 display distinct distribution and functional diversity. *J Cell Sci* **122**:2980–2988. doi:10.1242/jcs.041970

1405 Dutta S, Sengupta P. 2016. Men and mice: Relating their ages. *Life Sci* **152**:244–248.
1406 doi:10.1016/j.lfs.2015.10.025
1407 Egeblad M, Shen H-CJ, Behonick DJ, Wilmes L, Eichten A, Korets LV, Kheradmand F, Werb Z, Coussens LM.
1408 2007. Type I collagen is a genetic modifier of matrix metalloproteinase 2 in murine skeletal
1409 development. *Dev Dyn* **236**:1683–1693. doi:10.1002/dvdy.21159
1410 Ferrari S, Pesce M. 2021. Stiffness and Aging in Cardiovascular Diseases: The Dangerous Relationship
1411 between Force and Senescence. *Int J Mol Sci* **22**. doi:10.3390/ijms22073404
1412 Fletcher DA, Mullins RD. 2010. Cell mechanics and the cytoskeleton. *Nature* **463**:485–492.
1413 doi:10.1038/nature08908
1414 Gachon F, Nagoshi E, Brown SA, Ripperger J, Schibler U. 2004. The mammalian circadian timing system:
1415 from gene expression to physiology. *Chromosoma* **113**:103–112. doi:10.1007/s00412-004-0296-2
1416 Gachon F, Olela FF, Schaad O, Descombes P, Schibler U. 2006. The circadian PAR-domain basic leucine
1417 zipper transcription factors DBP, TEF, and HLF modulate basal and inducible xenobiotic detoxification.
1418 *Cell Metab* **4**:25–36. doi:10.1016/j.cmet.2006.04.015
1419 Garcin CL, Habib SJ. 2017. A Comparative Perspective on Wnt/β-Catenin Signalling in Cell Fate
1420 Determination. *Results Probl Cell Differ* **61**:323–350. doi:10.1007/978-3-319-53150-2_15
1421 Gillispie GJ, Sah E, Krishnamurthy S, Ahmidouch MY, Zhang B, Orr ME. 2021. Evidence of the Cellular
1422 Senescence Stress Response in Mitotically Active Brain Cells-Implications for Cancer and
1423 Neurodegeneration. *Life* **11**. doi:10.3390/life11020153
1424 Goligorsky MS. 2010. Microvascular rarefaction: The decline and fall of blood vessels. *Organogenesis* **6**:1–
1425 10. doi:10.4161/org.6.1.10427
1426 Goss AM, Tian Y, Tsukiyama T, Cohen ED, Zhou D, Lu MM, Yamaguchi TP, Morrisey EE. 2009. Wnt2/2b and
1427 beta-catenin signaling are necessary and sufficient to specify lung progenitors in the foregut. *Dev Cell*
1428 **17**:290–298. doi:10.1016/j.devcel.2009.06.005
1429 Gowans GJ, Hardie DG. 2014. AMPK: a cellular energy sensor primarily regulated by AMP. *Biochem Soc*
1430 *Trans* **42**:71–75. doi:10.1042/BST20130244
1431 Granéli C, Thorfve A, Ruetschi U, Brisby H, Thomsen P, Lindahl A, Karlsson C. 2014. Novel markers of
1432 osteogenic and adipogenic differentiation of human bone marrow stromal cells identified using a
1433 quantitative proteomics approach. *Stem Cell Res* **12**:153–165. doi:10.1016/j.scr.2013.09.009
1434 Grunewald M, Kumar S, Sharife H, Volinsky E, Gileles-Hillel A, Licht T, Permyakova A, Hinden L, Azar S,
1435 Friedmann Y, Kupetz P, Tzuberi R, Anisimov A, Alitalo K, Horwitz M, Leebhoff S, Khoma OZ, Hlushchuk
1436 R, Djonov V, Abramovitch R, Tam J, Keshet E. 2021. Counteracting age-related VEGF signaling
1437 insufficiency promotes healthy aging and extends life span. *Science* **373**:eabc8479.
1438 doi:10.1126/science.abc8479
1439 Haage A, Nam DH, Ge X, Schneider IC. 2014. Matrix metalloproteinase-14 is a mechanically regulated
1440 activator of secreted MMPs and invasion. *Biochem Biophys Res Commun* **450**:213–218.
1441 doi:10.1016/j.bbrc.2014.05.086
1442 Haffner-Luntzer M, Fischer V, Ignatius A. 2021. Differences in Fracture Healing Between Female and Male
1443 C57BL/6J Mice. *Front Physiol* **12**:712494. doi:10.3389/fphys.2021.712494
1444 Hirata H, Zhang N, Ueno M, Barati D, Kushioka J, Shen H, Tsubosaka M, Toya M, Lin T, Huang E, Yao Z, Wu
1445 JY, Zwingenberger S, Yang F, Goodman SB. 2022. Ageing attenuates bone healing by mesenchymal
1446 stem cells in a microribbon hydrogel with a murine long bone critical-size defect model. *Immun Ageing*
1447 **19**:14. doi:10.1186/s12979-022-00272-1
1448 Holstein JH, Becker SC, Fiedler M, Garcia P, Histing T, Klein M, Laschke MW, Corsten M, Pohlemann T,
1449 Menger MD. 2011. Intravital microscopic studies of angiogenesis during bone defect healing in mice
1450 calvaria. *Injury* **42**:765–771. doi:10.1016/j.injury.2010.11.020
1451 Horowitz MC, Fields A, DeMeo D, Qian HY, Bothwell AL, Trepman E. 1994. Expression and regulation of Ly-
1452 6 differentiation antigens by murine osteoblasts. *Endocrinology* **135**:1032–1043.
1453 doi:10.1210/endo.135.3.7520861
1454 Huang C, Ness VP, Yang X, Chen H, Luo J, Brown EB, Zhang X. 2015. Spatiotemporal Analyses of
1455 Osteogenesis and Angiogenesis via Intravital Imaging in Cranial Bone Defect Repair. *J Bone Miner*
1456 *Res* **30**:1217–1230. doi:10.1002/jbmr.2460
1457 Huelke DF, Compton CP. 1983. Facial injuries in automobile crashes. *J Oral Maxillofac Surg* **41**:241–244.
1458 doi:10.1016/0278-2391(83)90266-5

Jeffery EC, Mann TLA, Pool JA, Zhao Z, Morrison SJ. 2022. Bone marrow and periosteal skeletal stem/progenitor cells make distinct contributions to bone maintenance and repair. *Cell Stem Cell* **29**:1547-1561.e6. doi:10.1016/j.stem.2022.10.002

Jilka RL. 2013. The relevance of mouse models for investigating age-related bone loss in humans. *J Gerontol A Biol Sci Med Sci* **68**:1209–1217. doi:10.1093/gerona/glt046

Jin S, Guerrero-Juarez CF, Zhang L, Chang I, Ramos R, Kuan C-H, Myung P, Plikus MV, Nie Q. 2021. Inference and analysis of cell-cell communication using CellChat. *Nat Commun* **12**:1088. doi:10.1038/s41467-021-21246-9

Jung Y-S, Jun S, Lee SH, Sharma A, Park J-I. 2015. Wnt2 complements Wnt/β-catenin signaling in colorectal cancer. *Oncotarget* **6**:37257–37268. doi:10.18632/oncotarget.6133

Kang M-J, Ahn H-S, Lee J-Y, Matsuhashi S, Park W-Y. 2002. Up-regulation of PDCD4 in senescent human diploid fibroblasts. *Biochem Biophys Res Commun* **293**:617–621. doi:10.1016/S0006-291X(02)00264-4

Khan AU, Qu R, Fan T, Ouyang J, Dai J. 2020. A glance on the role of actin in osteogenic and adipogenic differentiation of mesenchymal stem cells. *Stem Cell Res Ther* **11**:283. doi:10.1186/s13287-020-01789-2

Kim H-N, Ponte F, Warren A, Ring R, Iyer S, Han L, Almeida M. 2021. A decrease in NAD+ contributes to the loss of osteoprogenitors and bone mass with aging. *NPJ Aging Mech Dis* **7**:8. doi:10.1038/s41514-021-00058-7

Kim Y. 2023. The impact of altered lamin B1 levels on nuclear lamina structure and function in aging and human diseases. *Curr Opin Cell Biol* **85**:102257. doi:10.1016/j.ceb.2023.102257

Kim Y-K, Nakata H, Yamamoto M, Miyasaka M, Kasugai S, Kuroda S. 2016. Osteogenic Potential of Mouse Periosteum-Derived Cells Sorted for CD90 In Vitro and In Vivo. *Stem Cells Transl Med* **5**:227–234. doi:10.5966/sctm.2015-0013

Kokabu S, Gamer L, Cox K, Lowery J, Tsuji K, Raz R, Economides A, Katagiri T, Rosen V. 2012. BMP3 suppresses osteoblast differentiation of bone marrow stromal cells via interaction with Acvr2b. *Mol Endocrinol* **26**:87–94. doi:10.1210/me.2011-1168

Lähteenvuo J, Rosenzweig A. 2012. Effects of Aging on Angiogenesis. *Circulation Research* **110**:1252–1264. doi:10.1161/CIRCRESAHA.111.246116

Lawenius L, Scheffler JM, Gustafsson KL, Henning P, Nilsson KH, Colldén H, Islander U, Plovier H, Cani PD, de Vos WM, Ohlsson C, Sjögren K. 2020. Pasteurized Akkermansia muciniphila protects from fat mass gain but not from bone loss. *Am J Physiol Endocrinol Metab* **318**:E480–E491. doi:10.1152/ajpendo.00425.2019

Lecarpentier Y, Claes V, Duthoit G, Hébert J-L. 2014. Circadian rhythms, Wnt/beta-catenin pathway and PPAR alpha/gamma profiles in diseases with primary or secondary cardiac dysfunction. *Front Physiol* **5**:429. doi:10.3389/fphys.2014.00429

Leite G, Pimentel M, Barlow GM, Chang C, Hosseini A, Wang J, Parodi G, Sedighi R, Rezaie A, Mathur R. 2021. Age and the aging process significantly alter the small bowel microbiome. *Cell Rep* **36**:109765. doi:10.1016/j.celrep.2021.109765

Levine ME, Suarez JA, Brandhorst S, Balasubramanian P, Cheng C-W, Madia F, Fontana L, Mirisola MG, Guevara-Aguirre J, Wan J, Passarino G, Kennedy BK, Wei M, Cohen P, Crimmins EM, Longo VD. 2014. Low Protein Intake Is Associated with a Major Reduction in IGF-1, Cancer, and Overall Mortality in the 65 and Younger but Not Older Population. *Cell Metabolism* **19**:407–417. doi:10.1016/j.cmet.2014.02.006

Li B, Wang Y, Fan Y, Ouchi T, Zhao Z, Li L. 2021. Cranial Suture Mesenchymal Stem Cells: Insights and Advances. *Biomolecules* **11**. doi:10.3390/biom11081129

Li H-S, Zhou Y-N, Li L, Li S-F, Long D, Chen X-L, Zhang J-B, Feng L, Li Y-P. 2019. HIF-1α protects against oxidative stress by directly targeting mitochondria. *Redox Biol* **25**:101109. doi:10.1016/j.redox.2019.101109

Li L, Chen Xiangjuan, Chen Xian, Yang L, Zeng Y, Xu J. n.d. TNFAIP6 Defines the MSC Subpopulation with Enhanced Immune Suppression Activities. doi:10.21203/rs.3.rs-1469688/v1

Li L, Su Y, Li F, Wang Y, Ma Z, Li Z, Su J. 2020. The effects of daily fasting hours on shaping gut microbiota in mice. *BMC Microbiol* **20**:65. doi:10.1186/s12866-020-01754-2

Li R, Liang Y, Lin B. 2022. Accumulation of systematic TPM1 mediates inflammation and neuronal remodeling by phosphorylating PKA and regulating the FABP5/NF-κB signaling pathway in the retina of aged mice. *Aging Cell* **21**:e13566. doi:10.1111/acel.13566

Li S, Zhan J-K, Wang Y-J, Lin X, Zhong J-Y, Wang Y, Tan P, He J-Y, Cui X-J, Chen Y-Y, Huang W, Liu Y-S. 2019. Exosomes from hyperglycemia-stimulated vascular endothelial cells contain versican that regulate calcification/senescence in vascular smooth muscle cells. *Cell Biosci* **9**:1. doi:10.1186/s13578-018-0263-x

Licciardi PV, Ververis K, Karagiannis TC. 2011. Histone deacetylase inhibition and dietary short-chain Fatty acids. *ISRN Allergy* **2011**:869647. doi:10.5402/2011/869647

Lim CH, Ito M. 2022. Niche stiffness regulates stem cell aging. *Nature Aging* **2**:568–569. doi:10.1038/s43587-022-00259-z

Liu G, Vijayakumar S, Grumolato L, Arroyave R, Qiao H, Akiri G, Aaronson SA. 2009. Canonical Wnts function as potent regulators of osteogenesis by human mesenchymal stem cells. *J Cell Biol* **185**:67–75. doi:10.1083/jcb.200810137

Liu J-H, Yue T, Luo Z-W, Cao J, Yan Z-Q, Jin L, Wan T-F, Shuai C-J, Wang Z-G, Zhou Y, Xu R, Xie H. 2020. Akkermansia muciniphila promotes type H vessel formation and bone fracture healing by reducing gut permeability and inflammation. *Dis Model Mech* **13**. doi:10.1242/dmm.043620

Liu M, Nakasaki M, Shih Y-RV, Varghese S. 2018. Effect of age on biomaterial-mediated in situ bone tissue regeneration. *Acta Biomater* **78**:329–340. doi:10.1016/j.actbio.2018.06.035

Liu S, Matsui TS, Kang N, Deguchi S. 2022. Analysis of senescence-responsive stress fiber proteome reveals reorganization of stress fibers mediated by elongation factor eEF2 in HFF-1 cells. *Mol Biol Cell* **33**:ar10. doi:10.1091/mbc.E21-05-0229

Liu TM, Lee EH. 2013. Transcriptional regulatory cascades in Runx2-dependent bone development. *Tissue Eng Part B Rev* **19**:254–263. doi:10.1089/ten.TEB.2012.0527

Locatelli V, Bianchi VE. 2014. Effect of GH/IGF-1 on Bone Metabolism and Osteoporsosis. *Int J Endocrinol* **2014**:235060. doi:10.1155/2014/235060

Loi F, Córdova LA, Pajarinen J, Lin T-H, Yao Z, Goodman SB. 2016. Inflammation, fracture and bone repair. *Bone* **86**:119–130. doi:10.1016/j.bone.2016.02.020

Longo VD, Anderson RM. 2022. Nutrition, longevity and disease: From molecular mechanisms to interventions. *Cell* **185**:1455–1470. doi:10.1016/j.cell.2022.04.002

Longo VD, Di Tano M, Mattson MP, Guidi N. 2021. Intermittent and periodic fasting, longevity and disease. *Nat Aging* **1**:47–59. doi:10.1038/s43587-020-00013-3

Lovett DB, Shekhar N, Nickerson JA, Roux KJ, Lele TP. 2013. Modulation of Nuclear Shape by Substrate Rigidity. *Cell Mol Bioeng* **6**:230–238. doi:10.1007/s12195-013-0270-2

Lowndes M, Rotherham M, Price JC, El Haj AJ, Habib SJ. 2016. Immobilized WNT Proteins Act as a Stem Cell Niche for Tissue Engineering. *Stem Cell Reports* **7**:126–137. doi:10.1016/j.stemcr.2016.06.004

Luo B, Zhou X, Tang Q, Yin Y, Feng G, Li S, Chen L. 2021. Circadian rhythms affect bone reconstruction by regulating bone energy metabolism. *J Transl Med* **19**:410. doi:10.1186/s12967-021-03068-x

Luo M-J, Rao S-S, Tan Y-J, Yin H, Hu X-K, Zhang Y, Liu Y-W, Yue T, Chen L-J, Li L, Huang Y-R, Qian Y-X, Liu Z-Z, Cao J, Wang Z-X, Luo Z-W, Wang Y-Y, Xia K, Tang S-Y, Chen C-Y, Xie H. 2020. Fasting before or after wound injury accelerates wound healing through the activation of pro-angiogenic SMOC1 and SCG2. *Theranostics* **10**:3779–3792. doi:10.7150/thno.44115

Lv J, Sun X, Ma J, Ma X, Xing G, Wang Y, Sun L, Wang J, Li F, Li Y. 2015. Involvement of periostin-sclerostin-Wnt/β-catenin signaling pathway in the prevention of neurectomy-induced bone loss by naringin. *Biochem Biophys Res Commun* **468**:587–593. doi:10.1016/j.bbrc.2015.10.152

Magne F, Gotteland M, Gauthier L, Zazueta A, Pesoa S, Navarrete P, Balamurugan R. 2020. The Firmicutes/Bacteroidetes Ratio: A Relevant Marker of Gut Dysbiosis in Obese Patients? *Nutrients* **12**. doi:10.3390/nu12051474

Maruyama T, Jeong J, Sheu T-J, Hsu W. 2016. Stem cells of the suture mesenchyme in craniofacial bone development, repair and regeneration. *Nat Commun* **7**:10526. doi:10.1038/ncomms10526

Matsushita Y, Ono W, Ono N. 2020. Skeletal Stem Cells for Bone Development and Repair: Diversity Matters. *Curr Osteoporos Rep* **18**:189–198. doi:10.1007/s11914-020-00572-9

1564 Matsushita Y, Sakamoto K, Tamamura Y, Shibata Y, Minamizato T, Kihara T, Ito M, Katsube K-I, Hiraoka S,
1565 Koseki H, Harada K, Yamaguchi A. 2013. CCN3 Protein Participates in Bone Regeneration as an
1566 Inhibitory Factor *. *J Biol Chem* **288**:19973–19985. doi:10.1074/jbc.M113.454652
1567 Matsu-Ura T, Moore SR, Hong CI. 2018. WNT Takes Two to Tango: Molecular Links between the Circadian
1568 Clock and the Cell Cycle in Adult Stem Cells. *J Biol Rhythms* **33**:5–14.
1569 doi:10.1177/0748730417745913
1570 McCarron JG, Wilson C, Sandison ME, Olson ML, Girkin JM, Saunter C, Chalmers S. 2013. From Structure
1571 to Function: Mitochondrial Morphology, Motion and Shaping in Vascular Smooth Muscle. *J Vasc Res*
1572 **50**:357–371. doi:10.1159/000353883
1573 McGuinness OP, Ayala JE, Laughlin MR, Wasserman DH. 2009. NIH experiment in centralized mouse
1574 phenotyping: the Vanderbilt experience and recommendations for evaluating glucose homeostasis in
1575 the mouse. *Am J Physiol Endocrinol Metab* **297**:E849-855. doi:10.1152/ajpendo.90996.2008
1576 Menon S, Salhotra A, Shailendra S, Tevlin R, Ransom RC, Januszyk M, Chan CKF, Behr B, Wan DC,
1577 Longaker MT, Quarto N. 2021. Skeletal stem and progenitor cells maintain cranial suture patency and
1578 prevent craniosynostosis. *Nat Commun* **12**:4640. doi:10.1038/s41467-021-24801-6
1579 Mills KF, Yoshida S, Stein LR, Grozio A, Kubota S, Sasaki Y, Redpath P, Migaud ME, Apte RS, Uchida K,
1580 Yoshino J, Imai S-I. 2016. Long-Term Administration of Nicotinamide Mononucleotide Mitigates Age-
1581 Associated Physiological Decline in Mice. *Cell Metab* **24**:795–806. doi:10.1016/j.cmet.2016.09.013
1582 Mosig RA, Dowling O, DiFeo A, Ramirez MCM, Parker IC, Abe E, Diouri J, Aqeel AA, Wylie JD, Oblander SA,
1583 Madri J, Bianco P, Apte SS, Zaidi M, Doty SB, Majeska RJ, Schaffler MB, Martignetti JA. 2007. Loss
1584 of MMP-2 disrupts skeletal and craniofacial development and results in decreased bone
1585 mineralization, joint erosion and defects in osteoblast and osteoclast growth. *Hum Mol Genet* **16**:1113–
1586 1123. doi:10.1093/hmg/ddm060
1587 Nakrani MN, Wineland RH, Anjum F. 2024. Physiology, Glucose MetabolismStatPearls. Treasure Island (FL):
1588 StatPearls Publishing.
1589 Novoseletskaya E, Grigorieva O, Nimiritsky P, Basalova N, Eremichev R, Milovskaya I, Kulebyakin K,
1590 Kulebyakina M, Rodionov S, Omelyanenko N, Efimenko A. 2020. Mesenchymal Stromal Cell-
1591 Produced Components of Extracellular Matrix Potentiate Multipotent Stem Cell Response to
1592 Differentiation Stimuli. *Front Cell Dev Biol* **8**:555378. doi:10.3389/fcell.2020.555378
1593 Nusspaumer G, Jaiswal S, Barbero A, Reinhardt R, Ishay Ronen D, Haumer A, Lufkin T, Martin I, Zeller R.
1594 2017. Ontogenic Identification and Analysis of Mesenchymal Stromal Cell Populations during Mouse
1595 Limb and Long Bone Development. *Stem Cell Reports* **9**:1124–1138.
1596 doi:10.1016/j.stemcr.2017.08.007
1597 Okuchi Y, Reeves J, Ng SS, Doro DH, Junyent S, Liu KJ, El Haj AJ, Habib SJ. 2021. Wnt-modified materials
1598 mediate asymmetric stem cell division to direct human osteogenic tissue formation for bone repair. *Nat*
1599 *Mater* **20**:108–118. doi:10.1038/s41563-020-0786-5
1600 Ortinau LC, Wang H, Lei K, Deveza L, Jeong Y, Hara Y, Grafe I, Rosenfeld SB, Lee D, Lee B, Scadden DT,
1601 Park D. 2019. Identification of functionally distinct Mx1+αSMA+ periosteal skeletal stem cells. *Cell*
1602 *Stem Cell* **25**:784-796.e5. doi:10.1016/j.stem.2019.11.003
1603 Ortona E, Pagano MT, Capossela L, Malorni W. 2023. The Role of Sex Differences in Bone Health and
1604 Healing. *Biology* **12**:993. doi:10.3390/biology12070993
1605 Özkul C, Yalınay M, Karakan T. 2019. Islamic fasting leads to an increased abundance of Akkermansia
1606 muciniphila and Bacteroides fragilis group: A preliminary study on intermittent fasting. *Turk J*
1607 *Gastroenterol* **30**:1030–1035. doi:10.5152/tjg.2019.19185
1608 Paine A, Woeller CF, Zhang H, Luz Garcia-Hernandez M, Huertas N, Xing L, Phipps RP, Ritchlin CT. 2018.
1609 Thy1 is a positive regulator of osteoblast differentiation and modulates bone homeostasis in obese
1610 mice. *FASEB j* **32**:3174–3183. doi:10.1096/fj.201701379R
1611 Petersen C, Nielsen MD, Andersen ES, Basse AL, Isidor MS, Markussen LK, Viuff BM, Lambert IH, Hansen
1612 JB, Pedersen SF. 2017. MCT1 and MCT4 Expression and Lactate Flux Activity Increase During White
1613 and Brown Adipogenesis and Impact Adipocyte Metabolism. *Sci Rep* **7**:13101. doi:10.1038/s41598-
1614 017-13298-z
1615 Pickel L, Sung H-K. 2020. Feeding Rhythms and the Circadian Regulation of Metabolism. *Front Nutr* **7**:39.
1616 doi:10.3389/fnut.2020.00039

1617 Pongkitwitoon S, Uzer G, Rubin J, Judex S. 2016. Cytoskeletal Configuration Modulates Mechanically
1618 Induced Changes in Mesenchymal Stem Cell Osteogenesis, Morphology, and Stiffness. *Sci Rep*
1619 **6**:34791. doi:10.1038/srep34791
1620 Provost PR, Marcel YL, Milne RW, Weech PK, Rassart E. 1991. Apolipoprotein D transcription occurs
1621 specifically in nonproliferating quiescent and senescent fibroblast cultures. *FEBS Lett* **290**:139–141.
1622 doi:10.1016/0014-5793(91)81244-3
1623 Rafei M, Hsieh J, Fortier S, Li M, Yuan S, Birman E, Forner K, Boivin M-N, Doody K, Tremblay M, Annabi B,
1624 Galipeau J. 2008. Mesenchymal stromal cell–derived CCL2 suppresses plasma cell immunoglobulin
1625 production via STAT3 inactivation and PAX5 induction. *Blood* **112**:4991–4998. doi:10.1182/blood-
1626 2008-07-166892
1627 Ren L, Wang D, Liu X, Yu H, Jiang C, Hu Y. 2020. Influence of Skull Fracture on Traumatic Brain Injury Risk
1628 Induced by Blunt Impact. *Int J Environ Res Public Health* **17**. doi:10.3390/ijerph17072392
1629 Ren X, Li B, Xu C, Zhuang H, Lei T, Jiang F, Zhou P. 2022. High expression of Piezo1 induces senescence in
1630 chondrocytes through calcium ions accumulation. *Biochem Biophys Res Commun* **607**:138–145.
1631 doi:10.1016/j.bbrc.2022.03.119
1632 Ren Y, Chu X, Senarathna J, Bhargava A, Grayson WL, Pathak AP. 2024. Multimodality imaging reveals
1633 angiogenic evolution in vivo during calvarial bone defect healing. *Angiogenesis* **27**:105–119.
1634 doi:10.1007/s10456-023-09899-0
1635 Reunanen J, Kainulainen V, Huuskonen L, Ottman N, Belzer C, Huhtinen H, de Vos WM, Satokari R. 2015.
1636 Akkermansia muciniphila Adheres to Enterocytes and Strengthens the Integrity of the Epithelial Cell
1637 Layer. *Appl Environ Microbiol* **81**:3655–3662. doi:10.1128/AEM.04050-14
1638 Ries C, Egea V, Karow M, Kolb H, Jochum M, Neth P. 2007. MMP-2, MT1-MMP, and TIMP-2 are essential for
1639 the invasive capacity of human mesenchymal stem cells: differential regulation by inflammatory
1640 cytokines. *Blood* **109**:4055–4063. doi:10.1182/blood-2006-10-051060
1641 Safwan-Zaiter H, Wagner N, Wagner K-D. 2022. P16INK4A—More Than a Senescence Marker. *Life* **12**:1332.
1642 doi:10.3390/life12091332
1643 Segel M, Neumann B, Hill MFE, Weber IP, Viscomi C, Zhao C, Young A, Agley CC, Thompson AJ, Gonzalez
1644 GA, Sharma A, Holmqvist S, Rowitch DH, Franze K, Franklin RJM, Chalut KJ. 2019. Niche stiffness
1645 underlies the ageing of central nervous system progenitor cells. *Nature* **573**:130–134.
1646 doi:10.1038/s41586-019-1484-9
1647 Shiozawa Y, Pedersen EA, Patel LR, Ziegler AM, Havens AM, Jung Y, Wang J, Zalucha S, Loberg RD, Pienta
1648 KJ, Taichman RS. 2010. GAS6/AXL axis regulates prostate cancer invasion, proliferation, and survival
1649 in the bone marrow niche. *Neoplasia* **12**:116–127. doi:10.1593/neo.91384
1650 Simiczyjew A, Mazur AJ, Popow-Woźniak A, Malicka-Błaszkiewicz M, Nowak D. 2014. Effect of
1651 overexpression of β- and γ-actin isoforms on actin cytoskeleton organization and migration of human
1652 colon cancer cells. *Histochem Cell Biol* **142**:307–322. doi:10.1007/s00418-014-1199-9
1653 Smith H, Whittall C, Weksler B, Middleton J. 2012. Chemokines stimulate bidirectional migration of human
1654 mesenchymal stem cells across bone marrow endothelial cells. *Stem Cells Dev* **21**:476–486.
1655 doi:10.1089/scd.2011.0025
1656 Song J, Li J, Yang F, Ning G, Zhen L, Wu L, Zheng Y, Zhang Q, Lin D, Xie C, Peng L. 2019. Nicotinamide
1657 mononucleotide promotes osteogenesis and reduces adipogenesis by regulating mesenchymal
1658 stromal cells via the SIRT1 pathway in aged bone marrow. *Cell Death Dis* **10**:336. doi:10.1038/s41419-
1659 019-1569-2
1660 Stein GH, Drullinger LF, Soulard A, Dulić V. 1999. Differential roles for cyclin-dependent kinase inhibitors p21
1661 and p16 in the mechanisms of senescence and differentiation in human fibroblasts. *Mol Cell Biol*
1662 **19**:2109–2117. doi:10.1128/MCB.19.3.2109
1663 Stein LR, Imai S-I. 2012. The dynamic regulation of NAD metabolism in mitochondria. *Trends Endocrinol*
1664 *Metab* **23**:420–428. doi:10.1016/j.tem.2012.06.005
1665 Stricker J, Falzone T, Gardel ML. 2010. Mechanics of the F-actin cytoskeleton. *J Biomech* **43**:9–14.
1666 doi:10.1016/j.jbiomech.2009.09.003
1667 Tang Y, Rowe RG, Botvinick EL, Kurup A, Putnam AJ, Seiki M, Weaver VM, Keller ET, Goldstein S, Dai J,
1668 Begun D, Saunders T, Weiss SJ. 2013. MT1-MMP-dependent control of skeletal stem cell commitment
1669 via a β1-integrin/YAP/TAZ signaling axis. *Dev Cell* **25**:402–416. doi:10.1016/j.devcel.2013.04.011

1670 Torimitsu S, Nishida Y, Takano T, Koizumi Y, Makino Y, Yajima D, Hayakawa M, Inokuchi G, Motomura A,
1671 Chiba F, Otsuka K, Kobayashi K, Odo Y, Iwase H. 2014. Statistical analysis of biomechanical properties
1672 of the adult skull and age-related structural changes by sex in a Japanese forensic sample. *Forensic*
1673 *Sci Int* **234**:185.e1–9. doi:10.1016/j.forsciint.2013.10.001
1674 Tran JR, Chen H, Zheng X, Zheng Y. 2016. Lamin in inflammation and aging. *Curr Opin Cell Biol* **40**:124–130.
1675 doi:10.1016/j.ceb.2016.03.004
1676 Trapnell C, Cacchiarelli D, Grimsby J, Pokharel P, Li S, Morse M, Lennon NJ, Livak KJ, Mikkelsen TS, Rinn
1677 JL. 2014. The dynamics and regulators of cell fate decisions are revealed by pseudotemporal ordering
1678 of single cells. *Nat Biotechnol* **32**:381–386. doi:10.1038/nbt.2859
1679 Tsai Y-C, Rau C-S, Huang J-F, Chang Y-M, Chia K-J, Hsieh T-M, Chou S-E, Su W-T, Hsu S-Y, Hsieh C-H.
1680 2022. The Association between Skull Bone Fractures and the Mortality Outcomes of Patients with
1681 Traumatic Brain Injury. *Emerg Med Int* **2022**:1296590. doi:10.1155/2022/1296590
1682 Tyurin-Kuzmin PA, Zhdanovskaya ND, Sukhova AA, Sagaradze GD, Albert EA, Ageeva LV, Sharonov GV,
1683 Vorotnikov AV, Tkachuk VA. 2016. Nox4 and Duox1/2 Mediate Redox Activation of Mesenchymal Cell
1684 Migration by PDGF. *PLoS One* **11**:e0154157. doi:10.1371/journal.pone.0154157
1685 van den Bos T, Speijer D, Bank RA, Brömme D, Everts V. 2008. Differences in matrix composition between
1686 calvaria and long bone in mice suggest differences in biomechanical properties and resorption: Special
1687 emphasis on collagen. *Bone* **43**:459–468. doi:10.1016/j.bone.2008.05.009
1688 Veronese N, Reginster J-Y. 2019. The effects of calorie restriction, intermittent fasting and vegetarian diets on
1689 bone health. *Aging Clin Exp Res* **31**:753–758. doi:10.1007/s40520-019-01174-x
1690 Villa CR, Ward WE, Comelli EM. 2017. Gut microbiota-bone axis. *Crit Rev Food Sci Nutr* **57**:1664–1672.
1691 doi:10.1080/10408398.2015.1010034
1692 Volonte D, Galbiati F. 2020. Caveolin-1, a master regulator of cellular senescence. *Cancer Metastasis Rev*
1693 **39**:397–414. doi:10.1007/s10555-020-09875-w
1694 Wagner W, Bork S, Horn P, Krunic D, Walenda T, Diehlmann A, Benes V, Blake J, Huber F-X, Eckstein V,
1695 Boukamp P, Ho AD. 2009. Aging and replicative senescence have related effects on human stem and
1696 progenitor cells. *PLoS One* **4**:e5846. doi:10.1371/journal.pone.0005846
1697 Wahlestedt M, Ladopoulos V, Hidalgo I, Sanchez Castillo M, Hannah R, Säwén P, Wan H, Dudenhöffer-Pfeifer
1698 M, Magnusson M, Norddahl GL, Göttgens B, Bryder D. 2017. Critical Modulation of Hematopoietic
1699 Lineage Fate by Hepatic Leukemia Factor. *Cell Rep* **21**:2251–2263. doi:10.1016/j.celrep.2017.10.112
1700 Wanandi SI, Purnamawati P, Tamara A, Putri KT, Simadibrata DM. 2018. Analysis of ALDH1A1 and ALDH1A3
1701 Gene mRNA Expressions in Adipose-Derived Stem Cells (ASCs) and Umbilical Cord Stem Cells
1702 (UCSCs). *The Indonesian Biomedical Journal* **10**:290–296. doi:10.18585/inabj.v10i3.477
1703 Wang D, Christensen K, Chawla K, Xiao G, Krebsbach PH, Franceschi RT. 1999. Isolation and
1704 characterization of MC3T3-E1 preosteoblast subclones with distinct in vitro and in vivo
1705 differentiation/mineralization potential. *J Bone Miner Res* **14**:893–903.
1706 doi:10.1359/jbmr.1999.14.6.893
1707 Westermann B. 2012. Bioenergetic role of mitochondrial fusion and fission. *Biochimica et Biophysica Acta*
1708 *(BBA) - Bioenergetics* **1817**:1833–1838. doi:10.1016/j.bbabio.2012.02.033
1709 Wiese DM, Ruttan CC, Wood CA, Ford BN, Braid LR. 2019. Accumulating Transcriptome Drift Precedes Cell
1710 Aging in Human Umbilical Cord-Derived Mesenchymal Stromal Cells Serially Cultured to Replicative
1711 Senescence. *Stem Cells Transl Med* **8**:945–958. doi:10.1002/sctm.18-0246
1712 Wilk K, Yeh S-CA, Mortensen LJ, Ghaffarigarakani S, Lombardo CM, Bassir SH, Aldawood ZA, Lin CP, Intini
1713 G. 2017. Postnatal Calvarial Skeletal Stem Cells Expressing PRX1 Reside Exclusively in the Calvarial
1714 Sutures and Are Required for Bone Regeneration. *Stem Cell Reports* **8**:933–946.
1715 doi:10.1016/j.stemcr.2017.03.002
1716 Xie S-A, Zhang T, Wang J, Zhao F, Zhang Y-P, Yao W-J, Hur SS, Yeh Y-T, Pang W, Zheng L-S, Fan Y-B, Kong
1717 W, Wang X, Chiu J-J, Zhou J. 2018. Matrix stiffness determines the phenotype of vascular smooth
1718 muscle cell in vitro and in vivo: Role of DNA methyltransferase 1. *Biomaterials* **155**:203–216.
1719 doi:10.1016/j.biomaterials.2017.11.033
1720 Yang J, Liu K, Yang J, Jin B, Chen H, Zhan X, Li Z, Wang L, Shen X, Li M, Yu W, Mao Z. 2017. PIM1 induces
1721 cellular senescence through phosphorylation of UHRF1 at Ser311. *Oncogene* **36**:4828–4842.
1722 doi:10.1038/onc.2017.96

1723 Yang Y, Sauve AA. 2016. NAD+ metabolism: Bioenergetics, signaling and manipulation for therapy.
1724 *Biochimica et Biophysica Acta (BBA) - Proteins and Proteomics* **1864**:1787–1800.
1725 doi:10.1016/j.bbapap.2016.06.014
1726 Yates LB, Karasik D, Beck TJ, Cupples LA, Kiel DP. 2007. Hip structural geometry in old and old-old age:
1727 similarities and differences between men and women. *Bone* **41**:722–732.
1728 doi:10.1016/j.bone.2007.06.001
1729 Ye Y, Hu W, Guo F, Zhang W, Wang J, Chen A. 2012. Glycosaminoglycan chains of biglycan promote bone
1730 morphogenetic protein-4-induced osteoblast differentiation. *Int J Mol Med* **30**:1075–1080.
1731 doi:10.3892/ijmm.2012.1091
1732 Yoshitane H, Asano Y, Sagami A, Sakai S, Suzuki Y, Okamura H, Iwasaki W, Ozaki H, Fukada Y. 2019.
1733 Functional D-box sequences reset the circadian clock and drive mRNA rhythms. *Commun Biol* **2**:300.
1734 doi:10.1038/s42003-019-0522-3
1735 Zhang F, Luo K, Rong Z, Wang Z, Luo F, Zhang Z, Sun D, Dong S, Xu J, Dai F. 2017. Periostin Upregulates
1736 Wnt/β-Catenin Signaling to Promote the Osteogenesis of CTLA4-Modified Human Bone Marrow-
1737 Mesenchymal Stem Cells. *Sci Rep* **7**:41634. doi:10.1038/srep41634
1738 Zhang J, Ma Z, Yan K, Wang Y, Yang Y, Wu X. 2019. Matrix Gla Protein Promotes the Bone Formation by Up-
1739 Regulating Wnt/β-Catenin Signaling Pathway. *Front Endocrinol* **10**:891.
1740 doi:10.3389/fendo.2019.00891
1741 Zhang W, Chen E, Chen M, Ye C, Qi Y, Ding Q, Li H, Xue D, Gao X, Pan Z. 2018. IGFBP7 regulates the
1742 osteogenic differentiation of bone marrow-derived mesenchymal stem cells via Wnt/β-catenin
1743 signaling pathway. *FASEB J* **32**:2280–2291. doi:10.1096/fj.201700998RR
1744 Zhao H, Feng J, Ho T-V, Grimes W, Urata M, Chai Y. 2015. The suture provides a niche for mesenchymal
1745 stem cells of craniofacial bones. *Nat Cell Biol* **17**:386–396. doi:10.1038/ncb3139
1746 Zhong-Sheng Z, Nuo Y, Xiao-Yan H, Liang D, Rui F, Hai-Jun X. 2022. MMP2 promotes osteoblast
1747 differentiation and calcification of muscle-derived mesenchymal stem cells by interaction with miR-
1748 29b-3p. *Tissue Cell* **76**:101807. doi:10.1016/j.tice.2022.101807
1749 Zhou L, Zhang T, Sun S, Yu Y, Wang M. 2018. Cryptochrome 1 promotes osteogenic differentiation of human
1750 osteoblastic cells via Wnt/β-Catenin signaling. *Life Sci* **212**:129–137. doi:10.1016/j.lfs.2018.09.053
1751 Zhu L, Tang Y, Li X-Y, Keller ET, Yang J, Cho J-S, Feinberg TY, Weiss SJ. 2020. Osteoclast-mediated bone
1752 resorption is controlled by a compensatory network of secreted and membrane-tethered
1753 metalloproteinases. *Sci Transl Med* **12**. doi:10.1126/scitranslmed.aaw6143
1754 Zorova LD, Popkov VA, Plotnikov EY, Silachev DN, Pevzner IB, Jankauskas SS, Babenko VA, Zorov SD,
1755 Balakireva AV, Juhaszova M, Sollott SJ, Zorov DB. 2018. Mitochondrial membrane potential. *Anal*
1756 *Biochem* **552**:50–59. doi:10.1016/j.ab.2017.07.009
1757